

1988

The NASA Langley Laminar-Flow-Control Experiment on a Swept, Supercritical Airfoil

Design Overview

Charles D. Harris,
William D. Harvey,
and Cuyler W. Brooks, Jr.

*Langley Research Center
Hampton, Virginia*



National Aeronautics
and Space Administration

Scientific and Technical
Information Division

Contents

Summary	1
Introduction	1
Symbols	2
General Background	4
List of Figures	4
General Design and Experimental Considerations	5
Test Setup in the 8-Ft TPT	6
Wind Tunnel	6
Wind-Tunnel Model	6
Wind-Tunnel Liner	6
Sonic Choke Devices	7
Wind-Tunnel Screens and Honeycomb	7
Model Suction System	7
Laminar-Flow-Control Airfoil Design	7
Design Cycle	7
Theoretical Pressure Distributions	8
Theoretical Shock-Free Limits	9
Stability Analysis	9
Upper surface	10
Lower surface	11
Drag Divergence	11
Laminar-Flow-Control Model Suction System	12
Airfoil Suction Requirements	12
Model laminar region	12
Model turbulent region	12
Slot Design	12
Analysis	13
Slot geometry	13
Slot plenum	13
Suction Nozzle Design	14
Laminar-Flow-Control Model Design and Fabrication	14
Slotted Surface Structure	14
Structural features	14
Fabrication process	14
Surface tolerance	15
Model Suction Ducts and Nozzle Layout	15
Airflow Control System External to Model	16
Airflow Boxes	16
Sonic Nozzles	16
Tunnel Modifications	16
Test Section Liner	17
Concept	17
Liner/collar suction	17

Liner hardware	17
Flow Quality Modifications	18
Screens	18
Honeycomb	18
Sonic throat	19
Measurements and Instrumentation	19
Real-Time Data System	20
Free-Stream Conditions	20
Aerodynamic Measurements	20
Surface static pressure measurements	20
Profile drag rake	20
Dynamic measurements	21
Tunnel Liner and Choke	21
Suction System	21
Ducts, nozzles, and evacuation lines	21
Airflow control boxes and variable sonic nozzles	21
Concluding Remarks	22
References	22
Tables	25
Figures	32

Summary

A 23°-swept, 13-percent-thick, 7.07-ft-chord, supercritical, laminar-flow-control (LFC) airfoil has been designed and constructed and is currently undergoing tests in the Langley 8-Foot Transonic Pressure Tunnel. Design conditions included a free-stream Mach number of 0.82, a section lift coefficient of 0.47, and a Reynolds number of 20×10^6 , based on free-stream conditions and model chord. This ambitious and very complex experiment was directed toward evaluating the compatibility of LFC and supercritical airfoils, validating prediction techniques, and generating a data base for future transport airfoil design. Unique features of the laminar-flow-control airfoil included a high design Mach number with shock-free flow and boundary-layer control by suction. Special requirements for the experiment included modifications to the wind tunnel to achieve the necessary flow quality and contouring of the test section walls to simulate free airflow about an infinite yawed model at transonic speeds. The first phase of the experiment—the evaluation of a slotted suction surface—has been completed. The second phase—the evaluation of a perforated suction surface—is currently under way. The design of the slotted airfoil, the suction system, and modifications to the tunnel to meet test requirements are discussed.

Introduction

A reduction in drag and, hence, an increase in vehicle performance have always been primary goals of aerodynamicists. One of the primary sources of aerodynamic drag is the skin friction associated with turbulent boundary layers, and large decreases in drag can be realized if the boundary layer can be prevented from going turbulent. Both passive and active means of maintaining laminar flow by boundary-layer control have been investigated. Passive or natural-laminar-flow (NLF) systems are controlled through the choice of geometry and pressure gradients, whereas active or laminar-flow-control (LFC) systems depend on both geometry and mass transfer through the surface to stabilize the laminar boundary layer.

Past research efforts have included the development and testing of airfoils and wings designed for both natural and suction-augmented laminar flow. In general, investigations involving the application of suction through the surface to maintain laminar flow have provided large reductions in both friction and profile drag. A collection of theoretical and experimental papers dealing with boundary-layer control is presented in reference 1. A detailed discussion and a summary review of a large number of LFC

investigations, including wind-tunnel and flight results, are presented in reference 2.

The feasibility of achieving full-chord laminar flow with active boundary-layer control on swept, conventional wings has been demonstrated and is discussed in reference 2. Low-speed suction experiments were conducted during the late 1950's on a symmetrical, 7.00-ft-chord, 30°-swept, 12-percent-thick wing of a modified NACA 66-012 airfoil section in the Michigan 5- by 7-Foot, Norair 7- by 10-Foot, and NASA Ames 12-Foot Pressure Wind Tunnels. Continuous suction was approached by means of closely spaced suction slots. Full-chord laminar boundary layers were maintained up to a chord Reynolds number of 29×10^6 in the Ames tunnel, and up to 14×10^6 in the Michigan and Norair tunnels. Differences in the extent of laminar flow achieved in the different tunnels were attributed to stream turbulence levels (ref. 2).

A reasonably efficient LFC suction system, using closely spaced suction slots, was developed and flight tested on an F-94 LFC wing glove (ref. 3) and on an X-21 wing (ref. 4) during the 1950's and 1960's. Neither the 10°-swept F-94 glove nor the 33°-swept X-21 wing were designed as supercritical sections but were flight tested at high subsonic speeds. Aside from some sensitivity to insect contamination and ice crystals, these flight tests demonstrated that large regions of laminar flow could be consistently achieved in flight on wings with suction.

Interest in laminar-flow control waned during the 1960's because of practical concerns about the operational feasibility of aircraft incorporating LFC. Among these concerns were the inability of manufacturing technology to build wings sufficiently smooth and wave free, the loss of laminar flow associated with surface contamination, and the deterioration of wing surface quality in normal service operations.

Rising oil prices in the 1970's and the associated need for improved fuel economy stimulated a renewed interest in laminar-flow control. Although oil prices have stabilized and even dropped in the decade since the dramatic increase of the 1970's, fuel prices remain high enough to make LFC attractive. The likelihood of future oil price increases, the threat of oil import fees, and a possible scarcity of oil help to sustain a strong impetus for a continued effort toward drag reduction. The steadily increasing market for extremely long range commercial and military aircraft also provides an impetus to the effort since laminar flow adds substantially to the range capability of an aircraft.

Renewed interest in LFC also stemmed from the fact that none of the emerging technologies identified by NASA's aircraft energy efficiency (ACEE)

programs had more potential for producing efficient, economically superior aircraft than laminar-flow control (ref. 5). Potential fuel savings could range from 20 to 40 percent depending on the extent of application and the design range of the aircraft.

This economic impetus coincided with emerging improvements in materials, fabrication methods, theoretical design and analysis techniques for both aerodynamics and structures, and advanced airfoil technology. More sophisticated boundary-layer codes for stability analysis and the determination of suction requirements reduced the task of solving LFC design problems and made the application of laminar-flow control a more realistic objective.

Because of the potential benefits, the National Aeronautics and Space Administration (NASA) decided in the mid-1970's to take advantage of these improving technologies and incorporate them with supercritical airfoil technology. Research began to determine if laminar flow—aided by boundary-layer removal through slotted or perforated surfaces—could be maintained through a large supersonic bubble on the upper surface of a high-performance, 13-percent-thick, 23°-swept supercritical wing.

An early overview of the resulting laminar-flow-control experiment was presented in reference 6. Installation of the model and associated tunnel modifications in the Langley 8-Foot Transonic Pressure Tunnel (8-ft TPT) began in May 1981. The first phase of the experiment—the evaluation of a slotted suction surface (refs. 7 and 8)—has been completed and the second phase—the evaluation of a perforated suction surface—is currently under way.

This report expands the information presented in reference 6 to include design changes subsequently incorporated into the experiment. It describes the slotted, LFC, supercritical-wing model (phase 1 of the LFC experiment) and includes advanced design and analysis techniques, materials, design goals, and fabrication processes employed to achieve these goals. The test environment for proper LFC evaluation and modifications to the 8-ft TPT undertaken to meet these requirements are discussed also.

Symbols

a	disturbance amplitude
a_o	initial disturbance amplitude
B	growth factor, $\beta\theta R_\theta$
C_p	pressure coefficient, $\frac{p - p_\infty}{q_\infty}$
$C_{p,sonic}$	pressure coefficient corresponding to local Mach number of 1.0

C_Q	coefficient of suction, $\frac{\rho w w_w}{\rho_\infty U_\infty}$
c	model chord parallel to free-stream direction, 7.07 ft
c_l	section lift coefficient
$c_{l,N}$	section lift coefficient normal to leading edge
d	diameter
f	frequency
G	Görtler parameter, $R_\theta(\theta/r)^{1/2}$
h	plenum height, nozzle height, or surface wave height
M	Mach number
n	exponent in expression for disturbance growth
p	pressure, psf
q	dynamic pressure, psf
R	Reynolds number
R_c	Reynolds number based on free-stream conditions and model chord
$R_{c,N}$	Reynolds number based on flow conditions and chord normal to leading edge
R_{ft}	unit Reynolds number based on length of 1 ft
R_n	crossflow Reynolds number based on maximum cross-flow velocity and boundary-layer height at which cross-flow velocity is one-tenth of its maximum value
R_s	Reynolds number based on slot width
R_x	local Reynolds number based on coordinate x
R_θ	Reynolds number based on momentum thickness
$R_{\theta,al}$	attachment-line Reynolds number based on velocity of flow along attachment line and boundary-layer momentum thickness

r	radius of surface curvature	w	wall (airfoil surface)
s	slot width	∞	free stream
T	temperature, °F	Superscripts:	
t	thickness	'	root-mean-square value
U_{∞}	free-stream velocity	-	mean value
u, w	velocity components in x - and z -directions, respectively	Abbreviations:	
x	distance along model chord from leading edge (positive toward trailing edge)	ARC	Ames Research Center
y	distance along model span from centerline of test section (positive toward top of test section)	BL	boundary layer
z	distance perpendicular to model chord plane (positive toward model upper surface), or sucked height of boundary layer (incremental portion of local boundary layer removed by suction)	CF	crossflow
β	disturbance growth rate	CFM	cubic feet per minute
γ	ratio of specific heats	ESP	electroscanning pressure
Δ	incremental amount	LaRC	Langley Research Center
δ	flap angle, deg	LE	leading edge
θ	momentum thickness	LFC	laminar-flow control
Λ	leading-edge sweep angle, deg	TE	trailing edge
λ	wavelength	T-G	Taylor-Görtler
ρ	density	T-S	Tollmien-Schlichting
τ	local shear stress	TPT	Transonic Pressure Tunnel
Subscripts:		2-D, 3-D	two- and three-dimensional
DD	drag divergence	Tunnel designations:	
e	boundary-layer edge value	ARC 12-ft PWT	Ames 12-Foot Pressure Wind Tunnel
ℓ	lower surface	LaRC 8-ft TPT	Langley 8-Foot Transonic Pressure Tunnel
max	maximum	LaRC LTPT	Langley Low-Turbulence Pressure Tunnel
N	normal to leading edge	LaRC TDT	Langley Transonic Dynam- ics Tunnel
t	total conditions	Michigan 5 × 7	University of Michigan 5- by 7-Foot Wind Tunnel
u	upper surface	Norair 7 × 10	Northrop Corporation 7- by 10-Foot Subsonic Wind Tunnel
		Zurich 7 × 10	Institute for Aerodynamics 7- by 10-Foot Wind Tunnel at the Federal Institute of Technology, Zurich, Switzerland

General Background

During the mid-1970's, the NASA Langley Research Center defined an experiment employing advanced theoretical tools, materials, and manufacturing processes to extend laminar-flow control to supercritical airfoils. The overall objective of the experiment was to provide basic information concerning the design and compatibility of swept, supercritical airfoils with active boundary-layer control at conditions typical of high-performance transport aircraft.

The experiment, including both hardware and test procedures, was ambitious and very complex. The large-chord airfoil model posed a particularly difficult design problem in simulating unbounded free airflow around the model (i.e., free of blockage and wall interference), and thus extensive analyses and modifications were required to contour the walls of the tunnel test section. The integration of laminar-flow control with swept supercritical-wing technology also required advanced fabrication techniques to construct a suitable model. The effect of wind-tunnel flow quality had to be properly assessed and the tunnel test environment modified to satisfy the resultant requirements.

Several surface suction concepts with viscous drag reduction potential were to be investigated. These included the following: (1) upper- and lower-surface suction through discrete slots, (2) upper-surface suction through a perforated skin and lower-surface suction through discrete slots, (3) upper-surface suction through a perforated skin and a solid, nonsuction lower surface, and (4) various hybrid configurations combining boundary-layer control over the forward region by suction and over the rear region by nonsuction geometric shaping. This report discusses only the first phase, that is, suction through discrete slots on both upper and lower surfaces. Reference 9 describes the perforated upper-surface panels used in the second phase of the experiment.

List of Figures

For the convenience of the reader, a list of the figures, including both pictorial and graphic results, is given as follows:

	Figure
Airfoil design parameters	1
Variation of chord Reynolds number with sweep angle for constant crossflow Reynolds number	2
Test section liner	3
General test setup in Langley 8-ft TPT	4
Photographs of test section liner and model	5
Choke plates on opposing sides of test section liner	6
Model suction system	7
Block diagram of LFC airfoil design cycle	8
Theoretical pressure distributions and sonic lines for "near-final" shock-free design and high-lift off-design conditions normal to leading edge	9
"Final" theoretical pressure distribution normal to leading edge combining Korn-Garabedian and Eppler calculations	10
Sketches of LFC airfoil normal to leading edge	11
Variation of theoretical shock-free limits with Mach number	12
Calculated maximum-disturbance amplitude ratios for design conditions	13
Theoretical suction distributions for LFC airfoil with continuous area suction	14
Linearized maximum growth factor B of Taylor-Görtler vortices versus Görtler parameter G for incompressible flow with and without suction	15
Representative values of theoretical maximum-disturbance amplitude ratio for Taylor-Görtler vortices with small incremental turn of flow	16
Comparison of drag-divergence Mach number for present LFC airfoil with turbulent supercritical and conventional airfoils	17
Theoretical suction requirements for slotted LFC airfoil for $Re = 10 \times 10^6$ and 20×10^6	18
Planform view of model from lower surface in tunnel	19
Spanwise variation of design suction distribution of slotted LFC airfoil	20
Experimental limits for variations of suction plenum ratio of height to slot width with slot Reynolds number for several limiting metering-hole geometries	21
Sketches of suction duct nozzles	22
Cross section of LFC model normal to leading edge	23

Sketches showing features of surface and internal suction system of model nose and flap regions	24
Photographs of model panels in various stages of fabrication	25
Photograph of orifice drilling process on lower-surface forward panel	26
Photographs of model suction-panel assemblies during fabrication process	27
Photograph of wingbox installed in test section	28
Comparison of variation of permissible amplitude ratio h/λ for multiple waves on subsonic and supersonic airfoils with full-chord LFC	29
Internal suction ducting and nozzle layout	30
Photograph of penetration holes in end of panel	31
Airfoil control system	32
Sketch showing details of airflow control boxes	33
Photographs of airfoil control boxes	34
Variable sonic nozzle	35
Block diagram outlining tunnel-liner contour-design procedure	36
Scaled illustration of relative size of LFC airfoil model, 3-D supersonic flow regions, and inviscid liner shape	37
Sketch of liner contours	38
Sketch of spanwise streamline displacement over swept wing	39
Suction collar	40
Photographs of liner-block milling process	41
Photographs of liner installation	42
Influence of turbulence level on maximum chord Reynolds number with laminar-flow suction control for low-drag wings and bodies of revolution in wind tunnels and flight	43
Measured and predicted disturbance levels in the 8-ft TPT with and without choke, honeycomb, and screens at $M_\infty = 0.80$	44
Upstream view from test section of fifth screen	45
Photographs of honeycomb and turning vanes from floor of tunnel between honeycomb and turning vanes	46

Adjustable wall choke plates	47
Theoretical distribution of pressure coefficients along middle of liner wall opposite airfoil upper surface at design conditions	48
Model surface instrumentation	49
Sketch and photographs of profile drag rake and schematic of wake profile	50
Pressure orifice locations over four walls of liner	51

General Design and Experimental Considerations

As a result of the complexity of the LFC experiment, considerable discussion focused on choosing the proper design parameters. Choices were particularly difficult during early planning because of the uncertainty as to whether the experiment would be conducted in the Langley 8-Foot Transonic Pressure Tunnel (8-ft TPT) or in the larger Ames 12-Foot Pressure Wind Tunnel (12-ft PWT). The Langley facility was eventually chosen and, following preliminary studies and evaluations, the design parameters shown in figure 1 were selected. These studies and evaluations are beyond the intended scope of this report, but general design and experimental considerations are noted.

Among the many design and experimental factors affecting transition on airfoils in a wind tunnel are the size of the model, sweep, Reynolds number, surface waviness and roughness, pressure gradients, shock impingement, wind-tunnel disturbance levels, and wind-tunnel blockage and wall interference. Close tolerances must be maintained during fabrication of the model, and airfoil pressure gradients (including pressure discontinuities through shock regions) must be controlled by careful tailoring of the airfoil geometry. Simplification of suction requirements through a highly tailored pressure distribution is also of major importance. In order to minimize the effect of background disturbances on transition, tunnel disturbance levels should be low ($u'/U_\infty < 0.1$ percent).

Maintaining laminar flow on airfoil models in wind tunnels is often a more difficult aerodynamic problem than on full-scale wing surfaces. For instance, the achievement of moderately high chord Reynolds numbers on a practical-sized model requires testing at high unit Reynolds numbers in most tunnels. Since the characteristic disturbance levels in wind tunnels increase with increasing unit Reynolds number and Mach number, tunnel background disturbance levels become critical for high

chord Reynolds number testing. Wind-tunnel testing at high unit Reynolds numbers also adversely affects suction system design and surface smoothness criteria, and physical dimensions are frequently so small that practical fabrication tolerances for certain model features become difficult to achieve. Therefore, a large (7.07-ft) chord was chosen for the LFC experiment in the 8-ft TPT so that the experiment could be conducted at a lower unit Reynolds number with corresponding low background disturbance levels. A large chord was also dictated by constraints on slot-duct construction, surface tolerances, and the necessity to minimize fabrication scale effects.

Early airfoil design configurations (refs. 10 through 12, for example) had a chord of 7.00 ft. The chord was extended by 1.0 percent for the final configuration to alleviate the adverse pressure gradient in the trailing-edge pressure recovery region and reduce the possibility of boundary-layer separation on the model and tunnel walls (ref. 13).

Since future transport aircraft with LFC are envisioned to have moderately swept ($\approx 20^\circ$ to 30°) wings, laminar boundary-layer crossflow stability was investigated at simulated-flight crossflow Reynolds numbers on a model designed with 23° of sweep. The choice of leading-edge sweep was more or less a balanced compromise between opposing considerations. Reducing the sweep is beneficial since it reduces suction requirements and allows placement of the first slot farther downstream where there is less susceptibility to erosion and other incidental damage. Increasing the sweep allows greater wing thickness, reduced weight, and higher drag-divergence Mach number.

The combination of design Mach number, thickness ratio, lift coefficient, sweep, and Reynolds number was selected based on the simulation of cruise conditions envisioned for future transport aircraft. Figure 2 shows the selected design conditions for the swept LFC airfoil compared with design conditions for future LFC aircraft. The expected range of the test Reynolds number R_c from 8 to 40×10^6 at $\Lambda = 23^\circ$, $c_l = 0.47$, and $M_\infty = 0.82$ is typical of the envisioned flight cruise conditions for such aircraft.

The chord chosen for the experiment, 7.07 ft, resulted in a total tunnel height-to-chord ratio of about 1. To avoid blockage problems and to minimize wall interference over such a large-chord swept wing, a test section liner was designed to match the contours of the surrounding unbounded streamlines (fig. 3). In addition, it was necessary to improve flow quality and minimize upstream noise propagation in the tunnel by adding turbulence suppression devices in the settling chamber and a sonic throat at the diffuser entrance to prevent facility-generated

vorticity and acoustic disturbances (refs. 14 and 15) from having a destabilizing effect on the model boundary layer.

Test Setup in the 8-Ft TPT

Schematics of the overall LFC experimental setup in the 8-ft TPT are shown in figure 4 along with facility modifications. Major components consisted of a large-chord, swept, supercritical, LFC airfoil model that spanned the full test section height, a contoured test section liner, facility disturbance suppression devices, and a model suction system. Photographs of the installed liner and model are shown in figure 5.

The following sections provide brief descriptions of the major components of the experiment.

Wind Tunnel

The Langley 8-Foot Transonic Pressure Tunnel (8-ft TPT) is a continuous-flow, variable-pressure wind tunnel with controls that permit independent variations of Mach number, stagnation pressure and temperature, and humidity. The standard test section is square with filleted corners and a cross-sectional area approximately equivalent to an 8-ft-diameter circle. The floor and ceiling of the test section are axially slotted to permit a continuous variation of the test section Mach number from 0.20 to 1.30.

Tunnel stagnation pressure can be varied from a minimum of about 0.25 atm at all test Mach numbers to about 1.50 atm at transonic speeds and to about 2.00 atm at Mach numbers of 0.40 or less. Tunnel air is dried until the dew point is reduced enough to prevent condensation. Temperature is controlled with water from an outside cooling tower circulating through cooling coils across the corner of the tunnel circuit upstream of the test section.

Wind-Tunnel Model

The LFC model was mounted vertically with 23° of sweep and extended through the test section liner from ceiling to floor about 10 ft forward of the regular test section (fig. 3). The model location (discussed later) was chosen to minimize viscous blockage, diffuser losses, and tunnel-wall boundary-layer radiated noise and to allow unrestricted development of the supersonic zone in the flow field above the upper surface.

Capability was provided to make small angle-of-attack changes up to $\pm 2^\circ$ about the quarter-chord in a plane normal to the leading edge.

Wind-Tunnel Liner

To meet special requirements for the large-chord, laminar-flow-control experiment, the conventional

slotted test section was reshaped with a contoured, solid wall liner. The 54-ft liner extended from the tunnel contraction region (the 24-ft tunnel station) through the test section and into the diffuser (the 78-ft tunnel station). The 50-ft tunnel station in the liner coordinate system corresponds to the slot origin of the 8-ft TPT slotted test section. The shape of the contoured liner conformed to the computed streamline flow field around the wing at the design lift coefficient, Mach number, and Reynolds number. Reference 16 discusses the analytical design of the liner.

Sonic Choke Devices

To prevent facility-generated pressure disturbances from feeding forward into the test section, an adjustable sonic throat consisting of two-dimensional, adjustable, sonic choke plates located on the liner along opposing sidewalls (fig. 6) was included as part of the liner design. These sonic choke devices were located about 1 chord downstream of the model trailing edge between the test section and the diffuser.

References 15 through 19 discuss the need for such choke devices, the demonstrated value of such devices, and flow quality measurements in the standard 8-ft TPT configuration.

Wind-Tunnel Screens and Honeycomb

Disturbances such as pressure and vorticity fluctuations propagating downstream through the settling chamber were reduced by a honeycomb and five screens installed in the settling chamber. (See fig. 4(a).) Design considerations for flow-quality devices and evaluation of the screen-honeycomb configuration are given in references 20 through 22.

Model Suction System

Laminar-flow control by boundary-layer removal on the slotted configuration was achieved with suction through closely spaced slots (fig. 7) extending spanwise on the airfoil surface. After passing through the slots and small underlying plenums, the air passed through appropriately spaced metering holes and was collected by spanwise ducts of constant cross section with circular or two-dimensional suction nozzles located at the ends. Air from the nozzles passed through model evacuation lines, through airflow control boxes that controlled the amount of suction to the individual duct nozzles, through variable nozzles, through hoses to a collector manifold, and, finally, to a 10 000-ft³/min (CFM) compressor with a 4.5:1 compression ratio which supplied the suction.

For low test Reynolds numbers, the tunnel circuit had to be evacuated to very low stagnation

pressures. For example, for $R_c = 10 \times 10^6$ and $M_\infty = 0.82$, stagnation pressure was about 0.33 atm. The pressure on the model upper surface was even lower since the local static pressure at design conditions ($M_{\text{local}} > 1.0$ in supersonic bubble) was approximately one-half the stagnation pressure (i.e., $p_{\text{local}}/p_{\text{stagnation}} = 0.528$ for $M_{\text{local}} = 1.0$). Because of this, the 4.5:1 compression ratio, 10 000 CFM compressor was exhausted to the stagnation pressure of the tunnel circuit instead of to outside ambient conditions, as shown in figure 4(b).

In the normal operation of the tunnel, the 10 000 CFM compressor exhaust would be vented to the atmosphere through an automatic modulating valve to maintain a constant stagnation pressure (constant Reynolds number) against piping and access hatch leaks. It was impossible in this experiment, however, to do this and simultaneously satisfy the suction requirements for the reasons outlined above. Therefore, an auxiliary 2000 CFM compressor was installed to balance the tunnel stagnation pressure against leaks.

Laminar-Flow-Control Airfoil Design

Design Cycle

The design and optimization of the laminar-flow-control (LFC) airfoil required iteration cycles using advanced computer codes to analyze the aerodynamics, the surface mass transfer and displacement thickness effects, and the stability of the boundary layer. The application of advanced codes was expected to reduce the uncertainties associated with the design of suction systems and to improve the determination of the suction flow requirements.

A block diagram of the iterative design cycle is shown in figure 8 with illustrative outputs from the various codes. The design approach utilized a transonic-airfoil analysis code (ref. 23), a swept-wing boundary-layer code (ref. 24), and stability theories (refs. 25 through 28) for prediction and optimization of suction requirements. Successive computations were made to optimize the combination of design Mach number, lift, and airfoil thickness at $R_c = 20 \times 10^6$. The three-dimensional, boundary-layer analysis code (ref. 24) was modified to include the effects of local mass transfer and computation of boundary-layer displacement thickness. This code, in combination with the transonic airfoil analysis code (ref. 23), permitted the analysis of transonic flow and three-dimensional boundary-layer parameters over an infinite-span, yawed LFC airfoil. Combining results from the boundary-layer analysis with the stability codes provided the required suction rates. Solutions of the stability codes were based on

the fixed-frequency, or envelope, method for various types of local boundary-layer instabilities in the different regions of the airfoil upper and lower surfaces.

Theoretical Pressure Distributions

The LFC wing was designed for shock-free flow at a high free-stream Mach number with lift performance comparable to that of current turbulent supercritical airfoils. The intent was to design a laminar-flow-control airfoil that retained the advantages of a supercritical airfoil while minimizing boundary-layer instability problems and, thus, suction requirements by suitable choices of geometry and pressure distribution.

The "near-final," shock-free design pressure distribution and sonic lines normal to the leading edge for the resultant airfoil (as calculated with the analysis code of ref. 23) are shown in figure 9. Various types of boundary-layer instabilities considered in the design process are indicated. Also included in figure 9 is a high-lift, off-design pressure distribution. Earlier design efforts are reported in references 10 and 11 with comparisons of numerical results presented in references 12 and 13.

The airfoil analysis code of reference 23 did not include provisions for a laminar boundary layer; and, in view of the extremely thin laminar boundary layer expected with suction, the flow was treated inviscidly by assuming zero displacement thickness up to the point of specified transition. Transition was specified during design to occur near the end of the laminar test regions—96 percent chord on the upper surface and 84 percent chord on the lower surface. Suction did not extend completely to the trailing edge of the upper surface because of the high suction requirements and marginal benefits and because the trailing edge was extremely thin (0.020 in.). Suction was not required over the aft region of the lower surface for several reasons: (1) the adverse pressure gradients in the concave region tended to generate crossflows opposite in circulation to those generated in the favorable pressure gradient regions, thus minimizing suction requirements; (2) Taylor-Görtler instability was controlled by geometric shaping (discussed in later sections) rather than by suction; and (3), perhaps the most practical reason, there was no room for lower-surface suction ducts beyond 84 percent chord.

The airfoil thickness was reduced in the front and rear by undercutting the lower surface to optimize lift (for a given thickness and Mach number) or Mach number (for a given thickness and lift) and to reduce pitching moments. The center of the airfoil provided bending strength and torsional stiffness without any significant lift contribution. This concept provided

less pitching moment than conventional aft-loaded supercritical airfoils.

Undercutting the forward lower surface also produced a low-velocity region of near-constant pressure coefficient that was conducive to laminar flow without suction. This procedure also reduces sensitivity to surface roughness which might permit laminar flow over local surface discontinuities associated with leading-edge devices such as Krueger flaps.

As discussed in reference 10, the upper-surface pressure distribution was characterized by a steep acceleration around the leading edge (because of the relatively sharp and specially designed leading edge) followed by a gradual and progressively slower deceleration to about 40 percent chord. Over the mid-chord region, the pressure gradient was near zero. Downstream of the 70 percent chord, the flow decelerated progressively more rapidly through a steep subsonic pressure rise toward the trailing edge in a manner similar to a Stratford-type pressure recovery. The rear transition from supersonic to subsonic flow was located in a region of relatively strong surface curvature. This location better ensured a gentle slope of the sonic line toward the upper surface around 80 percent chord and thus delayed the onset of shocks in this particularly critical region. The supersonic zone on the upper surface thus extended over about 80 percent of the airfoil chord, and the maximum local Mach number reached about 1.11. This was greater both in extent and magnitude than that measured in flight on either the F-94 or X-21 (refs. 3 and 4).

As discussed in reference 2 and in later sections of this report, crossflow disturbance growth was believed to depend more on the time spent in a pressure gradient than on the steepness of the gradient. Growth thus may be minimized by confining steep gradients to short distances along the chord. Consequently, steep gradients are indicated in the four regions labeled "crossflow" in figure 9.

On the lower surface, the flow accelerated rapidly around the small leading edge toward the concave region at high static pressure with a local deceleration at about 10 percent chord. The flow then accelerated rapidly in a second acceleration to sonic velocity in the midchord region. The small pocket of supersonic flow in the midchord region was followed by a Stratford-type rear pressure recovery to a high static pressure in the rear concave-curvature region. The flow finally accelerated to the trailing-edge static pressure.

A small-chord (0.109c) trailing-edge flap provided pressure distribution and lift control at off-design conditions. Calculations of lift recovery by flap deflection (in the event of suction failure and/or loss

of laminar flow on an earlier configuration (ref. 11)) indicated that the flap was very effective in recovering a pressure distribution similar to the design-point pressure distribution.

As noted in reference 2, feasibility of the LFC airfoil depended on the ability to maintain laminar flow in the concave-curvature regions on the lower surface where centrifugal Taylor-Görtler (T-G) type of boundary-layer instabilities dominate. In a manner similar to crossflow disturbances, Taylor-Görtler disturbance growth depends more on the time spent in a concave-curvature region than on the magnitude of the curvature. One technique for minimizing the growth of T-G instabilities was to turn the flow through a given angle over the shortest possible chordwise distance in the concave-curvature regions at one or more "corner" locations instead of using a gradual turn over a longer chordwise distance. As a result, the two concave regions on the lower surface had local regions of high curvature, and two dips, labeled "Taylor-Görtler instabilities," appear in the pressure distribution of figure 9.

To provide suitable computational resolution to analyze spikes in the pressure distribution at such "corners," the incompressible Eppler code (ref. 29) was used with extra grid points in the low-speed flow of the fore and aft concave regions of the lower surface. These corners and the resulting pressure spikes were then superimposed on the "near-final" calculations of figure 9, and the "final" composite design pressure distribution is shown in figure 10. The resulting airfoil profile is shown in figure 11 and the coordinates are presented in table I. As described in reference 13, there were two concave corners in the front region and two in the rear region where boundary-layer suction was provided to prevent laminar separation. There were four additional concave corners in the region downstream of where the suction ended.

Theoretical Shock-Free Limits

Since the airfoil was designed with a large, shock-free, supersonic zone, the local flow was sensitive to changes in the external flow conditions (ref. 30). Conceptual design and off-design transonic potential flow analyses (ref. 10) indicated that shock-free, full-chord laminar-flow airfoils appeared feasible at the design point and possibly within a narrow off-design operating range.

Reference 2 summarizes previous successful experimental research involving laminarization with suction in the presence of shock boundary-layer interaction without flow separation at supersonic speeds. Based on this earlier work and unpublished analyses, suction laminarization appeared practicable in

regions of weak shocks on transonic airfoils. Apparently, the pressure rise that a laminar boundary layer can negotiate in the region of an incident shock wave decreases with increasing Reynolds number unless the thickness of the upstream boundary layer can be reduced in some manner (by suction, for example). Quantification of the suction requirements for boundary-layer control in such shock-interaction regions requires experimentation.

A summary of the variation of lift coefficient with Mach number normal to the leading edge, as calculated by the two-dimensional analysis code of reference 23, is shown in figure 12 for various combinations of angle of attack and flap deflection. The solid lines through open symbols are fairings of shock-free flow limits for constant flap deflection. Outside any of these limit lines either in increasing $c_{l,N}$ or M_N , an irregularity or discontinuity in the theoretical pressure distribution was deemed to be indicative of a flow condition that would rapidly deteriorate into a shock, thus rendering suction laminarization difficult. The design point ($M_N = 0.755$ and $c_{l,N} = 0.55$) selected for the experiment is shown in figure 12 with a solid circle symbol. The solid diamond symbol in figure 12 is the high-lift, off-design case from figure 9. Figure 12 probably represents a somewhat optimistic view since the results are based on an inviscid analysis.

At the design Mach number, the height-to-length ratio of the supersonic bubble above the upper surface was limited to about 0.35. Limitations that may be imposed by the model supersonic-bubble/tunnel-wall interaction were evaluated and are shown in figure 12 by the dashed curve.

Stability Analysis

Analysis and control of boundary-layer stability is especially difficult in high-speed flight where flow over sweptback wings must be considered.

Boundary-layer instabilities that can occur on swept wings are leading-edge attachment-line instability, inflexional or crossflow instability, Tollmien-Schlichting tangential instability, and Taylor-Görtler instability that is associated with surface concavity. These various instabilities are dependent on geometry and are normally analyzed separately although mutual interactions are possible. For example, in transonic flow, crossflow disturbances may superimpose with weakly amplified oblique Tollmien-Schlichting waves in the flat, midchord, pressure gradient regions on wings causing the crossflow vortices to be distorted three-dimensionally and thus be stretched and convected downstream. This resulting nonlinear interaction of Reynolds stresses in the two disturbance modes will cause the crossflow

vortices to grow substantially faster than those predicted by linearized disturbance theory. Therefore, the permissible degree of any one type of instability must be reduced when considering the possibility of interactions since analysis of their interdependence is not well-established (ref. 31).

Initially, the linearized, incompressible, boundary-layer crossflow stability codes of references 25 and 26 were used in the design cycle (fig. 8) to calculate integrated disturbance amplifications of the crossflow (CF) and Tollmien-Schlichting (T-S) boundary-layer disturbances. Later, these calculations were verified using the more advanced linear incompressible and compressible codes of references 27 and 28. Figure 13 is a summary of the boundary-layer stability analyses conducted at design conditions based on reference 27. It shows the maximum-disturbance amplitude ratios ($n = \ln a/a_0$) calculated in the nose, midchord, and aft regions of the upper and lower surfaces. The results are based on solutions obtained by the "envelope method" and are presented as the variation of n_{\max} with frequency f or normalized wavelength λ/c in each region of the airfoil. In the nose and aft regions where crossflow instabilities dominate, the curves for n_{\max} are the envelopes of maximum amplification rates for different wavelengths. In general, the most amplified rates were found for $f = 0$, which is similar to results found for the earlier low-speed LFC airfoil designs in reference 2.

Upper surface. Leading-edge contamination, or spanwise-turbulence contamination, refers to the instability of the spanwise boundary layer which is formed along the wing stagnation or "attachment line." This attachment-line instability was minimized on the model by limiting the attachment-line Reynolds number $R_{\theta,al}$ to less than 100 by choice of a moderate leading-edge sweep angle and by reducing the leading-edge radius and unit Reynolds number.

Because of transverse pressure gradients on swept wings, a boundary-layer crossflow component develops in the direction normal to the local potential-flow streamline. This crossflow profile has an inflection point that is strongly destabilizing (inflexional instability). Crossflow instability is associated with strong pressure gradients and predominates in the four regions of rapidly accelerating and decelerating flow indicated in figure 9.

Long extents of pressure gradients on swept wings result in the development of large crossflow velocities and large crossflow-disturbance amplification rates. These crossflow instabilities can be reduced, however, by increasing the steepness of the gradients and thereby thinning the boundary layer. In the

leading-edge region of the upper surface, crossflow was minimized by rapidly accelerating the chordwise flow from the stagnation point to the pressure minimum by use of a sharp leading edge. Restricting the leading-edge sweep and unit Reynolds number to moderate values also had a favorable effect on reducing crossflow instabilities. Because of these steps taken to minimize crossflow effects at the leading edge, suction in the immediate leading-edge region was not required for any but the highest design Reynolds number R_c of 40×10^6 , where a small suction spike is shown (fig. 14). Since a Reynolds number of 40×10^6 would have been in the short-term operating envelope of the tunnel because of overheating limitations, no provision was made for suction in the leading-edge region.

Tollmien-Schlichting instabilities dominated over the midchord region of the upper surface where there was a slowly decelerating supersonic flow followed by a relatively flat pressure distribution. These instabilities were minimized by the flatness of the pressure distribution, and their growth was controlled by modest amounts of suction over the upper surface to about 60 percent chord. Since the crossflow in the leading-edge region of the airfoil is concentrated over a very short chordwise distance and decays rather rapidly in the slowly decelerating downstream flow, the interaction of crossflow disturbances with Tollmien-Schlichting disturbances in the extensive flat-pressure midchord region of the upper surface appeared insignificant (ref. 10).

The airfoil design located the rear upper-surface pressure rise rather far downstream and increased the pressure gradient toward the trailing edge. In this region, the maximum crossflow velocity occurs closer to the surface (compared with the leading-edge crossflow profile) and the crossflow was more stable here than over the leading-edge region. This combination of adverse pressure gradient and crossflow resulted in increased suction requirements in the rear upper-surface region (fig. 14).

The indicated maximum-disturbance amplitude ratios on the upper surface (fig. 13) appeared acceptable when compared with previous swept LFC airfoil models tested in wind tunnels at low speeds (ref. 2). Compressibility effects were seen to reduce n_{\max} significantly in the midchord (T-S) region with minor favorable effects in the CF regions. This result indicated that the suction requirements as determined from incompressible calculations were conservative estimates. Therefore, the final LFC airfoil suction-system design was based on incompressible calculations.

Lower surface. On the lower surface, crossflow instabilities were alleviated over the forward region by providing steep accelerations around the leading edge and in the second acceleration near 20 percent chord. The steep acceleration at the leading edge resulted from the sharp leading edge, and the steep acceleration near 20 percent chord resulted from the choice of airfoil geometry. In addition, the decelerations in the two corners ahead of 20 percent chord caused a crossflow in the opposite spanwise direction that tended to cancel or compensate for the crossflow generated by the second acceleration. As a result, no suction was required for the control of crossflow instability in the lower-surface forward region.

Similarly, the crossflows in the steep acceleration and deceleration in the lower-surface aft region tended to offset each other and to minimize suction requirements for crossflow control in that region.

The incompressible stability results for the lower surface were similar in level and trend to those for the upper surface and again indicate that suction requirements in the forward and aft regions may be conservative. Laminarization of the LFC airfoil lower surface depended more strongly, however, on the suction control requirements of the more dominating centrifugal instabilities in the concave-surface regions referred to as "Taylor-Görtler instabilities" (refs. 32 and 33).

Results from linearized analyses (refs. 32 and 34) of the T-G instability presented in reference 35 were used to determine amplification factors for the lower-surface concave regions. Figure 15 (taken from ref. 35) shows the variation of the linearized maximum growth factor B with the Görtler parameter G for disturbances with and without asymptotic area suction. Suction tends to pull the T-G vortices closer toward the wall where stronger viscous forces dampen their growth. By using values of B between the theoretical curves shown in figure 15, calculated values of G based on airfoil-surface radius of curvature, and calculated boundary-layer parameters, the T-G vortex maximum growth rates in the concave regions were obtained from the following equation:

$$n_{\max} = \int_{(x_N)_1}^{(x_N)_2} \left[\frac{(\beta\theta R_\theta)_{\max}}{\theta R_\theta} \right] dx \quad (1)$$

As noted in the derivation of the "final" composite design pressure distribution, turning of the flow in the lower-surface concave-curvature regions (fig. 10) through several "corner" locations was believed to minimize growth of the T-G vortices. Consequently, such corners were analyzed instead of the usual gradual turn over a larger chordwise distance. Figure 16

shows representative values of n_{\max} with small incremental turns of the flow $\Delta x/c$ based on the Blasius and asymptotic suction amplification rates shown in figure 15.

According to reference 10, the wave number of the most amplified T-G vortices is relatively large for the large values of G in short chordwise-distance turns or "corners" of small radii. This leads to small vortex wavelengths and vortex heights from the surface (ref. 34) when compared with those of a longer, more gradual turn through the same angle. With potentially smaller T-G vortices, sufficient damping due to dissipation in the corners may tend to minimize overall growth of the disturbances. The insert in figure 16 illustrates typical variations of normalized curvature c_N/r with x/c for several possible increments of turn. Even though the Görtler number G and local growth rate B of the T-G vortices with a sharp turn of small radii are large, the integrated growth rate n_{\max} may be seen to decrease as the radius of concave-surface curvature decreases.

Since the flow decelerates as it approaches the concave "corner" regions of the model, increased local suction is required to prevent laminar separation. Values of $n_{\max} = 2.5$ to 4.0 based on the approach described above for T-G instabilities have been obtained in the front and rear concave regions of the LFC airfoil. The increased suction associated with these corners appeared as local spikes in the suction distribution. However, although disturbance amplitude may have decreased locally in the region of increased suction at each corner, the general trend was for disturbance amplitude to grow throughout the concave region and reach a maximum amplitude at the end of the concave region. The region of concave curvature in the forward lower surface was followed by a strongly favorable pressure gradient and a convex-curvature midchord region that tended to dampen disturbance growth.

In the aft concave region, six such corners were incorporated (fig. 11(c)). Two were located in the suction zone, each followed by a slightly convex turn (a slightly negative turning angle). There were four additional concave corners in the rear where no suction was provided ($x/c > 0.84$). Spikes occurred in the pressure distribution for the first two corners (fig. 10) but not for the last four, because, as mentioned earlier, a turbulent boundary layer was assumed in the region $x/c > 0.84$. Details of the concave corners are presented in reference 13.

Drag Divergence

During airfoil design, emphasis was placed on achieving a high drag-divergence Mach number M_{DD} for the chosen thickness ratio and lift coefficient in

order to reduce sweep for a fixed free-stream Mach number. For the design $(t/c)_N = 0.130$, the theoretical supercritical LFC airfoil had a M_{DD} comparable with that of supercritical turbulent airfoils (fig. 17).

Laminar-Flow-Control Model Suction System

Airfoil Suction Requirements

Model laminar region. Figure 14 shows the theoretical chordwise suction distribution over the upper and lower surfaces in terms of the suction coefficient C_Q for several Reynolds numbers. Suction in the laminar test region extended from 2.5 to 96.2 percent chord on the upper surface and from 5.0 to 84.1 percent chord on the lower surface.

These suction distributions represent the minimum levels calculated to control disturbance growth and maintain laminar flow. Evaluation of suction distributions was accomplished by combining them with the pressure distributions as iterative input to the conservative, linearized, incompressible stability calculations previously discussed. Calculated suction requirements were based upon continuous area suction over the surface. The results shown in figure 14 are based on maximum amplification or n -factors of e^5 to e^7 for crossflow and Tollmien-Schlichting boundary-layer disturbances on the upper surface and $e^{4.5}$ to $e^{6.5}$ on the lower surface. For Taylor-Görtler instabilities on the lower surface, n -factors of $e^{2.5}$ to $e^{4.0}$ were assumed. Based on a summary of the state-of-the-art application of stability theory to laminar-flow airfoils using suction (ref. 36), these maximum amplification factors were believed to be reasonably conservative for a tunnel with the disturbance levels expected for this experiment ($u'/U_\infty < 0.05$ percent).

Suction in the immediate leading-edge region was omitted because of the small leading-edge radius and pressure distribution selected to minimize crossflow-disturbance growth rates. Increased suction was required in the upper, aft pressure-rise region and in the decelerated-flow regions of the lower-surface concave regions.

During the hardware design phases, the continuous suction distributions shown in figure 14 were integrated over the chordwise extent of each duct and a discrete suction level was assigned to each duct. These integrated distributions (shown in fig. 18) were used to design the suction system hardware of the model and also were used as guidelines for setting suction levels during the experiment.

Model turbulent region. As discussed in a previous section, the tunnel-wall boundary layer

developed wedge-shaped regions of turbulent flow on the airfoil surface near its juncture with the wall (fig. 19). These wedge-shaped turbulent zones originated at the juncture of the wing leading edge and liner and were assumed to propagate from the local streamwise direction at a 10° angle. These required increased suction levels to avoid separation in the rear pressure-rise area. Because of this variation in spanwise suction, with more suction required toward the ends of the model, separate suction controls were designed for the laminar test zones on the upper and lower surfaces and for the turbulent wedge zones at the floor and ceiling ends of the model. This was accomplished with bulkheads in the model suction ducts that approximated the turbulent wedge boundaries and separated the laminar regions on both surfaces from the turbulent regions and allowed proper accountability of the suction drag. Suction may have been avoided in the turbulent regions with suitable geometric changes of the airfoil. However, such geometric changes were not investigated nor incorporated in the model since they would have unduly complicated model design and construction and increased model cost. Instead, flaps and collar suction were included to maintain two-dimensional constant lift across the span.

Figure 20 shows the spanwise design suction distributions for the upper and lower surfaces at several chordwise stations. The design values of suction in the turbulent zones are shown as multiples of the suction values in corresponding laminar zones. A 2-D boundary-layer analysis was used to evaluate the suction required in the turbulent zones to avoid flow separation. In general, the suction levels in the laminar zones extended the full span to about 60 percent chord on the upper surface and to about 15 percent chord on the lower surface before increased suction in the turbulent zones was required. On both surfaces, laminar suction levels extended into the turbulent zones before increasing rapidly to the turbulent level.

Slot Design

Minimum profile drag would be expected with a well-designed continuous-suction surface. A large number of discrete slots, which closely simulated continuous suction, would be expected to approach minimum profile drag. The tendency would be toward a reduction in profile drag with an increasing number of slots since the average boundary-layer thickness would decrease with decreasing slot spacing. More closely spaced slots would also enhance flow stability with reduced local suction and less variation of boundary-layer thickness. However, from the more practical standpoint of fabrication, structure, and hardware, it was desirable to reduce the number of

slots to a minimum. Design criteria from previous experiments and from some analyses were utilized to minimize the number of slots without inducing slot wake-flow fluctuations and with negligible sink effects on the boundary layer during passage from one slot to the next.

Analysis. The equations used for slot spacing Δc and sucked height z were derived by equating the suction flow rates at the surface to the flow rates within the slot in a manner similar to the earlier approach described in reference 2. The expression derived and used for the slot spacing was defined as

$$\Delta c_N = \frac{c_N R_s \left(\frac{T_w}{T_\infty} \right)^{0.73}}{C_Q R_c} = \frac{R_s \left(\frac{T_w}{T_\infty} \right)^{0.73}}{C_Q R_{ft}} \quad (2)$$

Equation (2) was applied with the restrictions that $s < 0.4h$ and $1.3 < s/z < 1.4$ to minimize the influence of slot wake-flow oscillations in the plenums and the boundary-layer streamline interaction at the downstream lip of the individual slots (ref. 37). The integrated averages of suction distributions over the ducts (fig. 18) were used in equation (2) to size the slot spacing.

Extensive suction significantly reduces local boundary-layer thickness but can lead to transition because of roughness effects; insufficient suction leads to instability. Accordingly, the sucked height z of the boundary layer can be critical in the slot design for the required suction rates to maintain laminar flow. The sucked height is defined as

$$z = \left(\frac{T_w}{T_e} \right)^{1.23} \frac{2R_s}{\bar{\tau}_w R_c} \left(\frac{1 + \frac{\gamma-1}{2} M_\infty^2}{1 + \frac{\gamma-1}{2} M_e^2} \right)^{0.73 - \frac{1}{2(\gamma-1)}} \quad (3)$$

where

$$\tau_w = \bar{\tau}_w \rho_\infty U_\infty^2$$

Values of z were restricted to about one-fifth of the boundary-layer thickness.

In general, z/s should be on the order of 1, the pressure drop through the slot must be compatible with the plenum metering-hole configuration and duct pressure levels, and the slot-spacing Reynolds number should be limited to small values. For the present model, maximum pressure drop through the plenum metering holes was limited to about 2 percent of the free-stream dynamic pressure to avoid back flow oscillations through the slots that could create boundary-layer disturbances. The effect on slot width for a given chord and unit Reynolds number condition can be shown from equations (2) and (3).

In general, representative values in equations (2) and (3) indicate that slot widths on a typical, full-scale LFC transport wing ($c \approx 20$ ft) would be greater than those for the present LFC airfoil model.

Slot geometry. By using the calculated suction requirements shown in figure 18, the upper- and lower-surface slot width, spacing, and internal-suction air-flow metering system of the LFC airfoil were designed for a 50-percent, off-design oversuction capability. The spanwise running slots had sharp lips and varied in width from 0.0020 to 0.0063 in. They extended in the chordwise direction from 2.5 to 96.2 percent on the upper-surface central flap region and from 5.0 to 84.1 percent on the lower surface. In the spanwise regions on the two intermediate and outer flaps, the upper-surface slots did not extend chordwise beyond the flap hinge line. Slot width and spacing are presented in table II. The higher suction levels required in the upper, aft, pressure rise region, in the decelerated-flow region of the lower-surface concave region, and in the turbulent wedge regions near the ends of the model were achieved with more closely spaced slots and metering holes, as well as through duct/nozzle arrangement and sizing.

Slot plenum. Laminar boundary-layer oscillations and transition can result from suction-induced disturbances at high Reynolds numbers. Therefore, consideration was given to slot-plenum geometry to prevent slot wake-flow fluctuations due to oscillating slot wakes in the small plenum chambers beneath the slots. This was accomplished by proper selection of plenum chamber height and plenum metering-hole diameter and spacing for the design surface-pressure drop. Other considerations were fabrication problems and maintenance of the surface to prevent clogging.

In principle, parameters for slot design are the slot Reynolds number R_s , the sucked height z , the pressure drop through the slot, and slot spacing. Figure 21 shows experimental limits based on unpublished measurements made during this design effort and limited results represented in reference 37 for the variation of the ratio of plenum height to slot width h/s with slot Reynolds number for several limiting metering-hole geometries. In general, R_s should be as small as possible to avoid viscous slot wake-flow oscillations. For constant slot width, the results shown in figure 21 also indicate that very shallow plenums would be required at high values of R_s . Such shallow plenums cause fabrication and maintenance problems, especially for small-scale models. The LFC airfoil design criteria are indicated by the hatched region for $10 < h/s < 20$ and $R_s < 150$ with two spanwise rows of metering holes located on opposite

sides of the shallow plenum beneath each slot with diameters less than 0.020 in. and spaced 0.50 in. or less apart. Such a plenum metering-hole configuration resulted in more uniform spanwise suction and was less sensitive to internal duct noise and chordwise displacement of the holes than single rows of holes aligned with the slots (ref. 37).

Suction Nozzle Design

Volume limitations inside the LFC airfoil model and requirements for maintaining very low duct velocities necessitated the design and application of both circular and 2-D suction duct nozzles to remove and measure suction flow rates. Figure 22 shows sketches of both nozzle types. The circular nozzles provided a smooth inlet flow followed by a straight section beginning at two throat diameters downstream from the lip. The 2-D nozzles had a transition section where the shape changes from rectangular to circular. The nozzle half height ($h/2$) and total width depended on the duct dimensions in which they were installed. Nozzle sizes were selected by limiting maximum flow velocity to 250 ft/sec to avoid choking and duct pressure oscillations. All nozzles were calibrated for flow coefficient variations with Reynolds number based on diameter so that mass flow rates could be measured during the experiment. Each duct and nozzle throat contained a static pressure orifice to measure the absolute and nozzle-duct differential pressures. These were used along with the calibrated nozzle flow coefficient to calculate mass flow rates of each duct during testing.

Laminar-Flow-Control Model Design and Fabrication

Slotted Surface Structure

Laminar-flow-control demands stringent manufacturing and structural requirements to achieve smooth surfaces and provide minimum weight structures for plenum chambers and ducts. If suction velocities and slot Reynolds numbers are kept low, rather simple suction slots can be cut into a thin outer skin bonded to a substructure.

Structural features. Figure 23 shows a cross-sectional view at midspan of the 7.07-ft-chord, swept, LFC airfoil model. The model was assembled with an aluminum wingbox to which six individual aluminum panels (three upper-surface and three lower-surface) were attached (fig. 23(a)). The upper-surface suction panels were assembled using spliced joints and were fastened to the wingbox from the underside to minimize steps or gaps on the upper surface. The three lower-surface panels were fastened directly to

the wingbox. Suction ducts (fig. 23(b)) were machined into the panels and suction slots were cut into a 0.032-in-thick external aluminum skin bonded to the outer surface of each panel.

All three upper-surface panels and the forward lower-surface panel were protected by infusing the aluminum surface with polymeric particles (TUFRAM¹ coating), thus forming a hardened surface that minimized corrosion and damage during installation and testing. The surfaces of the mid and aft lower-surface panels were not hardened since they were not considered as critical to surface erosion as the forward and upper-surface panels.

The trailing edge of the model consisted of a 10.9-percent-chord, five-segment flap from which loads were transferred through the aft panels to the central wingbox structure. This five-segment flap system included a central laminar suction flap with a 13.6-in. span and two separate nonsuction flaps on either side of the central flap. Segmentation of the flap compensated for aerodynamic decambering across the span of the airfoil model because of turbulent wedges originating from the leading-edge wall junctures. The central laminar-zone flap had a deflection range from -2° to 2° in 0.04° increments (positive, trailing edge down in a plane normal to the leading edge). The intermediate flaps had a deflection range from -2° to 4° in 0.20° increments; and the outer, fully turbulent flaps had a deflection range from -2° to 6° in 0.40° increments.

Figure 24 shows detailed segments of the LFC airfoil surface and its internal suction system in the model leading edge and central trailing-edge suction flap. Slot widths and spacing, slot plenums, metering holes, and collector ducts were sized for suction capability 50 percent above the design suction requirements. This system provided the removal of local boundary-layer air through both discrete spanwise ducts with constant cross section and suction nozzles located in the ends of the ducts. The spanwise ducts were designed to minimize pressure variations along the duct length by accounting for momentum and friction forces. A significant feature was that the design maximum duct velocity—except for the small limited-volume rearward ducts—is less than 50 ft/sec.

Fabrication process. A surface finish compatible with the thickness of the thin laminar boundary layer was necessary to maintain laminar boundary layers with surface suction. Indeed, smoothness requirements, which influence the manufacture and maintenance of low-drag airfoils, have always been

¹ TUFRAM: Registered trademark of General Magnaplate Corporation.

important (ref. 2). Experience and analysis (ref. 10) indicate that because of the large region of near-sonic flow on the upper surface of supercritical airfoils, surface tolerances for the LFC airfoil should be more stringent than those of more conventional models. Although definite surface-finish specifications are not available for high subsonic speeds, considerable effort was spent to improve fabrication and assembly techniques, and the model surface was hand polished until it was judged to be aerodynamically smooth.

Suction panels, attachment fittings, and internal ducting were fabricated from large aluminum billets with numerically controlled milling machines (fig. 25). Plenums and metering holes were machined and drilled perpendicular to the surface contour on a specially developed surface table/machine assembly equipped with overhead semiautomatic cutting and drilling tools (fig. 26). The panels were then chemically cleaned and a 0.032-in-thick sheet of aluminum alloy was bonded to the panel to form the outer surface. Discrete spanwise 0.0020- to 0.0063-in-wide slots were cut through the 0.032-in-thick bonded skin over the center of each plenum using special jeweler's circular-saw blades. Surface contour accuracy of the suction panels was routinely checked after each major fabrication process to ensure that the final shape adhered to the required tolerances.

To assure proper mating, various components were assembled during fabrication. The photographs in figure 27 show assemblies of the three upper-surface suction panels to the wingbox (fig. 27(a)) and the lower forward and center surface panels without a trailing-edge flap (fig. 27(b)). The width of the wingbox extended chordwise over the model midregion and contained internal stiffeners and access holes. Tunnel floor and ceiling attachment beams are shown at one end of the wingbox. When installed in the tunnel (fig. 28), the wingbox rotated about a spanwise line located near the quarter-chord station to provide small angle-of-attack adjustments. Each flap on the five-segment flap assembly could be independently deflected. The entire model, with flap assembly, was assembled and mated before it was installed in the tunnel; the final assembly was made during installation. During preinstallation assembly, the panels were hand polished to ensure overall surface smoothness, particularly along the joints.

Surface tolerance. Since pressure coefficients are proportional to local flow inclinations, or the surface slope divided by the Prandtl factor $(M^2 - 1)^{1/2}$ in supersonic flow,

$$C_p \propto \frac{2}{(M^2 - 1)^{1/2}} \frac{dy}{dx}$$

airfoils with large regions of near-sonic velocity are particularly sensitive to surface waviness (refs. 10 and 11). Under such conditions, small waviness may (1) cause enough of a decrease in local external pressure to induce outflow through the slots, (2) change the pressure distribution such as to influence growth of boundary-layer disturbances, or (3) generate a pressure wave that reflects from the sonic line onto the airfoil surface and induces transition.

To evaluate the effects of waviness on the LFC model, inviscid calculations were made using the transonic analysis code of reference 23 with a 320-point grid around the airfoil. A local surface wave was introduced by small changes in the upper-surface coordinates, and the resulting pressure distribution was then examined to see if the effects were acceptable. The resultant variation of permissible amplitude ratio h/λ for multiple waves on supercritical LFC airfoils is shown in figure 29 as a dashed line. An empirical expression derived from previous "X-21 criteria" data (refs. 38 and 39)

$$\frac{h}{\lambda} = \left[\frac{59\,000 \cos^2 \Lambda}{(\lambda/c) R_c^{3/2}} \right]^{1/2} \quad (4)$$

is represented for several values of R_c by solid lines in figure 29. The symbols are wave amplitudes measured on the upper surface of the model during preinstallation assembly using a template that had been machined to the model coordinates. These measurements were considered accurate to within ± 0.0005 in. and represent "worst case" values. These measurements were made before final assembly and before the surface was hand polished.

The permissible values of wave height h would be larger for a full-scale aircraft than those for most wind-tunnel models with given values of unit Reynolds number and λ/c . This can be seen more easily by expressing the "X-21 surface waviness criteria" of equation (4) as

$$h = \frac{(59\,000 \cos^2 \Lambda)^{0.5} \left(\frac{\lambda}{c}\right)^{0.25} \lambda^{0.25}}{R_{ft}^{0.75}} \quad (5)$$

Model Suction Ducts and Nozzle Layout

Figure 30 illustrates the layout of the LFC airfoil upper-surface assembly of internal suction ducts, nozzles, and connector hoses. Calibrated nozzles were placed at the end of the ducts where needed for suction control and mass flow measurements. Also shown are typical suction connector hoses and couplings that extended from each suction duct nozzle through either the tunnel floor or ceiling. As

mentioned in the section on suction requirements, individual laminar test-region suction ducts were separated from their corresponding turbulent zone ducts by bulkheads which approximately followed the predicted turbulent wedge boundaries. Penetration holes were drilled through the ends of the ducts (fig. 31) and through the bulkheads for nozzle extensions, connector hoses, pressure orifice tubes, and electrical leads. The penetration holes were sealed around the connector hoses to prevent leakage. An access panel covering the entire underside of each panel sealed the ducts. The connector hoses, which go to the airflow control boxes located in the plenum surrounding the test section, were sized and selected so that cross-sectional-area changes due to hose deformation were no more than 2 percent at the maximum design pressure of 1.51 psi. This minimized both duct and hose pressure oscillations.

Airflow Control System External to Model

Accurate measurement and control of suction is essential for LFC testing. Suction to the model was monitored by four airflow boxes (fig. 32) connected via hoses to the suction-duct nozzles. The fifth airflow control box shown in figure 32 was dedicated to the control of the suction in the collars around the ends of the model as discussed below. The boxes contained arrays of motor-driven needle valves that were operated from a console in the control room. Each airflow box was connected downstream, through variable sonic-flow nozzles, to a 10 000 CFM suction compressor (figs. 4(b) and 32(a)). The sonic nozzles blocked acoustic disturbances from the compressor feeding back to the model. Airflow from the sonic nozzles was acquired by a collector manifold and piped to the compressor.

Airflow Boxes

Details of the airflow control boxes for the LFC airfoil are shown in figures 33 and 34. Flexible hoses run from the ends of the suction nozzles in each model suction duct, through the penetration holes in the ends of the ducts, to constant-diameter pipes located in the upstream face of each airflow control box. Each airflow control box has 27 such pipes. Inside the airflow control boxes, individual electrical motors drive shafts with needle noses (fig. 34(d)) longitudinally into the open ends of the pipes (fig. 34(e)). These needle-nose shafts act as needle valves to control the mass flow from each model suction duct. The boxes were designed to maintain low flow velocities (15 ft/sec) and contain a contraction section and several noise-dampening devices (acoustic linear, honeycomb, and screen)

that minimize disturbances generated within the airflow control boxes. Individual nozzles and associated needles were designed to control flow from about 16 percent below suction levels required at the lowest Reynolds number at which the system was to be tested ($R_c = 8 \times 10^6$) to about 20 percent above suction levels required at the highest Reynolds number at which the system was to be tested ($R_c = 40 \times 10^6$).

Sonic Nozzles

Figure 35(a) sketches the sonic nozzles located just downstream of the airflow control boxes. Photographs of the nozzles are shown in figures 35(b) and 35(c). Nozzle design was based on the "sonic plug" principle and included an electric motor-driven needle assembly very similar to those for the airflow control boxes. Motors were operated from a console located in the tunnel control room, and sonic flow at the sonic nozzle throat was achieved by adjustment of the needle longitudinal position with varying flow rates. Needle geometry and stroke were sized to produce the necessary range of mass flow rates in the airflow control box.

Tunnel Modifications

Because of the blockage associated with the large-chord LFC model, a contoured liner was incorporated in the test section. The liner was designed without slots in order to reduce the predominant acoustic disturbances associated with the slotted test section normally used to alleviate transonic blockage effects. All four test section walls were contoured not only to alleviate severe transonic blockage problems associated with the large model and eliminate the noise due to test section slots but also to correct for the interference effects of the tunnel sidewall on the crossflow in the field about the swept model, that is, alleviate model end effects.

When measurements are obtained on models whose boundary layers remain laminar over long lengths, the boundary layer must not be adversely influenced by facility disturbances (vorticity and acoustic) (refs. 14 and 15). Maximum-length Reynolds numbers at which laminar flow can be maintained by suction directly relate to background disturbance levels since disturbances influence model boundary-layer development and transition. Consequently, considerable effort was made to improve flow quality in the tunnel by adding turbulence suppression devices (honeycomb and screens) in the settling chamber and a sonic throat at the diffuser entrance to minimize upstream noise propagation.

Test Section Liner

Concept. A complex, four-wall, test section liner was designed that extended forward well into the contraction region and rearward partway into the diffuser. To reduce costs, liner contours were essentially fixed and undisturbed streamlines were precisely simulated for only one test condition ($M_\infty = 0.82$, $c_l = 0.47$, and $R_c = 20 \times 10^6$). However, small variations from design conditions were not expected to produce unacceptable variations from the computed flow field. As previously mentioned, the model was located upstream as far as possible (toward the liner contraction region) in order to minimize liner-wall boundary-layer thickness, thus alleviating viscous blockage problems, and to minimize diffuser losses. The model was displaced from the tunnel vertical centerline toward the lower surface by approximately 15 percent chord to allow development of the supersonic zone in the flow field above the model upper surface.

Since the airfoil flow field extends well ahead of the model, the liner was extended into the contraction region, and the flow field of the model was superimposed on the accelerating flow field of the contraction to determine the liner shape. In the supercritical region of the model, it was necessary for the contours of the liner walls to match the undisturbed streamlines very closely. The liner contours in this region included corrections for the variations of the displacement thickness of the wall boundary layers as they moved through the pressure gradients produced by the model.

Procedures used for liner design are outlined in figure 36 and details are presented in reference 16. For supercritical flow conditions, appropriate transonic analysis codes (refs. 40 and 41) were used to establish the desired flow field and boundary streamlines. Blockage due to viscous effects on the liner was accounted for by using a boundary-layer analysis code (ref. 42). An axisymmetric stream tube code (ref. 43) was used to analyze the contraction, choke (ref. 44), and diffuser fairings. Several other codes were developed to prepare, transfer, interface, and manipulate the large data base generated. Basically, the bounding streamlines in the desired flow field were determined in order to establish the test section shape. These bounding streamlines were then faired back into the existing tunnel walls. Assessment was then made of all viscous blockage corrections in the presence of the model pressure field and required suction distributions.

Many interactions were required in the design of the liner (ref. 16) to match the contours of the existing tunnel and to meet constraints imposed by

the liner itself. Figure 37 is a scaled illustration of the relative size of the LFC airfoil model, its embedded 3-D supersonic flow regions, and the liner shape near the model.

Figure 38 is a sketch showing side and top views and representative cross sections of the liner contours. The rapid contraction-section shape changes from circular to rectangular with corner fillets and represents about a 27-percent increase in the original contraction. The increased tunnel-liner contraction ratio (from approximately 20:1 to 25:1) and the need for a wall choke at the downstream end of the test section required a longer diffuser. The requirement for a longer diffuser was another reason for the LFC model being located well upstream of the normal slotted test section. The test section liner contour extended downstream of the model (see fig. 3) and produced a smooth fairing into the existing diffuser. For a swept airfoil at lift, streamlines split at the leading edge and are displaced in the spanwise direction at the trailing edge (fig. 39). The cross-sectional views shown in figure 38 illustrate the steps (shelves) in the liner floor and ceiling downstream of the model caused by this displacement.

Liner/collar suction. As previously discussed and shown in figure 19, turbulent wedges (10° from local streamline direction according to ref. 45) developed on the ends of the model. These turbulent wedges, in combination with the turbulent boundary layer on the liner walls at the ends of the model, were expected to disrupt the stability of the boundary layers in the model laminar test zones. To prevent this disruption and to keep the turbulent boundary layer on the liner from separating at the juncture of the model and liner, suction was applied through slots in a collar around the ends of the model. (See fig. 40.) The plenums, metering holes, ducting, suction nozzles, and evacuation hoses were similar to those of the model suction system already discussed. The collar slots, approximately 0.025 in. wide, were wider than those on the model surface.

Both viscous and suction displacement corrections were determined by a 2-D stripwise analysis on the liner using a modified finite-difference boundary-layer code (ref. 41) in the presence of the model pressure field. Suction levels were designed to prevent the turbulent boundary layer on the liner wall from separating in the adverse pressure regions near the model. The calculated suction distributions on the liner end walls, above and below the LFC airfoil, are presented and discussed in reference 16.

Liner hardware. Figure 6 shows an upstream view of the liner installed in the tunnel with the model and downstream choke plates in place. Cutouts in

the liner floor and ceiling liner around the ends of the wingbox (fig. 28) allowed room for installation of the suction collar ducts after attachment of the six panels and flaps to the wingbox. The liner contour was constructed of rigid foam material bonded to plywood backing. It was divided into approximately 100 blocks with the windward sides contoured by numerically controlled milling machines (fig. 41) and instrumented with pressure orifices. The individual blocks were mounted on a substructure welded to the tunnel walls (fig. 42). The collar suction ducts with surface slots were located adjacent to the airfoil in the collar around the ends of the model at the tunnel floor and ceiling (fig. 40). The joints between the contoured foam blocks were filled and sealed for smoothness.

Flow Quality Modifications

Previous experiments (refs. 1 and 2) at subsonic speeds have shown that the maximum laminar-flow-length Reynolds number with suction critically depends on the characteristic disturbance level and frequencies (broadband) present in wind tunnels used for low-drag airfoil testing. For example, the data in figure 43 for both airfoils and bodies of revolution show that when either distributed suction (refs. 1, 4, and 46) or area suction (ref. 47) was used to remove the slower boundary-layer particles near the surface, the logarithm of transition-length Reynolds number was inversely proportional to the logarithm of u'/U_∞ . In addition, the values of R_c obtained with laminar-flow control were significantly higher than those reported in the literature without suction control. In particular, figure 43 illustrates that tunnels with low turbulence levels are required to achieve extensive laminar flow on airfoils at the high chord Reynolds numbers approaching flight conditions. Thus, if acceptable flow quality cannot be realized in the tunnel, achievement of high transition Reynolds numbers for low-drag airfoils may not be possible.

Achievement of low levels of disturbance becomes increasingly difficult in moving from subsonic to transonic speeds in a wind tunnel. The ability to simulate a free-air environment is hampered by the presence of stream turbulence in the tunnel, acoustical disturbances emanating from the tunnel-wall boundary layer or drive system, and mechanical vibrations (ref. 15). For the present experiment, the design-point chord Reynolds number ($R_c = 20 \times 10^6$) was chosen based on empirical predictions that disturbance levels could be reduced to $u'/U_\infty \leq 0.05$ percent. Thus, based on estimated disturbance levels attainable with proper flow treatment in the 8-ft TPT (cross-hatched band in fig. 43), the

design Reynolds number of 20×10^6 with a disturbance level of $u'/U_\infty = 0.05$ percent appeared to be conservative.

To define modifications required to achieve the desired tunnel flow quality, considerable effort was spent measuring the existing flow quality and identifying sources of major flow disturbances in the circuit of the 8-ft TPT. These critical results were documented (refs. 15 and 18) and served as a basis for pilot tests (refs. 20 and 21) conducted to provide an effective combination of honeycomb and screens in the settling chamber of the 8-ft TPT. A sonic throat or choke installed downstream of the model was also employed, as previously noted, in the LFC experiment. Discussions of these modifications are given in subsequent paragraphs.

Screens. The general disturbance level measured (refs. 15 and 18) at the turning vanes upstream of the unmodified test section at a unit Reynolds number equivalent to the design Reynolds number of the LFC experiment ($R_{ft} \approx 2.8 \times 10^6$) was $u'/\bar{u} \approx 8$ percent (fig. 44). In the settling chamber, downstream of the turning vanes, u'/\bar{u} was approximately 2 percent. Predictions (refs. 48 and 49) showed that to obtain the desired test section disturbance level of 0.05 percent or less, at least five screens with pressure drops of 2.50 psf each were necessary for the normal tunnel contraction ratio of 20:1. Research (ref. 50) has shown that screens of open-area ratios less than 0.57 tend to introduce instabilities and lateral disturbances. Much larger values, however, do not provide a sufficient drop in pressure to reduce axial disturbances satisfactorily. In evaluating the most effective combination of screens, several combinations of screen number and mesh size were investigated (refs. 20 and 21) in a pilot tunnel at full-scale Reynolds numbers. These investigations, in conjunction with the geometry of the settling chamber (ref. 50), led to the choice of five 30-mesh, stainless-steel screens with open-area ratios of 0.65. Figure 45 shows a photograph of the most downstream installed screen as viewed upstream from the test section.

Honeycomb. Screens alone are not very effective for removing swirl and mean lateral-velocity variations. Research (refs. 51 and 52) has shown that a honeycomb with a cell length at least six to eight times the cell diameter is preferable if the flow incidence does not exceed about 10° . The primary restriction on cell width is that it be smaller than the smallest lateral wavelength of the variations in velocity. Furthermore, the flow resistance coefficient of a honeycomb is usually about 0.5. This is a small number when compared with the flow resistance of

screens and does not contribute appreciably to tunnel power requirements. The selected honeycomb geometry had an open area of 95 percent with cells 3/8 in. across and 3-1/2 in. deep. The honeycomb was made of type 304 stainless steel with 0.006-in. wall thickness. The honeycomb was designed for a pressure drop of 1.25 psf.

Since significant deflection of the honeycomb under its own weight or under air loads would be undesirable, a maximum allowable deflection of 0.3 in. was specified. The installed honeycomb structure was a rigid self-supported structure; however, eight upstream tension cables distributed over the upstream face of the honeycomb and attached to the turning vanes provided additional longitudinal air load support. In general, the 36-ft-diameter honeycomb structure was fabricated by spot-welding 2-ft by 12-ft precut sections. The precut sections were matched and stacked vertically to minimize overlap of cell wall thickness and to maintain cell uniformity and straightness. Adjoining sections were spot-welded along each overlapped cell length. The honeycomb was located 2.5 ft upstream of the first screen and clamped around the edge to the settling chamber wall. Figure 46 shows photographs of the installed honeycomb with support cables.

Sonic throat. Sonic throats are well-known as effective devices for preventing the upstream propagation of diffuser-generated acoustic disturbances. Earlier flow-quality tests in the 8-ft TPT (refs. 15 and 18) utilized fixed wall chokes that reduced the test section noise level by nearly an order of magnitude. Corresponding energy spectra were reduced primarily at low frequencies. The fixed choke also was used in transition tests on a sharp cone and provided transition Reynolds numbers comparable to those in flight (ref. 19). Effects on tunnel power requirements were minimal. An adjustable choke that worked over a range of Mach numbers was designed for the LFC experiment and was an integral part of the test section liner (ref. 16).

A sketch of the liner and choke is shown in figure 47(a). Figure 47(b) shows a photograph of one of the choke plates mounted on the test section sidewall. The choke consisted of adjustable 6-ft-chord plates mounted on the vertical sidewalls of the test section downstream of the upper and lower surfaces of the model. The leading edges of the plates were located about one-half choke chord downstream of the most downstream trailing-edge location of the model. The surfaces of the choke plates were constructed of fiberglass and were designed for variable deflection toward the tunnel centerline through a piston driven by an electrically actuated bell crank with

a 10:1 mechanical advantage. The local area change, at extreme deflections, provided choked flow over a range of free-stream Mach numbers from 0.80 to 0.84. The upstream and downstream edges of the fiberglass choke plates matched the liner contour and had seals and slide joints so that the maximum deflection point occurred at the piston stroke location, that is, about 2 ft from the choke leading edge. The test section was vented to the plenum chamber surrounding the test section through porous strips (fig. 47(b)) on the surface of the choke plates, downstream of the maximum deflection point (corresponding to the location of lowest static pressure in the test section). This assures that loads on the liner are directed outward, toward the steel walls of the normal test section. The porous vent strips also help to equalize pressures across the liner during transient conditions.

Measured disturbance levels before modification and predicted disturbance levels with the honeycomb, five screens, and sonic choke are shown in figure 44. The estimated results were based on the new tunnel-liner contraction ratio of 25:1 rather than on the original value of 20:1. The combination of flow treatment (honeycomb and five screens in the settling chamber) and sonic throat was expected to reduce the overall disturbance level u'/\bar{u} in the test section region to less than 0.05 percent at $M_\infty = 0.80$. These results do not take into account any disturbances generated by the LFC model itself.

Measurements and Instrumentation

Extensive static and dynamic instrumentation were provided to establish design conditions during testing, to evaluate performance of the model during all test conditions, and to assess the effectiveness of the tunnel liner. Furthermore, dynamic measurements (ref. 53) were required to monitor transition movement and effects of both internal suction-induced and external acoustic disturbances on laminarization. This section describes briefly the measurements and instrumentation used for the various elements of the experiment.

Three types of pressure instrumentation were used. Tunnel free-stream stagnation and static pressures were measured on sonar-sensed mercury manometers that are checked daily to a precision of ± 0.2 psf.

Airfoil surface pressures, profile drag rake pressures, pressures on the tunnel choke plates, suction-duct static pressures and associated nozzle throat pressures, and all other pressures involved in monitoring the suction control system were measured with a high-speed (10 000 samples per second) electroscanning pressure (ESP) system with module limits of 2.5, 5, and 10 psi. The precision of this system

is stated as $[0.0015 \times (\text{Module limit})]/^{\circ}\text{F}$. In practice, the system was calibrated against integral standard gauges before each run and the calibration was checked for any deviations greater than 0.01 psi in the coarsest modules. Module references and size were selected, insofar as possible, to achieve maximum precision. The airfoil surface pressure, the suction-duct static pressures, and the wall-choke surface pressures were referenced to free-stream static pressure. The suction-nozzle throat pressures were connected to special 2.5-psi modules with each port separately referenced to its own duct static pressure.

Finally, the tunnel-wall liner and diffuser pressures were measured with 24 stepping valves of 47 ports each, ganged in groups of 6, for a total of 1128 ports. Again, the gauge transducer (5, 10, or 15 psi) and the reference pressures were chosen so as to achieve maximum precision, estimated to be $0.01 \times (\text{Gauge limit})$.

Real-Time Data System

From the beginning of the experiment it was realized that the design flow conditions could not be established without real-time data feedback to the tunnel and suction system operators. This was because of the continuous interaction between the exterior flow, the surface pressure distribution on the model, and the suction flow through the surface. Moreover, adjusting suction in any duct to some extent changed the suction levels in adjacent ducts and in other ducts connected to the same airflow control box.

After several modifications during early tests, the real-time system evolved to a configuration that provided instant monitoring and display of any selected pressure measurements or any computed parameters (such as free-stream Mach number and Reynolds number) on cathode ray tube screens. In addition, two real-time graphic displays provided plots, updated once a second, of streamwise airfoil pressure distribution—with the design pressure distribution displayed for comparison—at several spanwise stations. The real-time plots also displayed differences between surface and duct pressures, suction levels C_Q in the laminar zones (with the design distribution displayed for comparison), ratios of choke surface pressure to stagnation pressure (as indicators of local Mach number on the chokes), and stagnation pressure deficits across the profile drag rake.

Free-Stream Conditions

Since the walls of the tunnel were contoured to allow for the influence of the model, there could be no empty tunnel calibration. There was, therefore, no region in the flow field where undisturbed

free-stream static pressure could be measured. The theoretical pressures along streamlines derived during the liner design were examined to find a location on the liner that most nearly matched the free-stream static pressure corresponding to the design Mach number M_{∞} of 0.82. The wall static pressure tap at this location (the 36-ft, 8-in. tunnel station) was chosen to represent free-stream static pressure. (See fig. 48.) A nearby wall static pressure tap was used as a reference for various pressure-measuring devices that were referenced to free-stream static pressure. The differential pressure between the two wall taps was measured to be about ± 0.5 psf.

Aerodynamic Measurements

Surface static pressure measurements. There are 302 static pressure orifices distributed along 12 upper-surface rows and 12 lower-surface rows oriented along theoretical surface streamlines as shown in figure 49. The orifices, having a 0.010-in. inside diameter, were staggered about the streamlines to prevent wedges of orifice-generated disturbances shed by forward orifices from reinforcing each other so that orifice-induced transition would occur at a more rearward orifice. The orifices were generally centered between suction slots and were most concentrated in regions where shock waves were most likely to occur.

Profile drag rake. Drag forces on the model were determined from variations of stagnation and static pressures measured across the wake with the profile drag rake shown in figure 50. The profiles, schematically illustrated in figure 50(b), represent the momentum losses as indicated by stagnation pressure deficits across the wake.

The rake was cantilevered off the west test section wall (the wall opposite the model lower surface) in the center of the laminar-zone flap and approximately 8 in. behind the model trailing edge. (See figs. 50(c) and 50(d).) The profile drag rake had 47 total pressure orifices over a 6.2-in. span that were connected to the ESP system and referenced to free-stream stagnation pressure. There also were six static pressure orifices spread across the rake that were connected to the ESP system and referenced to free-stream static pressure. The ends of the stagnation pressure tubes were flattened and spaced closely together in the region of the wake associated with skin-friction boundary-layer losses. In addition, some of the stagnation pressure tubes in this closely spaced region were staggered off the plane of symmetry of the rake to permit closer spacing across the wake. The ends of the staggered tubes were positioned in a plane parallel to the trailing edge so that all

stagnation pressure tubes were an equal streamwise distance from the trailing edge of the model.

Dynamic measurements. Fifty flush-mounted thin-film gauges were distributed over the upper and lower surfaces (shown in fig. 49) to measure local surface heat transfer rates as indicators of whether the boundary layer was laminar, transitional, or turbulent. Signals passed through constant temperature anemometers and were recorded on a frequency-modulated recording system for post-run analysis. In addition, the dynamic output from the thin-film gauges was displayed on oscilloscopes for real-time viewing. Mounting of the plug-type acoustic gauges flush with the airfoil contour was accomplished by recessing the gauge 0.0005 in. in a predrilled hole and then "wet-wiping" a thin coat of RTV resin over the hole. The thin-film gauges were mounted in a similar fashion. All leads and tubing for the instrumentation inside the panels were brought out through the ends of the panels and tunnel walls.

Tunnel Liner and Choke

Approximately 700 static pressure orifices were located along computed streamlines distributed over the four walls of the liner (see fig. 51) from the 24-ft tunnel station at the upstream end of the contraction region to the 53-ft station immediately upstream of the movable choke plates. Approximately 240 more static pressure orifices were located on 14 streamwise rows distributed around the test section between the 53-ft and 59-ft stations in the vicinity of the choke plates. Starting at the 60-ft station and extending to the 78-ft station downstream of the choke, approximately 70 static pressure orifices were located on 4 streamwise rows near the vertical and horizontal centerline planes of the tunnel.

All liner and choke static pressures were connected to differential-pressure scanning valves referenced to free-stream static pressure. In addition, the orifices on the choke itself (three rows on the wall opposite the airfoil upper surface and three rows on the wall opposite the airfoil lower surface) were teed to the ESP system so that the pressure distribution over the choke could be displayed in real time. (See the section entitled "Real-Time Data System.")

Suction System

The following discussion on instrumentation for the suction system applies to the collar suction system as well as to the model suction system.

Ducts, nozzles, and evacuation lines. The duct temperature and static pressure and the suction nozzle-throat static pressure were required to calculate the mass flow through the ducts. Since there were regions where temperature would not vary significantly,

it was not necessary to measure temperature in every duct. Inspection of the theoretical temperature distribution at design conditions led to the installation of chromel-alumel thermocouples in 18 laminar ducts—8 on the upper surface and 10 on the lower surface—and in 15 turbulent ducts—6 on the upper surface and 9 on the lower surface. Temperatures in the bottom end of the model were assumed to be equal to those measured in the top end, and all 15 of the selected turbulent ducts were in the top end of the model. Temperatures also were measured in the collar ducts around the top end of the model.

Static pressures in the laminar-zone suction ducts were average values gathered from three static orifices drilled 6-in. apart in a steel tube affixed to the floor or side of each duct. In laminar ducts in which there were two nozzles (one in each end of the duct), static pressure was measured in front of each nozzle. Because of the shorter duct length, only one static orifice was used in the turbulent zone and collar ducts. In all, there were 135 nozzles in the model and 24 in the collars. There were, therefore, 159 duct static pressures measured, and these were measured using the ESP system.

Differential pressures across the 159 nozzles were measured by individually referenced transducers (Δp channels) in the electroscanning pressure system. The reference pressure for each Δp transducer was teed from the duct static pressure. The sensor side of the Δp transducer was connected to the static orifice in the throat of the corresponding nozzle.

Airflow control boxes and variable sonic nozzles. Static pressures in the chamber in front of the screen/honeycomb of the five airflow control boxes were measured by individual transducers and were used as indicators of the suction level. Individual transducers also were used to measure total pressures at the downstream end of the contraction region in the airflow control boxes and at the downstream end of the variable sonic nozzles. The ratio of the total pressures for each control box/nozzle pair was computed and displayed in real time to indicate the presence and strength of a shock wave in the sonic nozzle.

Positions of the 27 motor-driven needle valves in each airflow control box and of the variable sonic nozzles were monitored and controlled from a remote-control panel in the tunnel control room. Valve positions were set with individual, three-position, spring-loaded rocker switches and were displayed on edgewise panel meters graduated in percent of valve travel.

Concluding Remarks

A large-chord, swept, supercritical, laminar-flow-control (LFC) airfoil has been designed and constructed and is currently undergoing tests in the Langley 8-Foot Transonic Pressure Tunnel as part of NASA's ongoing research program to reduce drag significantly and increase aircraft efficiency. This ambitious and very complex experiment is directed toward evaluating the compatibility of LFC and supercritical airfoils, validating prediction techniques, and generating a data base for future transport airfoil designs. Unique features of the laminar-flow-control airfoil include a high design Mach number with shock-free flow and boundary-layer control by suction. Special requirements for this experiment included modifications to the wind tunnel to achieve the necessary flow quality and contouring of the test section walls to simulate free airflow about an infinite yawed model at transonic speeds. The first phase of the experiment—the evaluation of a slotted suction surface—has been completed. The second phase—the evaluation of a perforated suction surface—is currently under way. The design of the airfoil with a slotted suction surface, the suction system, and modifications to the tunnel to meet test requirements are discussed.

NASA Langley Research Center
Hampton, Virginia 23665-5225
March 7, 1988

References

1. Lachmann, G. V., ed.: *Boundary Layer and Flow Control, Volume 2*. Pergamon Press, 1961.
2. Pfenninger, Werner: Laminar Flow Control Laminarization. *Special Course on Concepts for Drag Reduction*, AGARD-R-654, June 1977, pp. 3-1-3-75.
3. Pfenninger, W.; and Groth, E.: Low Drag Boundary Layer Suction Experiments in Flight on a Wing Glove of an F-94A Airplane With Suction Through a Large Number of Fine Slots. *Boundary Layer and Flow Control, Volume 2*, G. V. Lachmann, ed., Pergamon Press, 1961, pp. 981-999.
4. Fowell, L. R.; and Antonatos, P. P.: A. Some Results From the X-21A Program. Part 2: Laminar Flow Control Flight Test Results on the X-21A, *Recent Developments in Boundary Layer Research—Part IV*, AGARDograph 97, May 1965.
5. *Aircraft Fuel Conservation Technology—Task Force Report*. OAST, NASA, Sept. 10, 1975. (Available as NASA TM X-74295.)
6. Harvey, W. D.; and Pride, J. D.: The NASA Langley Laminar Flow Control Airfoil Experiment. AIAA-82-0567, Mar. 1982.
7. Harvey, W. D.; Harris, C. D.; Brooks, C. W.; Clukey, P. G.; and Stack, J. P.: Design and Experimental Evaluation of a Swept Supercritical Laminar Flow Control (LFC) Airfoil. *Langley Symposium on Aerodynamics, Volume I*, Sharon H. Stack, compiler, NASA CP-2397, 1985, pp. 475-484.
8. Harvey, W. D.; McGhee, R. J.; and Harris, C. D.: Wind Tunnel Testing of Low-Drag Airfoils. *Laminar Flow Aircraft Certification*, Louis J. Williams, compiler, NASA CP-2413, 1986, pp. 89-128.
9. Maddalon, Dal V.; and Poppen, William A., Jr.: *Design and Fabrication of Large Suction Panels With Perforated Surfaces for Laminar Flow Control Testing in a Transonic Wind Tunnel*. NASA TM-89011, 1986.
10. Pfenninger, W.; Reed, Helen L.; and Dagenhart, J. R.: Design Considerations of Advanced Supercritical Low Drag Suction Airfoils. *Viscous Flow Drag Reduction*, Gary R. Hough, ed., AIAA, c.1980, pp. 249-271.
11. Allison, Dennis O.; and Dagenhart, John R.: Design of a Laminar-Flow-Control Supercritical Airfoil for a Swept Wing. *CTOL Transport Technology—1978*, NASA CP-2036, Part I, 1978, pp. 395-408.
12. Allison, Dennis O.: *Inviscid Analysis of Two Supercritical Laminar-Flow-Control Airfoils at Design and Off-Design Conditions*. NASA TM-84657, 1983.
13. Allison, Dennis O.; and Dagenhart, J. Ray: *Two Experimental Supercritical Laminar-Flow-Control Swept-Wing Airfoils*. NASA TM-89073, 1987.
14. Pate, Samuel R.: Effects of Wind Tunnel Disturbances on Boundary-Layer Transition With Emphasis on Radiated Noise: A Review. AIAA-80-0431, Mar. 1980.
15. Harvey, William D.; Stainback, P. Calvin; and Owen, F. Kevin: *Evaluation of Flow Quality in Two Large NASA Wind Tunnels at Transonic Speeds*. NASA TP-1737, 1980.
16. Newman, Perry A.; Anderson, E. Clay; and Peterson, John B., Jr.: *Aerodynamic Design of the Contoured Wind-Tunnel Liner for the NASA Supercritical, Laminar-Flow-Control, Swept-Wing Experiment*. NASA TP-2335, 1984.
17. Keefe, Laurence R.: *A Study of Acoustic Fluctuations in the Langley 8-Foot Transonic Pressure Tunnel*. NASA CR-158983, 1979.
18. Brooks, Joseph D.; Stainback, P. Calvin; and Brooks, Cuyler W., Jr.: Additional Flow Quality Measurements in the Langley Research Center 8-Foot Transonic Pressure Tunnel. *A Collection of Technical Papers—AIAA 11th Aerodynamic Testing Conference*, Mar. 1980, pp. 138-145. (Available as AIAA-80-0434.)
19. Harvey, W. D.; and Bobbitt, P. J.: Some Anomalies Between Wind Tunnel and Flight Transition Results. AIAA-81-1225, June 1981.
20. Scheiman, James; and Brooks, J. D.: A Comparison of Experimental and Theoretical Turbulence Reduction From Screens, Honeycomb and Honeycomb-Screen Combinations. *A Collection of Technical Papers—AIAA 11th Aerodynamic Testing Conference*, American Inst. of Aeronautics and Astronautics, 1980, pp. 129-137. (Available as AIAA-80-0433.)
21. McKinney, Marion O.; and Scheiman, James: *Evaluation of Turbulence Reduction Devices for the Langley 8-Foot Transonic Pressure Tunnel*. NASA TM-81792, 1981.

22. Scheiman, James: *Considerations for the Installation of Honeycomb and Screens To Reduce Wind-Tunnel Turbulence*. NASA TM-81868, 1981.
23. Bauer, Frances; Garabedian, Paul; Korn, David; and Jameson, Antony: Supercritical Wing Sections II. *Volume 108 of Lecture Notes in Economics and Mathematical Systems*, M. Beckmann and H. P. Kuenzi, eds., Springer-Verlag, 1975.
24. Kaups, Kalle; and Cebeci, Tuncer: Compressible Laminar Boundary Layers With Suction on Swept and Tapered Wings. *J. Aircr.*, vol. 14, no. 7, July 1977, pp. 661-667.
25. Dagenhart, J. Ray: *Amplified Crossflow Disturbances in the Laminar Boundary Layer on Swept Wings With Suction*. NASA TP-1902, 1981.
26. Srokowski, Andrew J.; and Orszag, Steven A.: Mass Flow Requirements for LFC Wing Design. AIAA Paper 77-1222, Aug. 1977.
27. El-Hady, Nabil M.: On the Stability of Three-Dimensional Compressible Nonparallel Boundary Layers. AIAA-80-1374, July 1980.
28. Mack, Leslie M.: On the Stability of the Boundary Layer on a Transonic Swept Wing. AIAA Paper 79-0264, Jan. 1979.
29. Eppler, Richard; and Somers, Dan M.: *A Computer Program for the Design and Analysis of Low-Speed Airfoils*. NASA TM-80210, 1980.
30. Spee, B. M.: *Investigations on the Transonic Flow Around Aerofoils*. NLR TR 69122 U, Natl. Aerospace Lab. NLR (Netherlands), 1970.
31. Reed, Helen L.: Wave Interactions in Swept-Wing Flows. AIAA-84-1678, June 1984.
32. Smith, A. M. O.: On the Growth of Taylor-Görtler Vortices Along Highly Concave Walls. *Q. Appl. Math.*, vol. XIII, no. 3, Oct. 1955, pp. 233-262.
33. El-Hady, Nabil M.; and Verma, Alok K.: Growth of Goertler Vortices in Compressible Boundary Layers Along Curved Surfaces. AIAA-81-1278, June 1981.
34. Kobayashi, R.: *Taylor-Görtler Instability of a Boundary Layer With Suction or Blowing*. Rep. No. 289, Inst. of High Speed Mechanics, Tohoku Univ., vol. 32, 1975, pp. 129-148.
35. Pfenninger, W.; and Syberg, J.: *Reduction of Acoustic Disturbances in the Test Section of Supersonic Wind Tunnels by Laminarizing Their Nozzles and Test Section Wall Boundary Layers by Means of Suction*. NASA CR-2436, 1974.
36. Hefner, Jerry N.; and Bushnell, Dennis M.: Application of Stability Theory to Laminar Flow Control. AIAA Paper 79-1493, July 1979.
37. Pfenninger, W.; Bacon, J.; and Goldsmith, J.: Flow Disturbances Induced by Low-Drag Boundary-Layer Suction Through Slots. *Phys. Fluids Suppl.*, vol. 10, no. 9, pt. II, Sept. 1967, pp. S112-S114.
38. Carmichael, B. H.: *Surface Waviness Criteria for Swept and Unswept Laminar Suction Wings*. Rep. No. NOR-59-438 (BLC-123) (Contract AF33(616)-3168), Northrop Aircraft, Inc., Aug. 1959.
39. Carmichael, B. H.; and Pfenninger, W.: *Surface Imperfection Experiments on a Swept Laminar Suction Wing*. Rep. No. NOR-59-454 (BLC-124), Northrop Corp., Aug. 1959.
40. Carlson, Leland A.: *TRANDES: A FORTRAN Program for Transonic Airfoil Analysis or Design*. NASA CR-2821, 1977.
41. Keith, J. S.; Ferguson, D. R.; Merkle, C. L.; Heck, P. H.; and Lahti, D. J.: *Analytical Method for Predicting the Pressure Distribution About a Nacelle at Transonic Speeds*. NASA CR-2217, 1973.
42. Anderson, E. Clay: *User Guide for STRMLN: A Boundary-Layer Program for Contoured Wind-Tunnel Liner Design*. NASA CR-159058, 1979.
43. Ferguson, D. R.; and Keith, J. S.: *Modifications to the Streamtube Curvature Program. Volume I—Program Modifications and User's Manual*. NASA CR-132705, 1975.
44. Campbell, Richard L.: *Computer Analysis of Flow Perturbations Generated by Placement of Choke Bumps in a Wind Tunnel*. NASA TP-1892, 1981.
45. Fischer, Michael C.: Spreading of a Turbulent Disturbance. *AIAA J.*, vol. 10, no. 7, July 1972, pp. 957-959.
46. Loftin, Laurence K., Jr.; and Burrows, Dale L.: *Investigations Relating to the Extension of Laminar Flow by Means of Boundary-Layer Suction Through Slots*. NACA TN 1961, 1949.
47. Braslow, Albert L.; Burrows, Dale L.; Tetervin, Neal; and Visconti, Fioravante: *Experimental and Theoretical Studies of Area Suction for the Control of the Laminar Boundary Layer on an NACA 64A010 Airfoil*. NACA Rep. 1025, 1951. (Supersedes NACA TN 1905 by Burrows, Braslow, and Tetervin and NACA TN 2112 by Braslow and Visconti.)
48. Prandtl, L.: *Attaining a Steady Air Stream in Wind Tunnels*. NASA TM 726, 1933.
49. Uberoi, Mahinder S.: Effect of Wind-Tunnel Contraction on Free-Stream Turbulence. *J. Aeronaut. Sci.*, vol. 23, no. 8, Aug. 1956, pp. 754-764.
50. Bradshaw, P.: *The Effect of Wind Tunnel Screens on "Two-Dimensional" Boundary Layers*. NPL Aero Rep. 1085, British Aeronautical Research Council, Dec. 4, 1963.
51. Lumley, J. L.: Passage of a Turbulent Stream Through Honeycomb of Large Length-to-Diameter Ratio. *Trans. ASME, Ser. D.: J. Basic Eng.*, vol. 87, no. 2, June 1964, pp. 218-220.

52. Loehrke, R. I.; and Nagib, H. M.: Control of Free-Stream Turbulence by Means of Honeycombs: A Balance Between Suppression and Generation. *J. Fluids Eng.*, vol. 98, no. 3, ser. 1, Sept. 1976, pp. 342-353.
53. Dagenhart, J. Ray; and Stack, John P.: Boundary Layer Transition Detection Using Flush-Mounted Hot-Film Gages and Semiconductor Dynamic Pressure Transducers. AIAA-82-0593, Mar. 1982.

Table I. Theoretical Coordinates of Slotted LFC Supercritical Airfoil
Normal to Leading Edge

$(x/c)_N$	$(z/c_N)_u$	$(x/c)_N$	$(z/c_N)_u$	$(x/c)_N$	$(z/c_N)_u$
0.000000	0.000000	.134371	.037292	.474029	.053239
.000126	.001024	.141029	.038014	.483529	.053238
.000389	.002089	.147817	.038723	.493030	.053215
.000795	.003181	.154734	.039418	.502527	.053170
.001349	.004289	.161778	.040100	.512015	.053104
.002052	.005406	.168950	.040768	.521490	.053015
.002910	.006526	.176244	.041423	.530948	.052903
.003922	.007646	.183656	.042061	.540387	.052769
.005088	.008757	.191183	.042684	.549803	.052613
.006406	.009849	.198823	.043292	.559194	.052435
.007888	.010911	.206572	.043884	.568553	.052235
.009549	.011946	.214430	.044459	.577880	.052012
.011397	.012964	.222392	.045019	.587168	.051766
.013434	.013967	.230455	.045561	.596415	.051498
.015651	.014950	.238617	.046088	.605618	.051207
.018055	.015916	.246871	.046599	.614772	.050892
.020650	.016867	.255218	.047093	.623874	.050553
.023433	.017810	.263652	.047570	.632921	.050191
.026399	.018749	.272172	.048030	.641910	.049806
.029546	.019678	.280774	.048470	.650837	.049395
.032873	.020598	.289453	.048892	.659698	.048960
.036384	.021511	.298206	.049295	.668491	.048501
.040071	.022420	.307031	.049679	.677212	.048018
.043934	.023324	.315924	.050045	.685858	.047511
.047966	.024221	.324881	.050391	.694427	.046979
.052169	.025110	.333900	.050719	.702914	.046424
.056541	.025989	.342975	.051028	.711315	.045842
.061081	.026859	.352105	.051318	.719626	.045233
.065787	.027723	.361284	.051588	.727844	.044595
.070656	.028577	.370509	.051839	.735968	.043930
.075686	.029423	.379778	.052069	.743999	.043238
.080875	.030257	.389086	.052279	.751931	.042519
.086223	.031082	.398431	.052469	.759761	.041771
.091725	.031897	.407807	.052639	.767487	.040996
.097378	.032701	.417210	.052788	.775103	.040192
.103182	.033494	.426639	.052917	.782607	.039358
.109136	.034277	.436089	.053025	.789998	.038493
.115235	.035050	.445557	.053111	.797275	.037591
.121473	.035810	.455040	.053175	.804442	.036651
.127851	.036557	.464532	.053218	.811497	.035676

Table I. Continued

$(x/c)_N$	$(z/c_N)_u$	$(x/c)_N$	$(z/c_N)_\ell$	$(x/c)_N$	$(z/c_N)_\ell$
.818442	.034665	0.000000	0.000000	.127835	-.025535
.825269	.033620	.000019	-.000956	.135118	-.028162
.831976	.032537	.000201	-.001824	.140594	-.030138
.838567	.031409	.000574	-.002590	.144554	-.031566
.845049	.030237	.001170	-.003259	.147525	-.032639
.851485	.029011	.002015	-.003848	.150000	-.033538
.856436	.028031	.003121	-.004375	.151980	-.034290
.861386	.027025	.004484	-.004868	.153465	-.034930
.866337	.026004	.006098	-.005328	.154950	-.035668
.871287	.024974	.007967	-.005755	.156436	-.036474
.876238	.023941	.010103	-.006161	.158416	-.037584
.881188	.022906	.012503	-.006569	.160891	-.038982
.886139	.021871	.015157	-.006988	.164067	-.040777
.891089	.020837	.018058	-.007417	.167228	-.042563
.896040	.019802	.021208	-.007857	.170464	-.044392
.900990	.018767	.024596	-.008306	.176424	-.047725
.905941	.017733	.028212	-.008760	.182162	-.050623
.910891	.016698	.032059	-.009223	.187889	-.053088
.915842	.015663	.035891	-.009673	.193737	-.055206
.920792	.014630	.036881	-.009789	.199755	-.057071
.925743	.013597	.038861	-.010021	.205949	-.058755
.930693	.012565	.042822	-.010484	.212309	-.060304
.935644	.011535	.046782	-.010948	.218818	-.061743
.940594	.010505	.050743	-.011411	.225460	-.063084
.945545	.009476	.054703	-.011874	.232232	-.064334
.950495	.008449	.058663	-.012338	.239130	-.065502
.955446	.007422	.062624	-.012801	.246151	-.066598
.960396	.006397	.066584	-.013264	.253282	-.067625
.965347	.005374	.070545	-.013728	.260515	-.068583
.970297	.004353	.074505	-.014191	.267853	-.069479
.975248	.003335	.078465	-.014654	.275295	-.070318
.980198	.002318	.082426	-.015118	.282831	-.071101
.985149	.001303	.086386	-.015581	.290451	-.071830
.990099	.000290	.090347	-.016045	.298158	-.072503
.995050	-.000721	.094307	-.016508	.305950	-.073124
1.000000	-.001730	.098267	-.016971	.313817	-.073693
		.100990	-.017290	.321752	-.074210
		.103465	-.017588	.329758	-.074677
		.105446	-.017869	.337834	-.075096
		.106931	-.018170	.345971	-.075465
		.108416	-.018584	.354164	-.075786
		.110396	-.019250	.362413	-.076060
		.113366	-.020315	.370714	-.076286
		.117327	-.021743	.379061	-.076464
		.121782	-.023350	.387448	-.076593

Table I. Concluded

$(x/c)_N$	$(z/c_N)_\ell$	$(x/c)_N$	$(z/c_N)_\ell$	$(x/c)_N$	$(z/c_N)_\ell$
.395874	-.076674	.783663	-.014176	.899010	.002938
.404340	-.076707	.793564	-.011196	.902970	.003011
.412837	-.076692	.801980	-.008663	.907921	.003101
.421361	-.076628	.807921	-.006876	.914851	.003216
.429910	-.076518	.811961	-.005661	.921782	.003291
.438482	-.076359	.815130	-.004709	.926733	.003289
.447071	-.076151	.817110	-.004114	.930693	.003235
.455672	-.075894	.818694	-.003641	.934653	.003128
.464283	-.075589	.819882	-.003298	.939604	.002929
.472903	-.075234	.821070	-.002997	.946535	.002571
.481526	-.074830	.822258	-.002750	.953465	.002174
.490147	-.074375	.823447	-.002540	.958416	.001882
.498762	-.073868	.825031	-.002280	.962376	.001647
.507372	-.073310	.826724	-.002006	.965347	.001462
.515971	-.072699	.828699	-.001686	.968317	.001263
.524552	-.072036	.830392	-.001412	.970297	.001118
.533115	-.071319	.832085	-.001137	.972277	.000958
.541656	-.070548	.833778	-.000860	.975248	.000699
.550174	-.069721	.835471	-.000582	.980198	.000240
.558658	-.068839	.837447	-.000257	.985149	-.000229
.567107	-.067899	.839140	.000021	.988119	-.000521
.575514	-.066899	.840724	.000277	.990099	-.000732
.583873	-.065836	.841912	.000456	.992079	-.000965
.592180	-.064704	.843100	.000602	.995050	-.001342
.600430	-.063497	.844288	.000701	1.000000	-.001986
.608620	-.062206	.845476	.000766		
.616747	-.060820	.847060	.000839		
.624811	-.059324	.848753	.000911		
.632822	-.057702	.850729	.000993		
.640795	-.055943	.852422	.001063		
.648750	-.054040	.854115	.001135		
.656709	-.051988	.855808	.001207		
.664701	-.049797	.857501	.001280		
.672750	-.047489	.859476	.001367		
.680868	-.045093	.861386	.001452		
.689604	-.042483	.863366	.001542		
.698515	-.039806	.866337	.001675		
.704455	-.038018	.871287	.001898		
.714356	-.035038	.876238	.002121		
.724257	-.032057	.881188	.002344		
.734158	-.029077	.886139	.002565		
.744059	-.026097	.889109	.002691		
.753960	-.023117	.891089	.002763		
.763861	-.020137	.893069	.002818		
.773762	-.017156	.896040	.002881		

Table II. Location and Width of Suction Slots on LFC Supercritical
Airfoil Normal to Leading Edge

(a) Upper surface

Duct	Slot	$(x/c)_N$	Slot width, in.
1	1	0.02475	0.0021
1	2	.04089	.0029
2	3	.05644	.0030
2	4	.07257	.0033
3	5	.08891	.0033
3	6	.10538	.0033
4	7	.12184	.0034
4	8	.13831	.0036
5	9	.15478	.0035
5	10	.17125	.0038
6	11	.18771	.0036
6	12	.20418	.0038
7	13	.22064	.0038
7	14	.23711	.0039
7	15	.25358	.0038
Joint			
8	16	.27005	.0040
8	17	.28651	.0039
8	18	.30298	.0040
8	19	.31945	.0039
9	20	.33591	.0041
9	21	.35239	.0039
9	22	.36885	.0042
9	23	.38532	.0040
10	24	.40178	.0041
10	25	.41825	.0041
10	26	.43471	.0040
10	27	.45119	.0042
11	28	.46765	.0040
11	29	.48412	.0043
11	30	.50058	.0040
11	31	.51705	.0042
12	32	.53351	.0041
12	33	.54999	.0041
12	34	.56646	.0042
12	35	.58292	.0040
Joint			
13	36	.59939	.0046

Duct	Slot	$(x/c)_N$	Slot width, in.
13	37	.61859	.0044
14	38	.63780	.0046
14	39	.65701	.0045
14	40	.67622	.0049
15	41	.69543	.0051
15	42	.71463	.0057
15	43	.73384	.0062
16	44	.74792	.0060
16	45	.75817	.0056
16	46	.76585	.0053
16	47	.77200	.0050
17	48	.77738	.0047
17	49	.78224	.0045
17	50	.78673	.0042
17	51	.79057	.0043
17	52	.79442	.0043
17	53	.79826	.0044
17	54	.80210	.0043
17	55	.80594	.0043
18	56	.80978	.0042
18	57	.81362	.0042
18	58	.81747	.0042
18	59	.82131	.0041
18	60	.82515	.0041
18	61	.82899	.0041
18	62	.83283	.0040
19	63	.83667	.0040
19	64	.84051	.0040
19	65	.84436	.0041
19	66	.84820	.0043
19	67	.85204	.0044
20	68	.85588	.0045
20	69	.85972	.0047
20	70	.86356	.0048
20	71	.86741	.0049
21	72	.87125	.0050
21	73	.87509	.0052
21	74	.87893	.0051

Table II. Continued

(a) Concluded

Duct	Slot	$(x/c)_N$	Slot width, in.
21	75	0.88277	.0049
21	76	.88661	.0054
Joint			
22	77	.89685	.0050
22	78	.90069	.0042
22	79	.90453	.0040
22	80	.90838	.0039
22	81	.91222	.0038
22	82	.91606	.0037
23	83	.91990	.0037
23	84	.92374	.0036
23	85	.92758	.0036
23	86	.93143	.0035
23	87	.93527	.0035
23	88	.93911	.0035
23	89	.94295	.0035
24	90	.94679	.0035
24	91	.95063	.0035
24	92	.95448	.0035
24	93	.95832	.0035
24	94	.96216	.0034

Table II. Continued

(b) Lower surface

Duct	Slot	$(x/c)_N$	Slot width, in.
1	1	0.05050	0.0028
1	2	.06407	.0028
2	3	.07175	.0039
2	4	.07880	.0046
2	5	.08520	.0051
3	6	.09096	.0047
3	7	.09480	.0045
3	8	.09801	.0039
3	9	.10056	.0031
3	10	.10253	.0027
4	11	.10402	.0024
4	12	.10531	.0023
4	13	.10658	.0027
5	14	.13569	.0020
5	15	.14338	.0023
5	16	.14811	.0031
5	17	.15003	.0035
5	18	.15157	.0031
5	19	.15286	.0063
6	20	.15410	.0025
6	21	.15576	.0020
6	22	.15744	.0020
6	23	.15910	.0020
6	24	.16076	.0020
6	25	.16243	.0020
7	26	.20614	.0038
7	27	.22149	.0033
Joint			
8	28	.25683	.0035
8	29	.28050	.0031
8	30	.30098	.0032
8	31	.32019	.0037
8	32	.33862	.0032

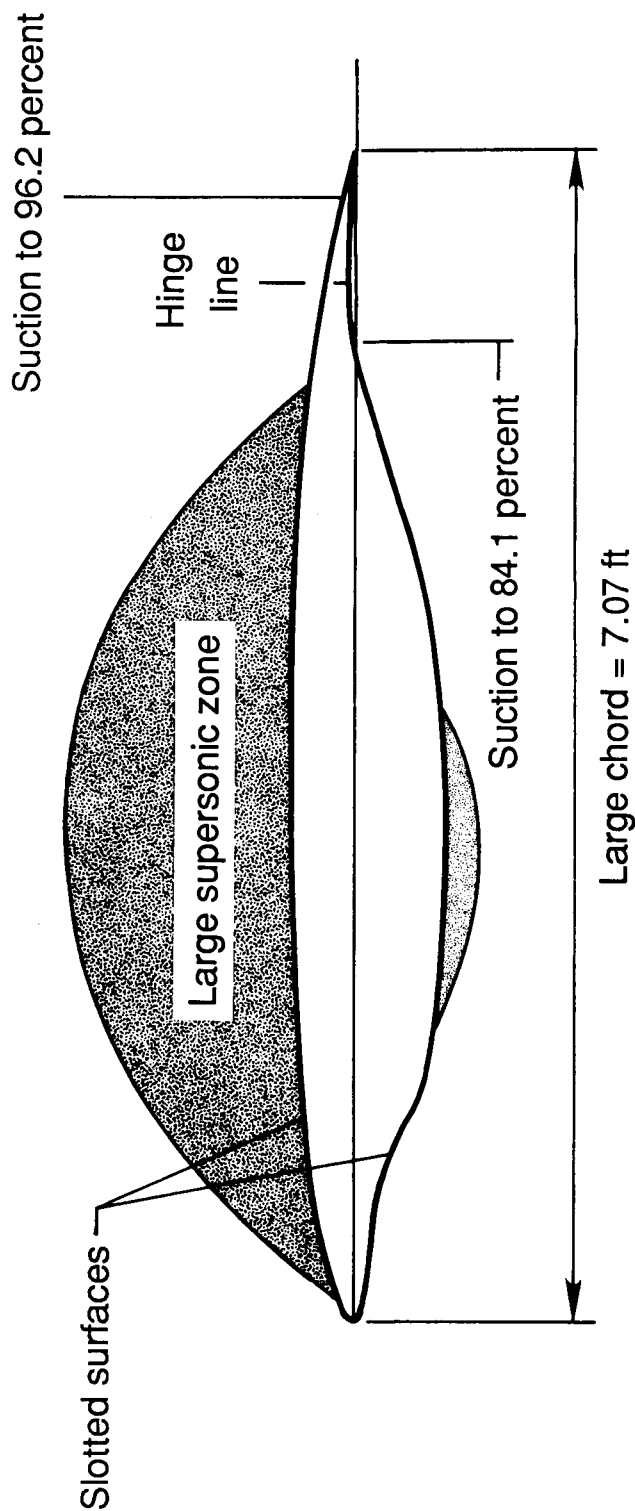
Duct	Slot	$(x/c)_N$	Slot width, in.
9	33	.35783	.0039
9	34	.37448	.0034
9	35	.38984	.0039
9	36	.40419	.0034
9	37	.41852	.0042
10	38	.43287	.0037
10	39	.44619	.0039
10	40	.45950	.0044
10	41	.47282	.0036
10	42	.48511	.0044
11	43	.49741	.0043
11	44	.50893	.0038
11	45	.52046	.0047
11	46	.53134	.0045
11	47	.54158	.0038
11	48	.54894	.0049
Joint			
12	49	.56446	.0043
12	50	.56937	.0042
12	51	.57718	.0046
12	52	.58499	.0046
12	53	.58970	.0044
13	54	.60061	.0046
13	55	.60843	.0053
13	56	.61624	.0051
13	57	.62136	.0050
13	58	.62571	.0052
13	59	.63006	.0048
13	60	.63442	.0048
13	61	.63800	.0048
14	62	.64158	.0047
14	63	.64517	.0045
14	64	.64838	.0043

Table II. Concluded

(b) Concluded

Duct	Slot	$(x/c)_N$	Slot width, in.
14	65	0.65157	0.0042
14	66	.65477	.0040
14	67	.65798	.0039
15	68	.66118	.0038
15	69	.66438	.0037
15	70	.66758	.0037
15	71	.67078	.0036
15	72	.67398	.0036
15	73	.67719	.0036
16	74	.68039	.0036
16	75	.68358	.0035
16	76	.68679	.0034
16	77	.68999	.0034
16	78	.69319	.0033
16	79	.69640	.0033
16	80	.69959	.0032
16	81	.70279	.0032
17	82	.70600	.0032
17	83	.70920	.0032
17	84	.71240	.0032
17	85	.71560	.0032
17	86	.71880	.0031
17	87	.72200	.0031
17	88	.72521	.0031
17	89	.72841	.0030
17	90	.73160	.0030
17	91	.73480	.0030
17	92	.73801	.0030
18	93	.74121	.0031
18	94	.74441	.0033
18	95	.74800	.0033
18	96	.75158	.0032

Duct	Slot	$(x/c)_N$	Slot width, in.
18	97	.75517	.0032
18	98	.75875	.0032
18	99	.76234	.0032
18	100	.76592	.0032
18	101	.76951	.0033
19	102	.77751	.0034
19	103	.78027	.0034
19	104	.78385	.0033
19	105	.78727	.0032
19	106	.79050	.0031
19	107	.79357	.0030
20	108	.79651	.0030
20	109	.79933	.0029
20	110	.80202	.0028
20	111	.80458	.0026
20	112	.80689	.0026
20	113	.80919	.0025
20	114	.81124	.0024
21	115	.81316	.0022
21	116	.81475	.0021
21	117	.81613	.0020
21	118	.81741	.0020
21	119	.81869	.0020
21	120	.81997	.0020
21	121	.83258	.0026
21	122	.83488	.0026
21	123	.83719	.0026
21	124	.83911	.0025
21	125	.84072	.0025



Free-stream design conditions

$$M_{\infty} = 0.82$$

$$\Lambda = 23^{\circ}$$

$$c = 7.07 \text{ ft}$$

$$R_C = 20 \times 10^6$$

$$c_l = 0.47$$

Design conditions normal to leading edge

$$M_N = 0.755$$

$$c_N = 6.508 \text{ ft}$$

$$R_{C,N} = 16.9 \times 10^6$$

$$(t/c)_N = 13.0 \text{ percent}$$

$$c_{l,N} = 0.55$$

Figure 1. Airfoil design parameters.

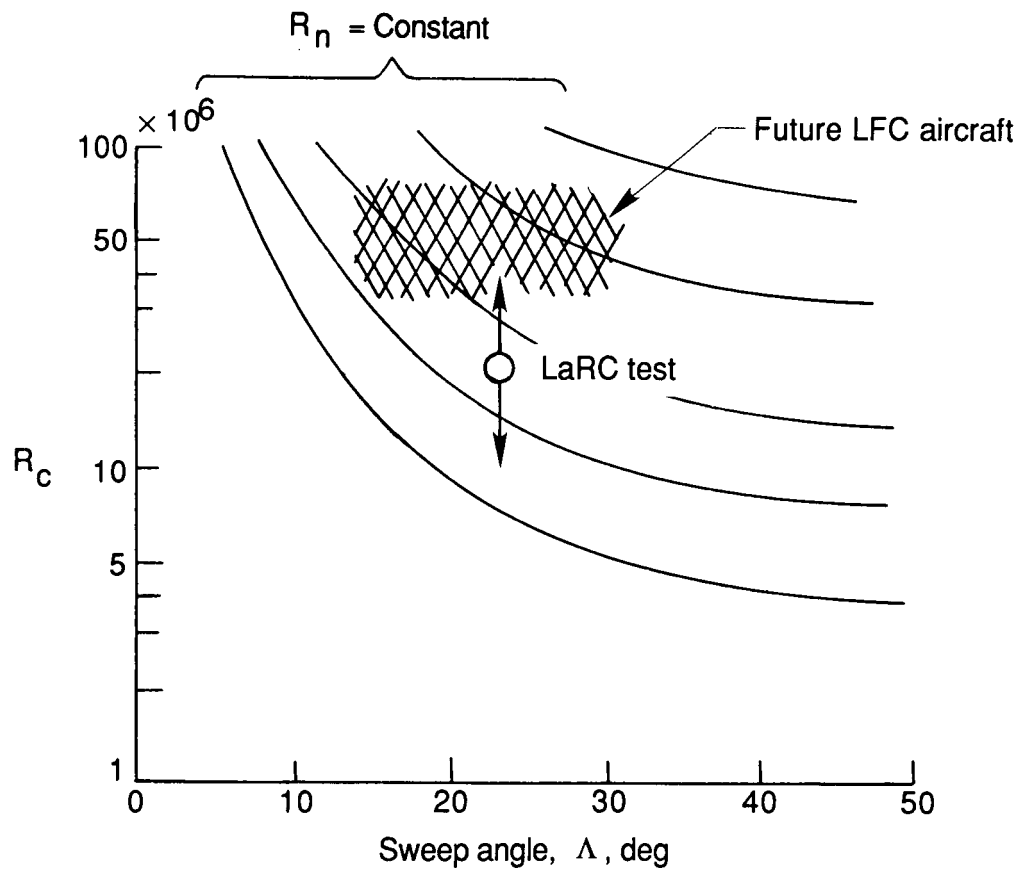


Figure 2. Variation of chord Reynolds number with sweep angle for constant crossflow Reynolds number.
 $R_n \propto \sin 2\Lambda R_c^{1/2}$.

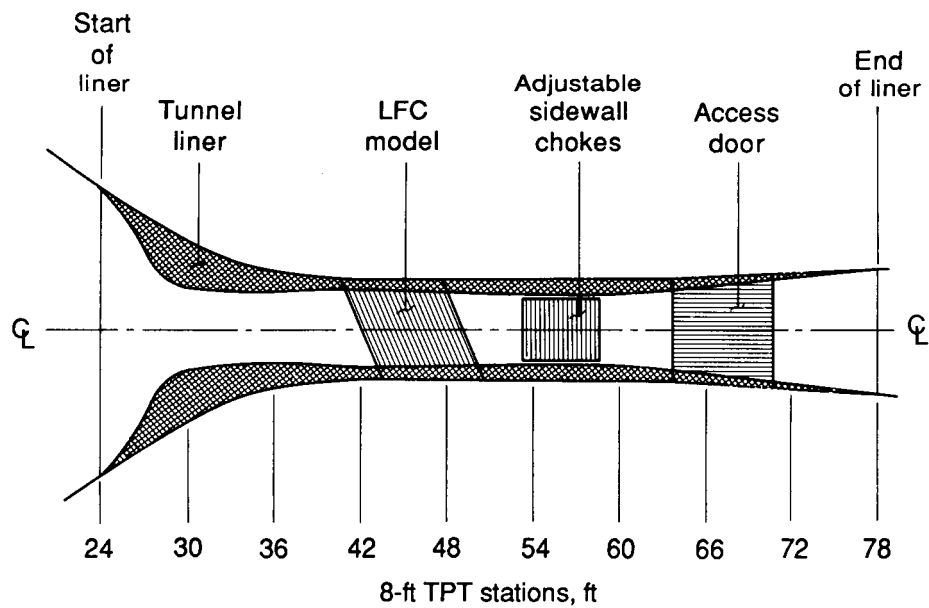
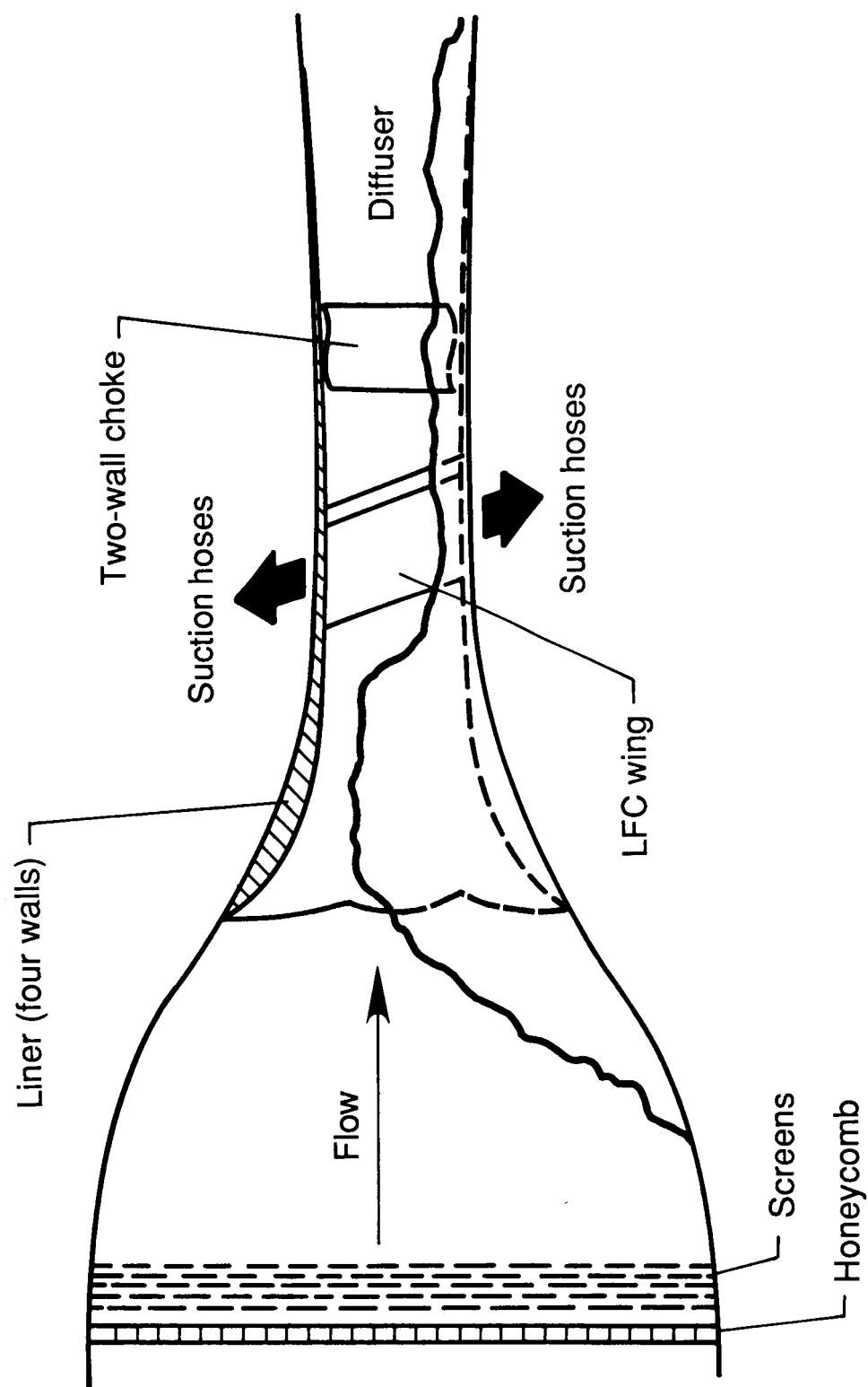
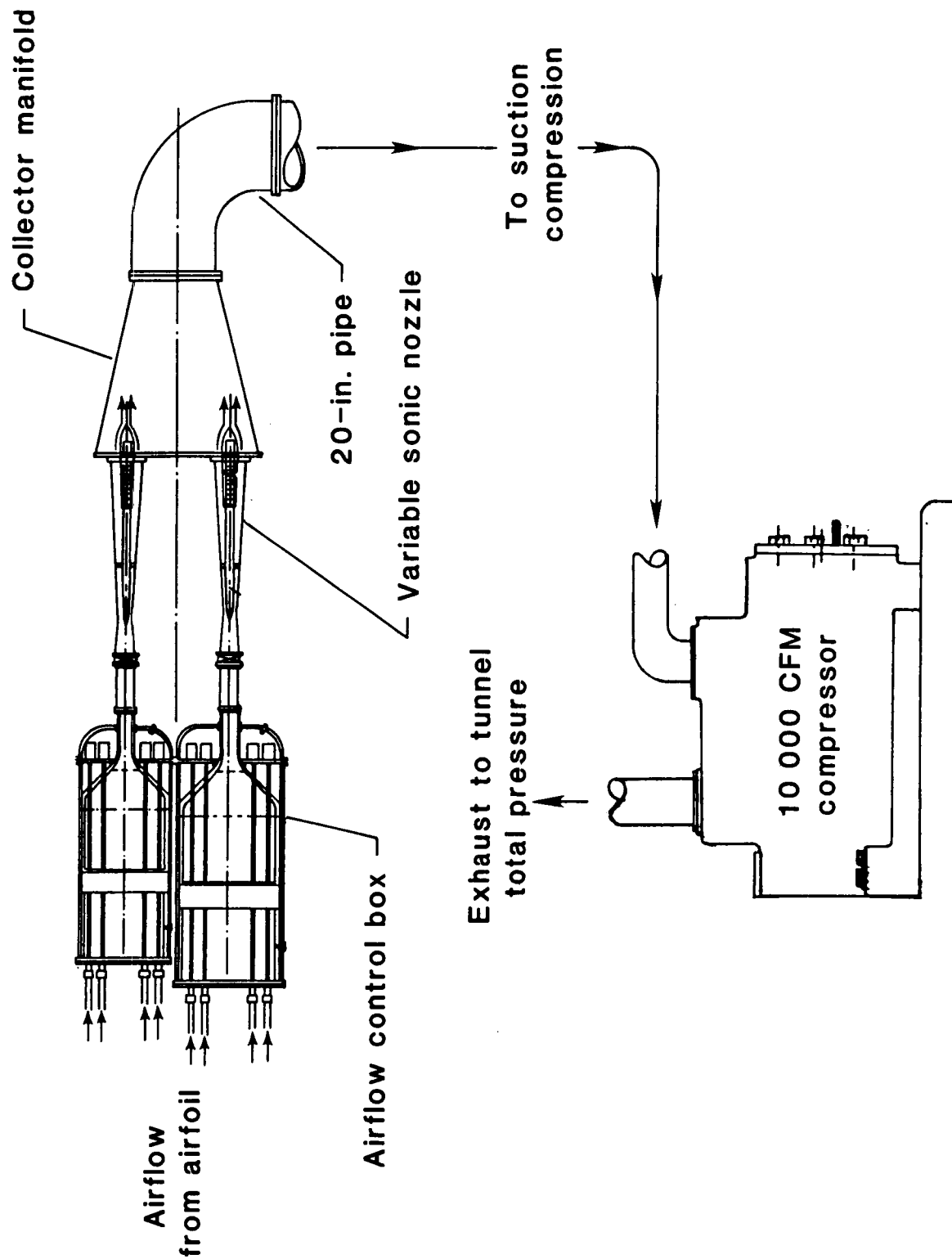


Figure 3. Test section liner.



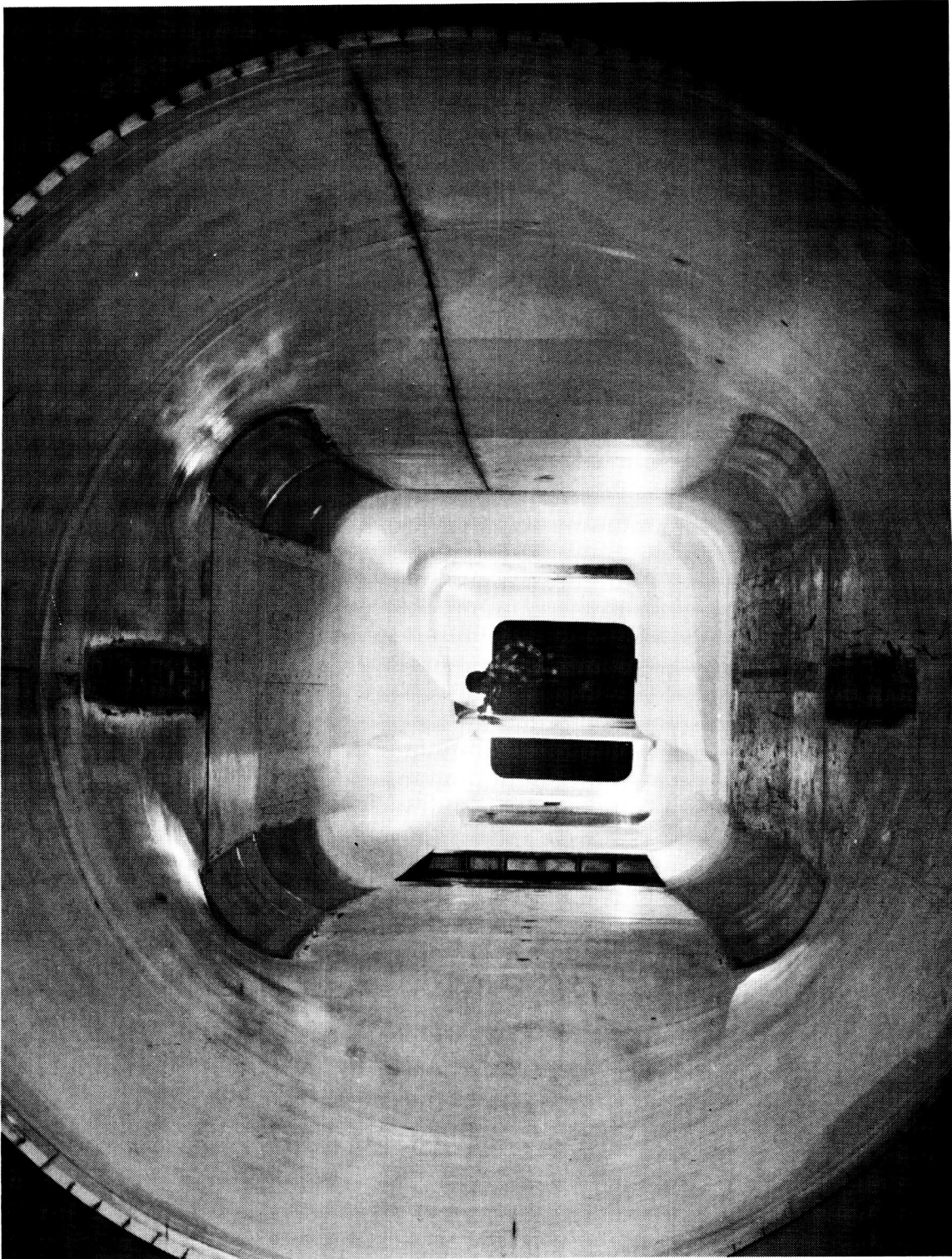
(a) Sketch of settling chamber, test section, and diffuser.

Figure 4. General test setup in 8-ft TPT.



(b) Suction airflow system.

Figure 4. Concluded.

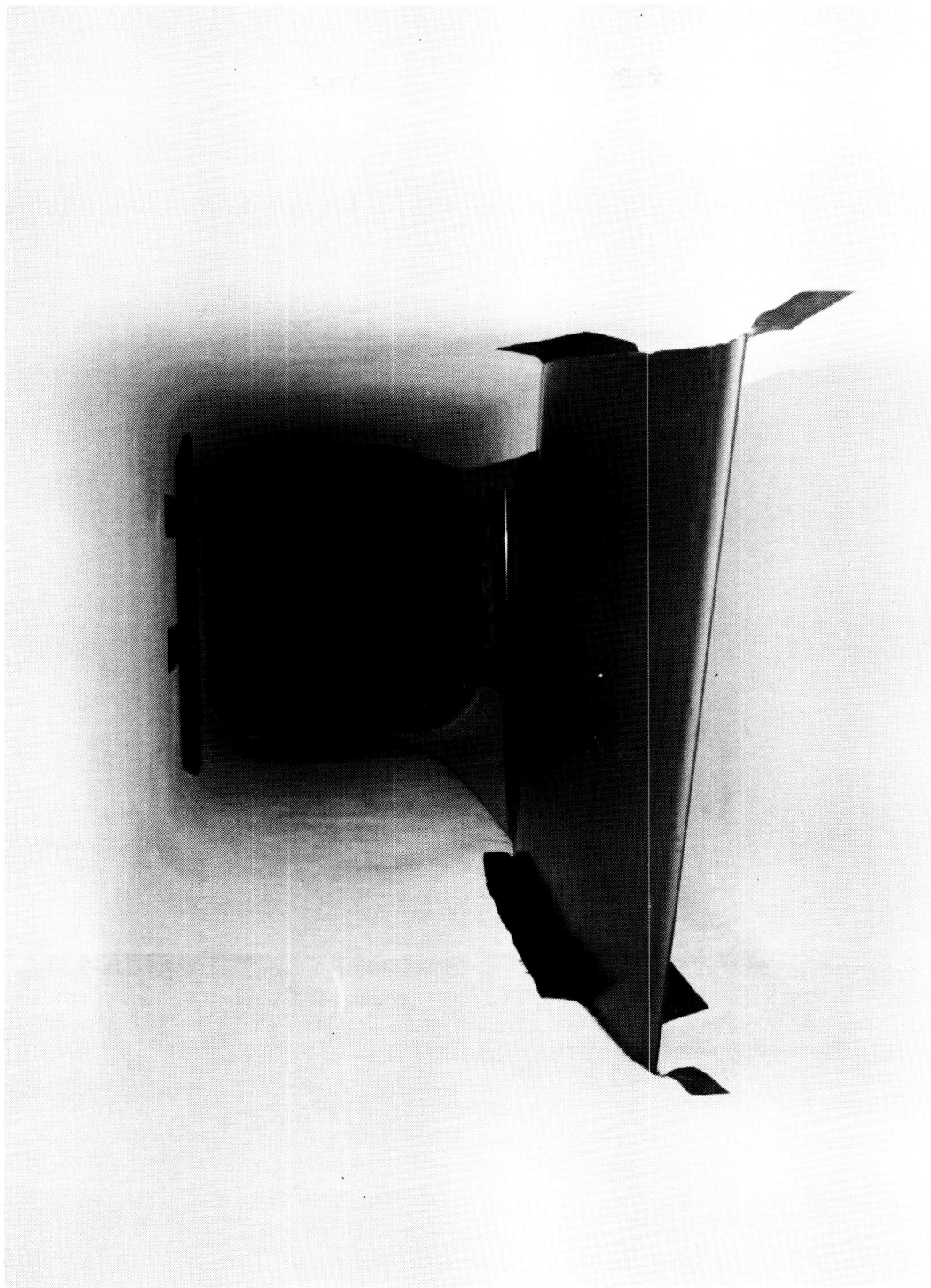


L-82-3,068

(a) Upstream view.

Figure 5. Photographs of test section liner and model.

ORIGINAL PAGE IS
OF POOR QUALITY

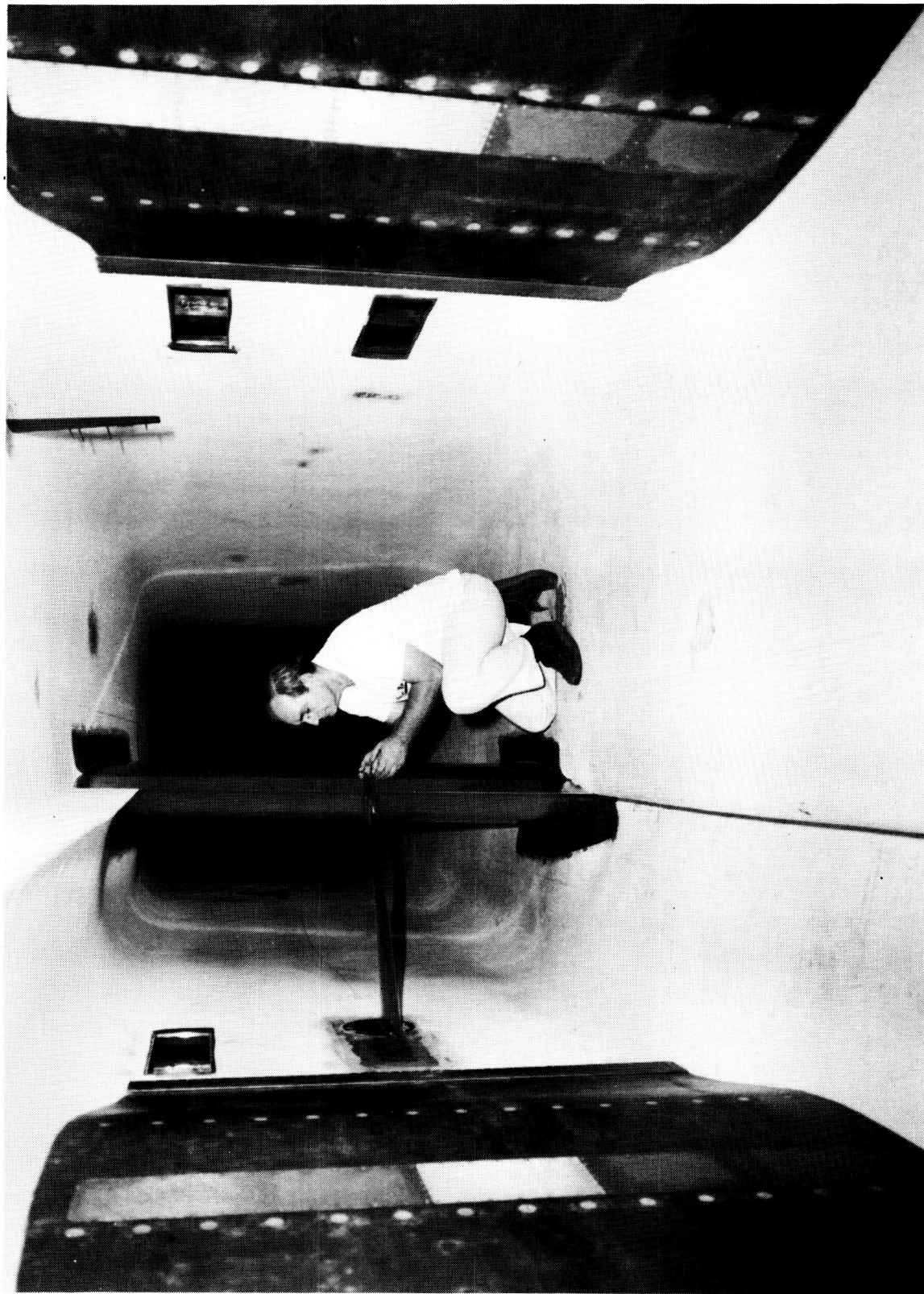


L-82-3,619

(b) Downstream view.

Figure 5. Concluded.

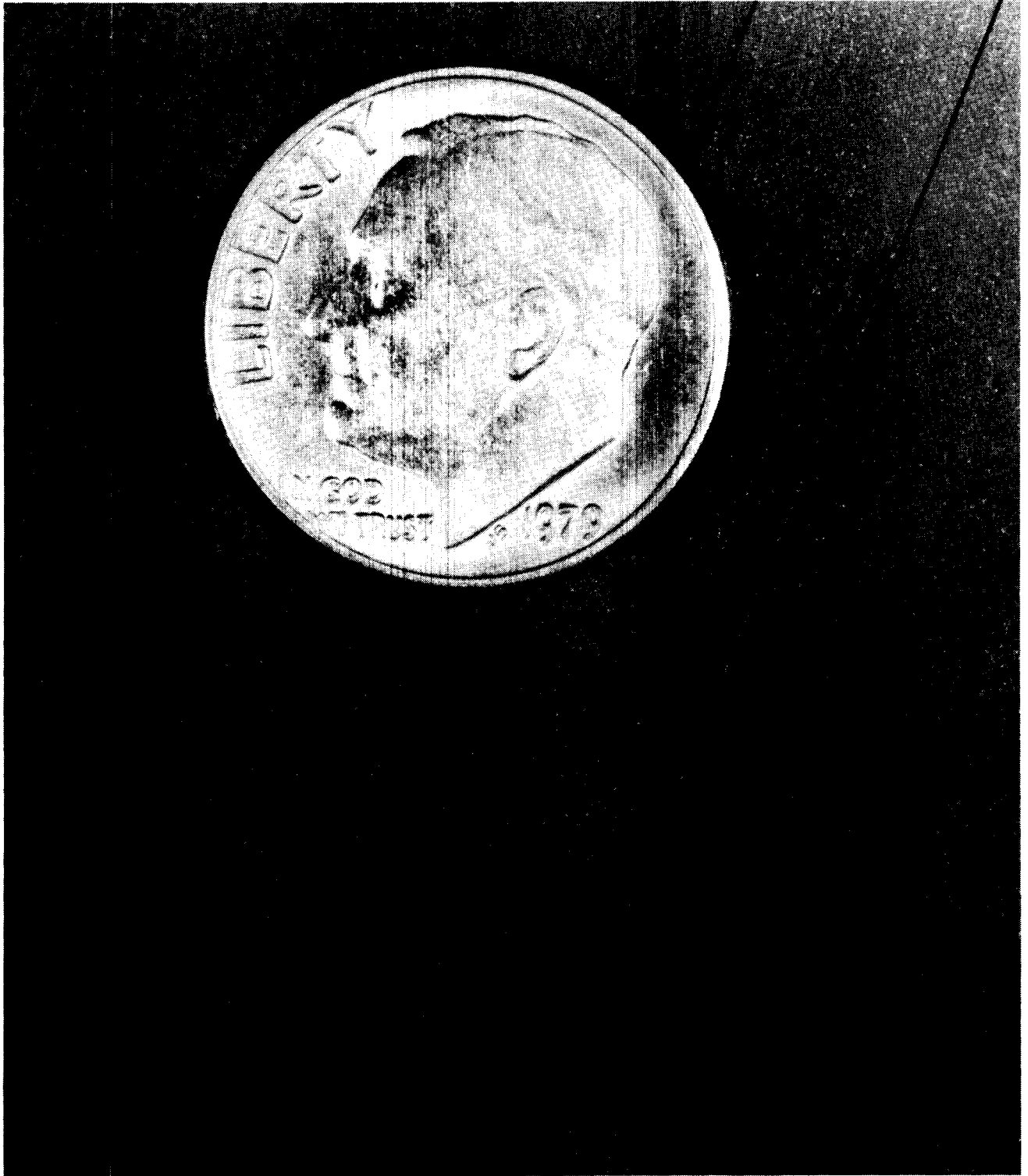
ORIGINAL PAGE IS
OF POOR QUALITY



L-82-9,339

Figure 6. Choke plates on opposing sides of test section liner.

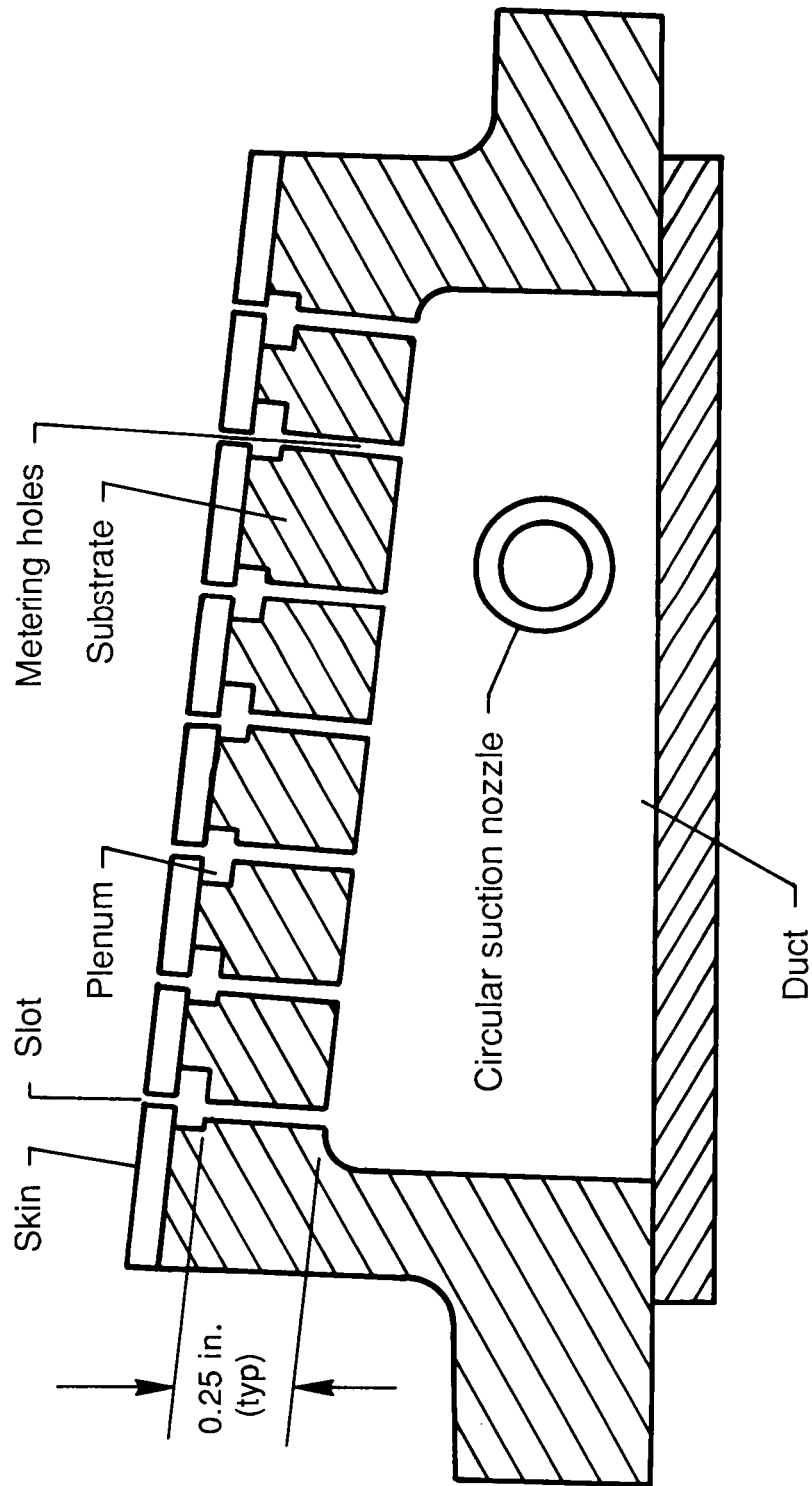
ORIGINAL PAGE IS
OF POOR QUALITY.



L-83-3,976

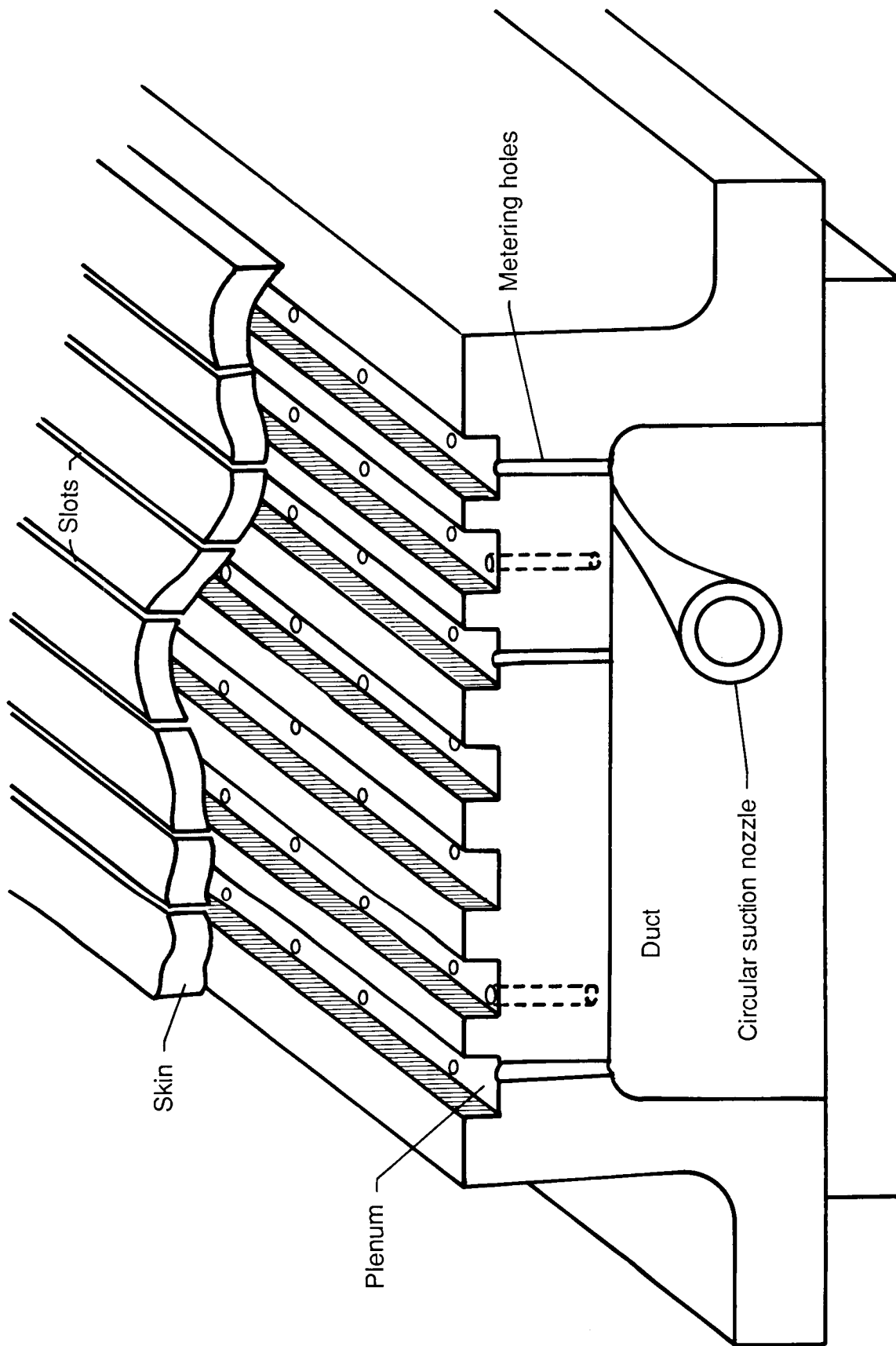
(a) Suction slots in surface.

Figure 7. Model suction system.



(b) Cross-sectional sketch of suction duct.

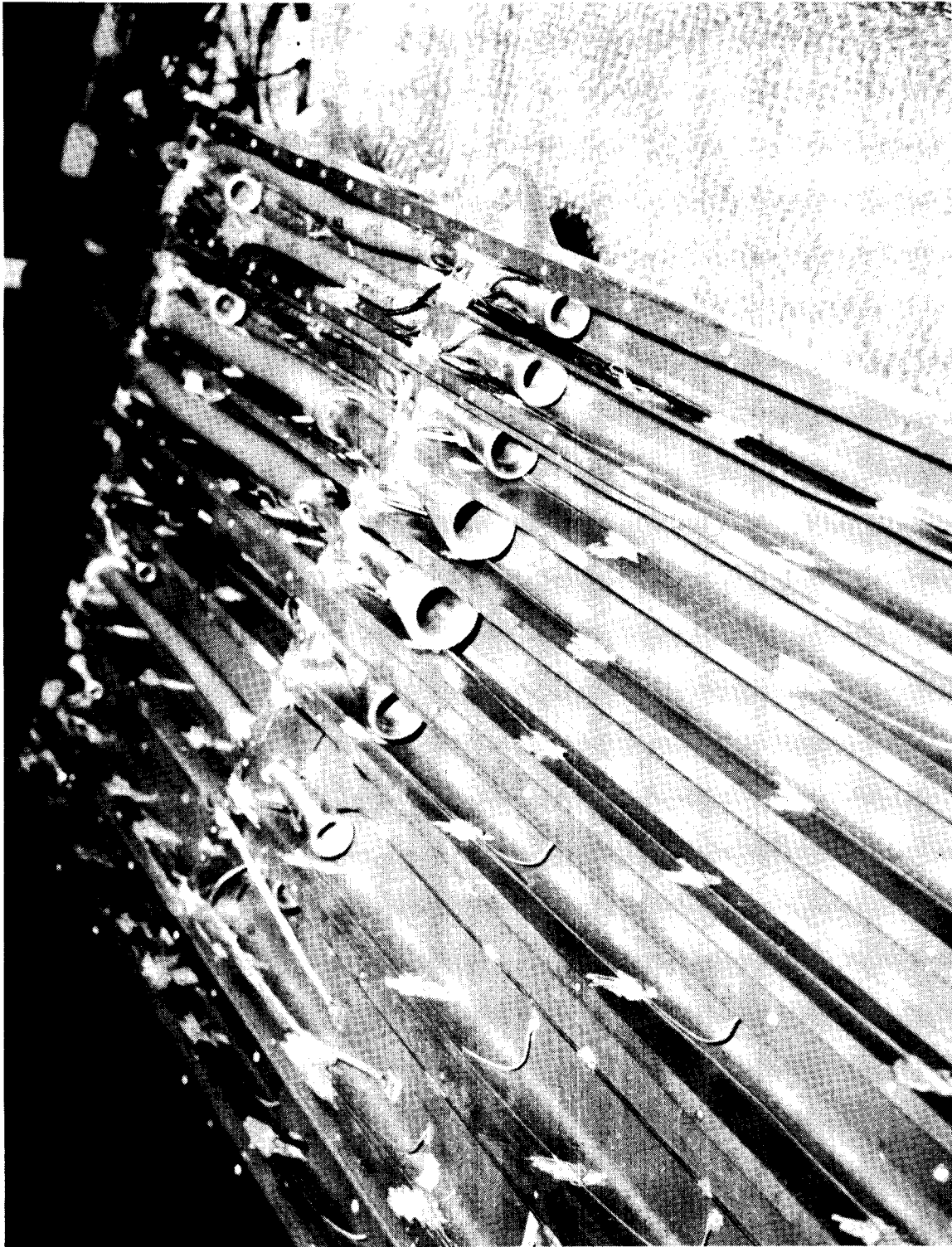
Figure 7. Continued.



(c) Isometric sketch of suction duct.

Figure 7. Continued.

ORIGINAL PAGE IS
OF POOR QUALITY

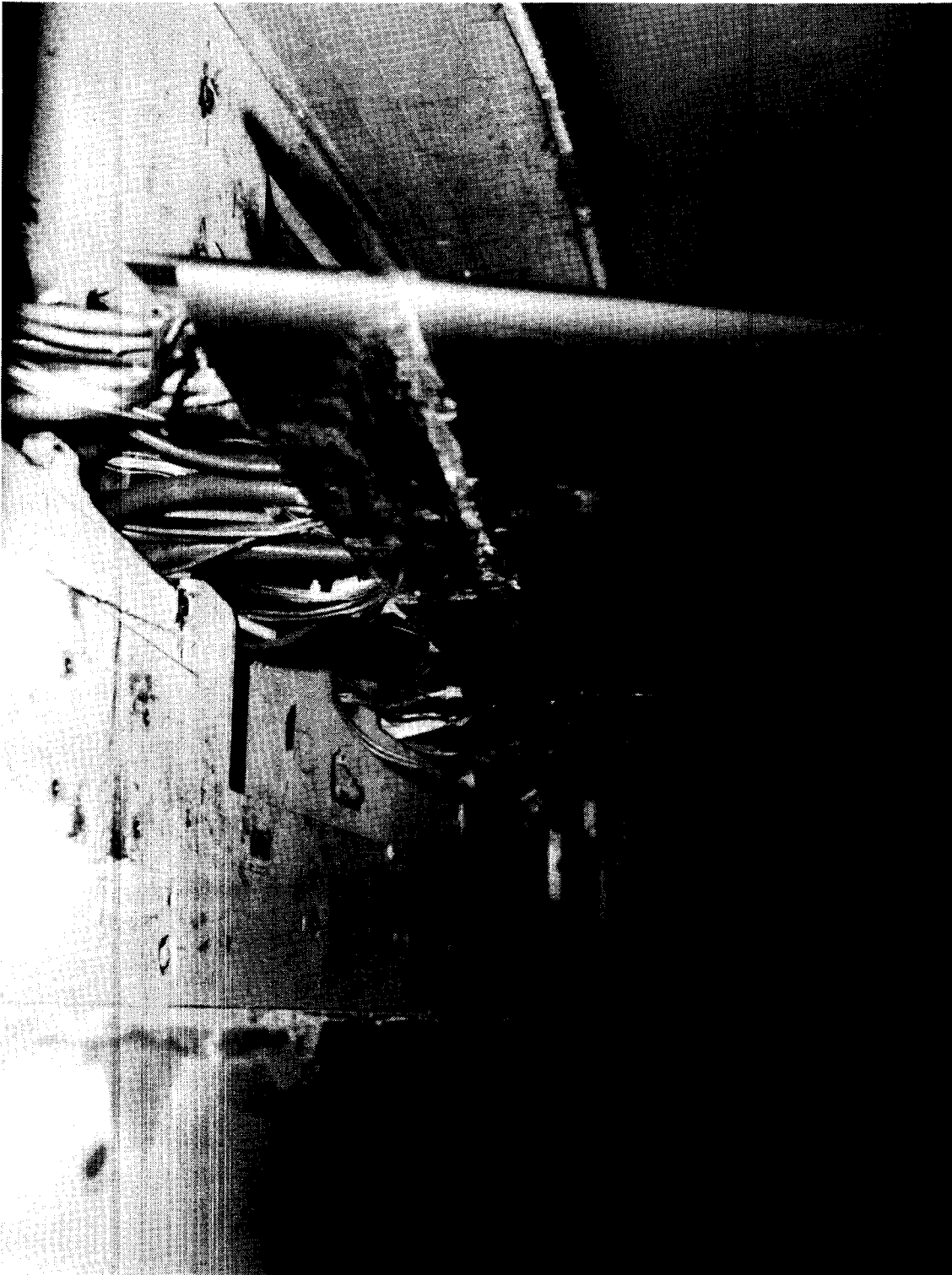


L-81-8757

(d) Photograph of suction nozzles in end of suction ducts.

Figure 7. Continued.

ORIGINAL PAGE IS
OF POOR QUALITY



L-85-1255

(e) Photograph of suction hoses from model exiting through ceiling of test section.

Figure 7. Continued.

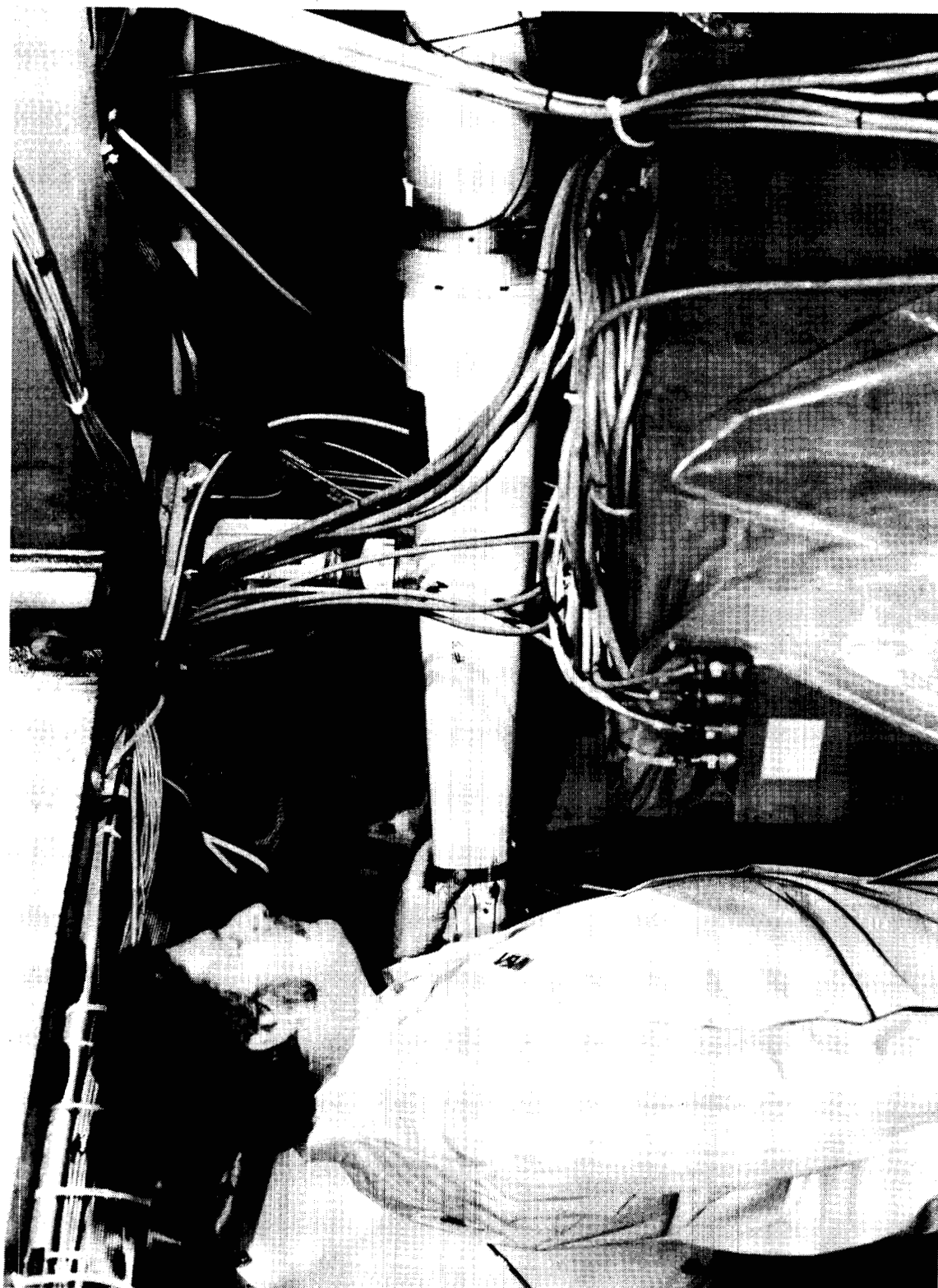


L-82-7,941

(f) Photograph of upstream face of airflow control box.

Figure 7. Continued.

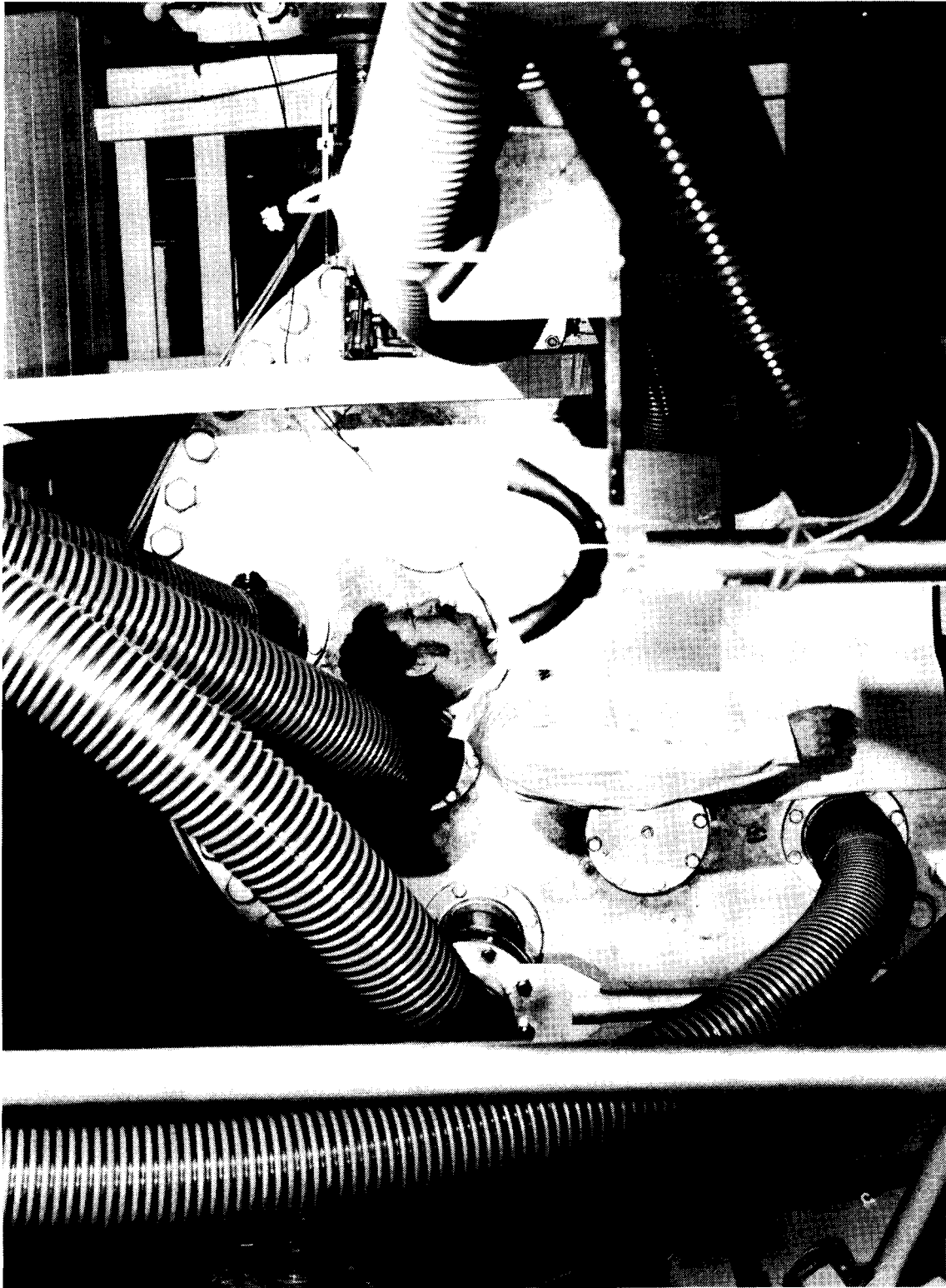
ORIGINAL PAGE IS
OF POOR QUALITY.



L-86-11918

(g) Photograph of variable sonic nozzle downstream of airflow control box.

Figure 7. Continued.



L-86-11915

(h) Photograph of upstream face of collector manifold.

Figure 7. Concluded.

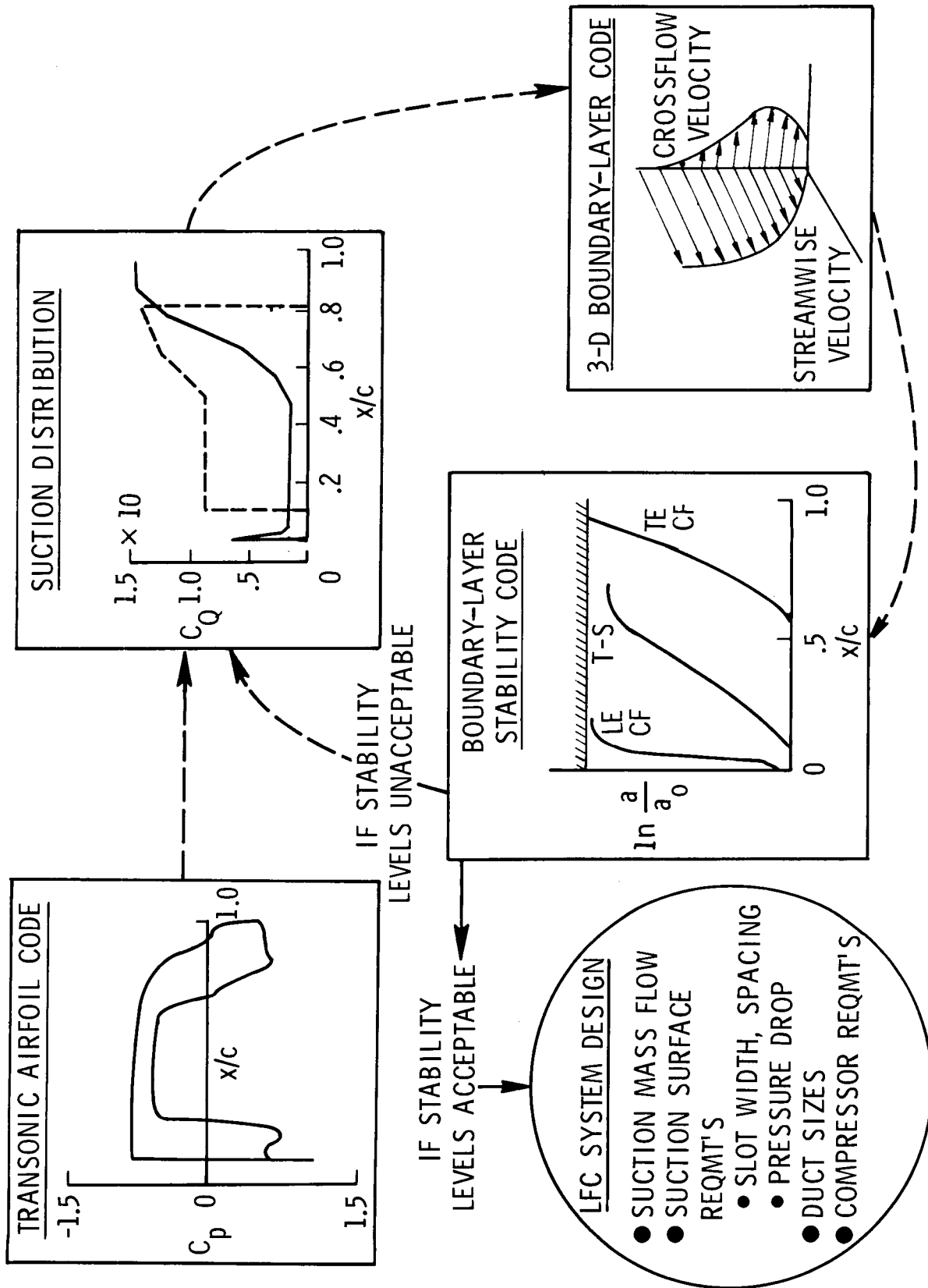


Figure 8. Block diagram of LFC airfoil design cycle.

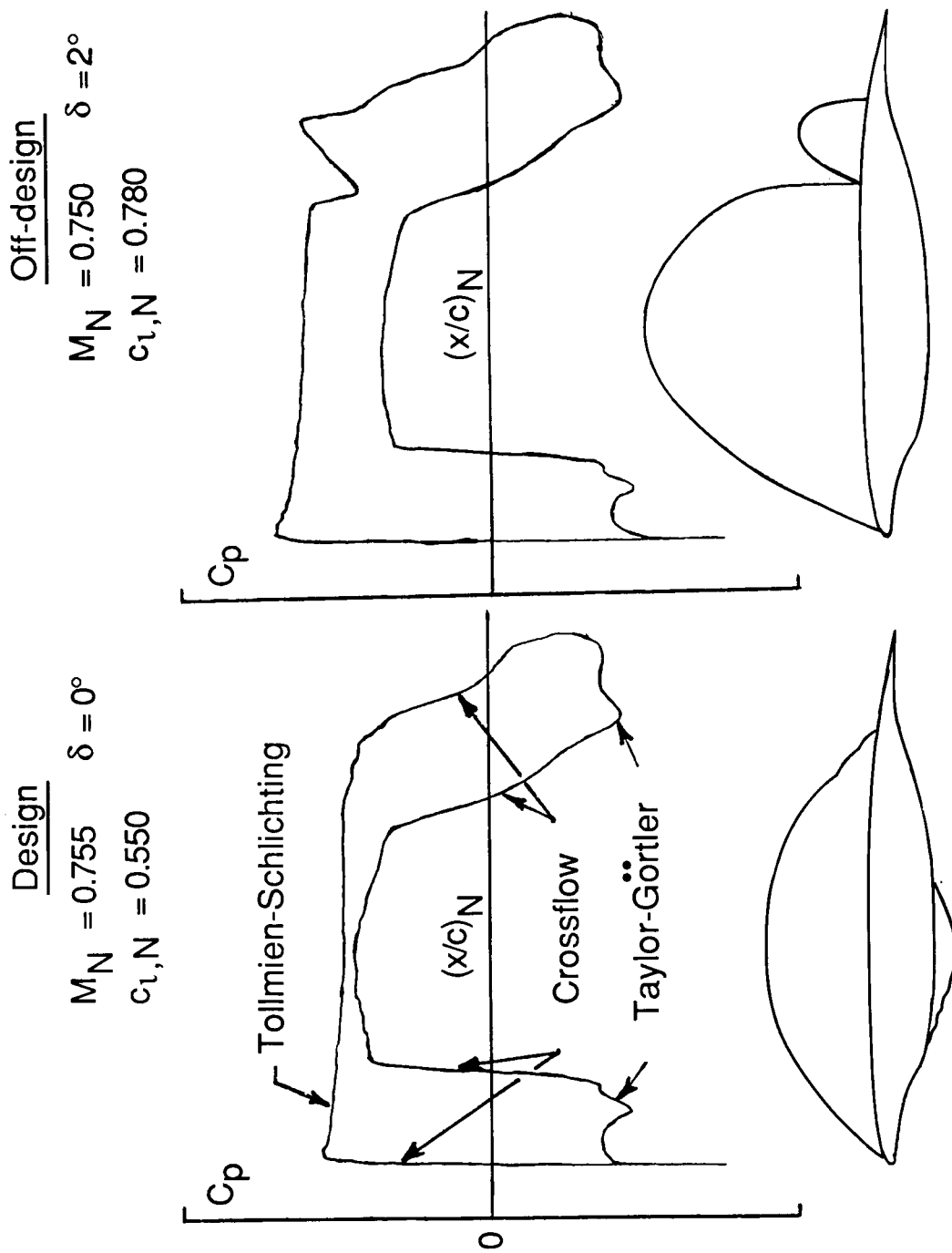


Figure 9. Theoretical pressure distributions and sonic lines for "near-final" shock-free design and high-lift off-design conditions normal to leading edge.

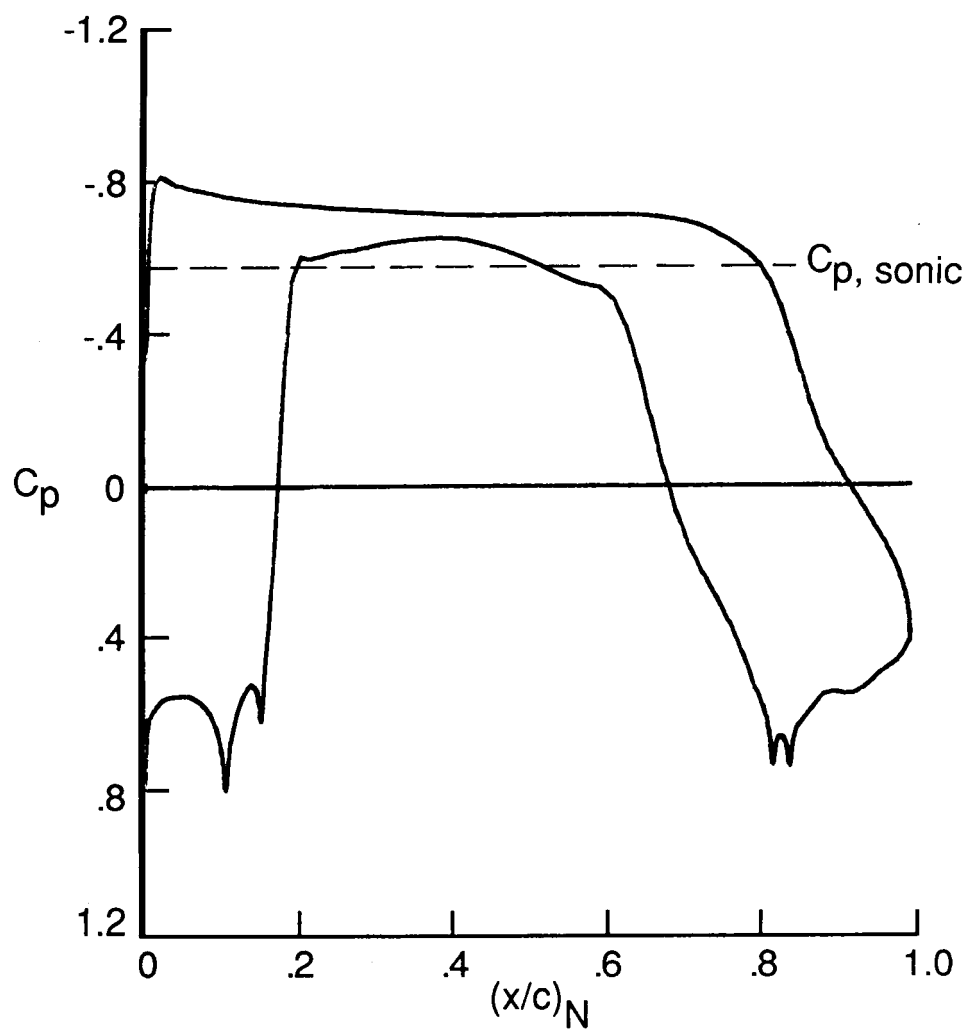
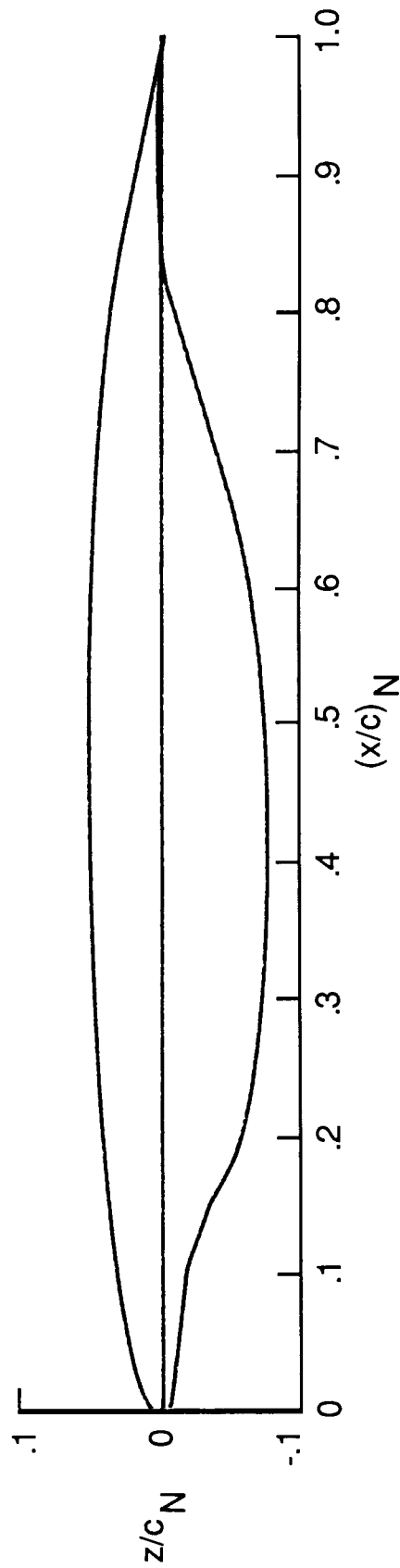
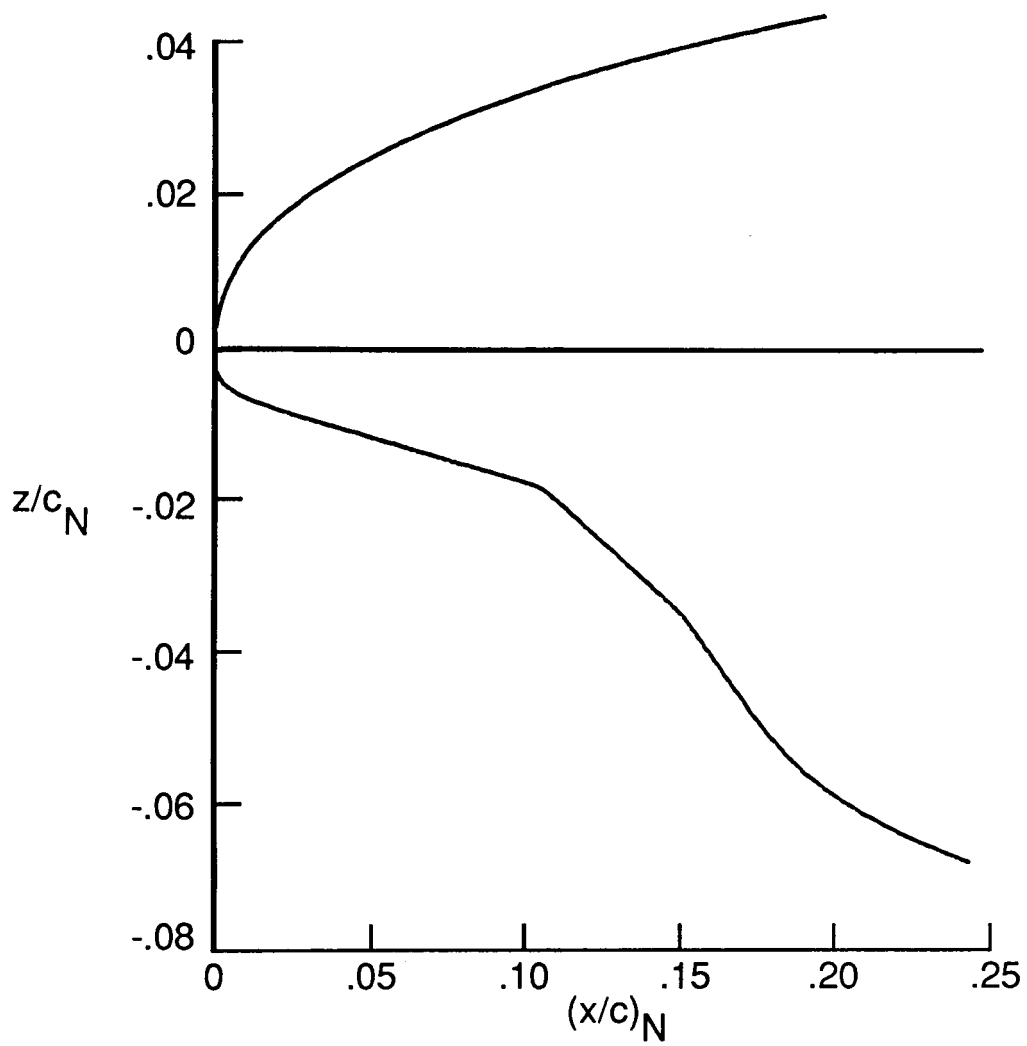


Figure 10. "Final" theoretical pressure distribution normal to leading edge combining Korn-Garabedian and Eppler calculations.



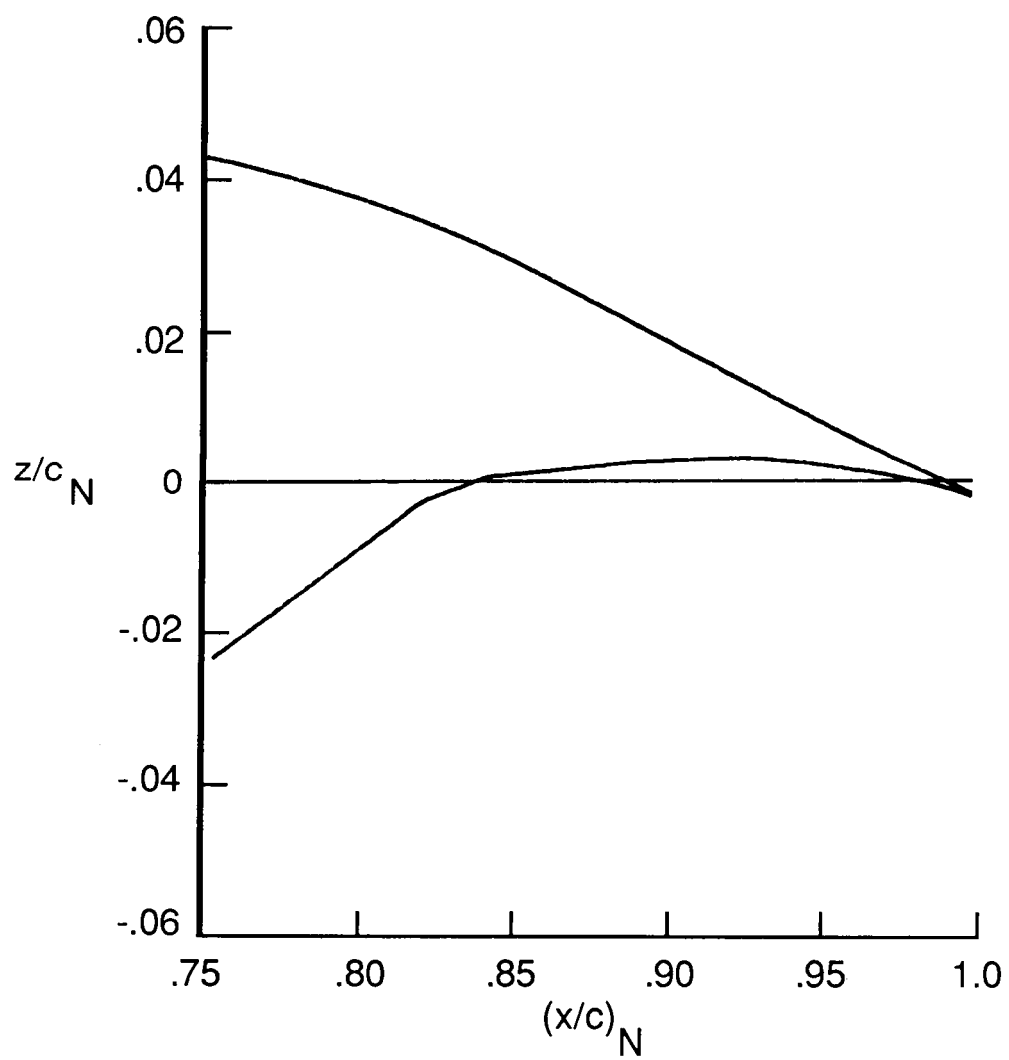
(a) Upper- and lower-surface contours.

Figure 11. Sketches of LFC airfoil normal to leading edge.



(b) Forward lower surface.

Figure 11. Continued.



(c) Aft lower surface.

Figure 11. Concluded.

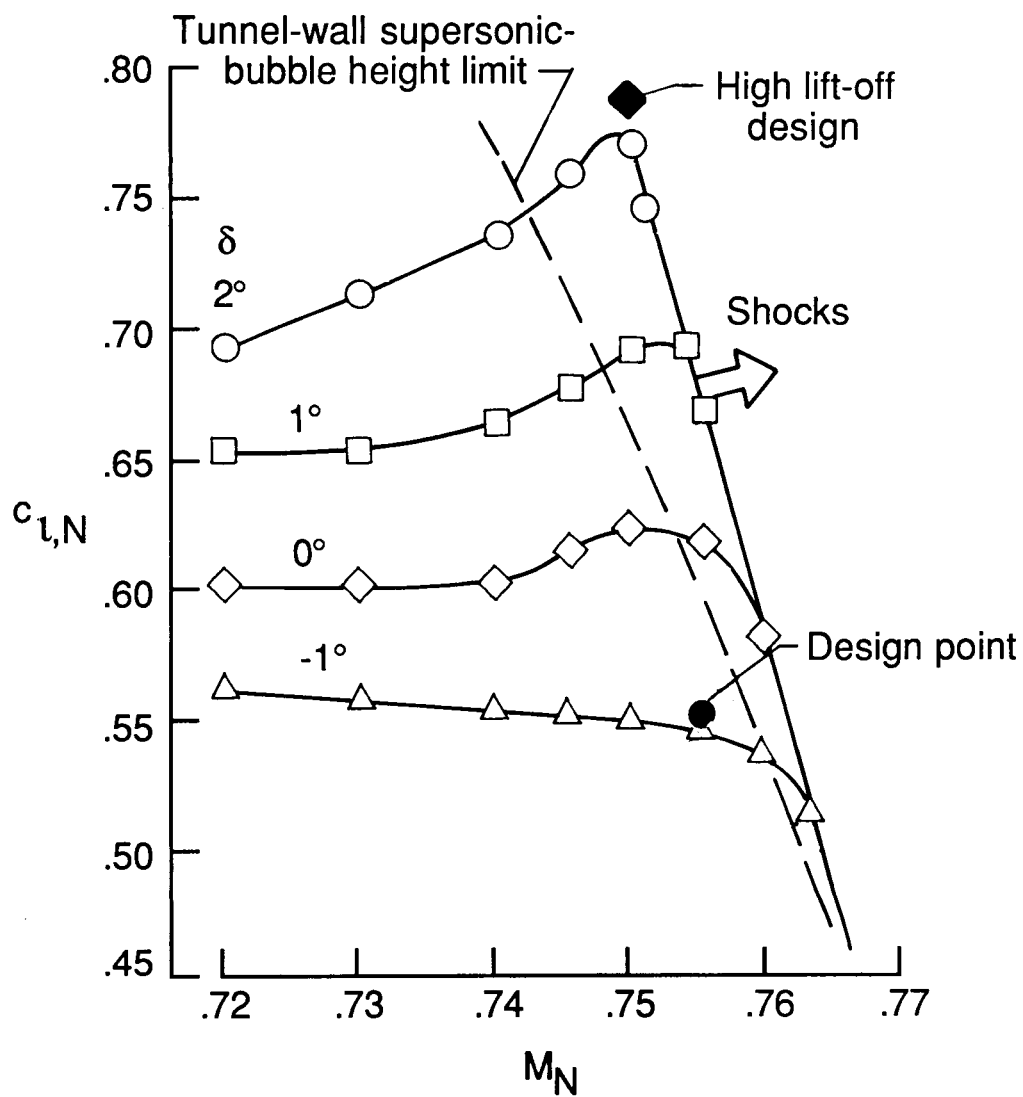
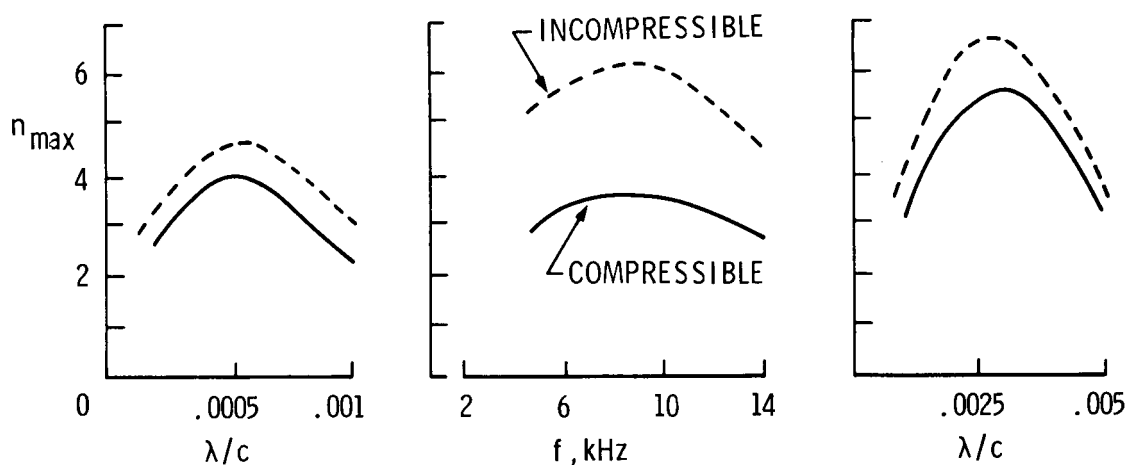


Figure 12. Variation of theoretical shock-free limits with Mach number. $M_N = M_\infty \cos \Lambda$.



NOSE REGION

- CROSSFLOW INSTABILITY
- STATIONARY DISTURB. ($f = 0$)
- $0 \leq \sqrt{R_x} \leq 1600$
- 15% DECREASE IN n_{\max}

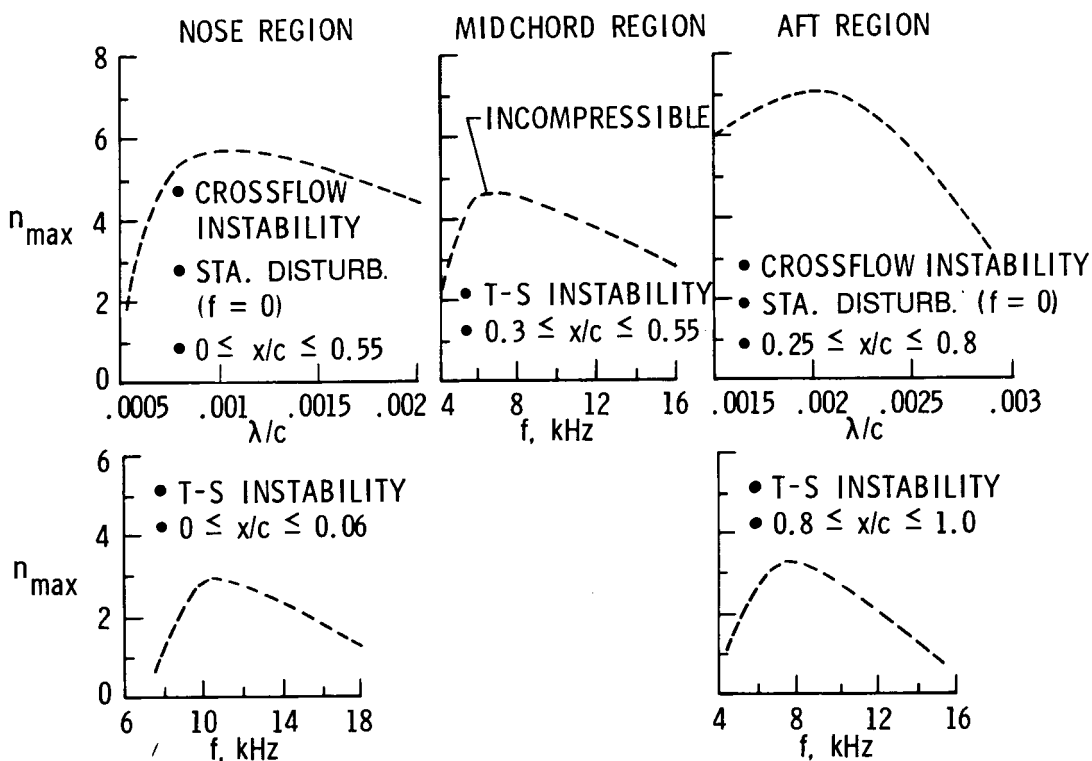
MIDCHORD REGION

- T-S INSTABILITY
- $0 \leq \sqrt{R_x} \leq 3300$
- 40% DECREASE IN n_{\max}

AFT REGION

- CROSSFLOW INSTABILITY
- STATIONARY DISTURB. ($f = 0$)
- $\sqrt{R_x} \geq 3900$
- 15% DECREASE IN n_{\max}

(a) Upper surface.



(b) Lower surface.

Figure 13. Calculated maximum-disturbance amplitude ratios ($n = \ln a/a_0$) for design conditions.

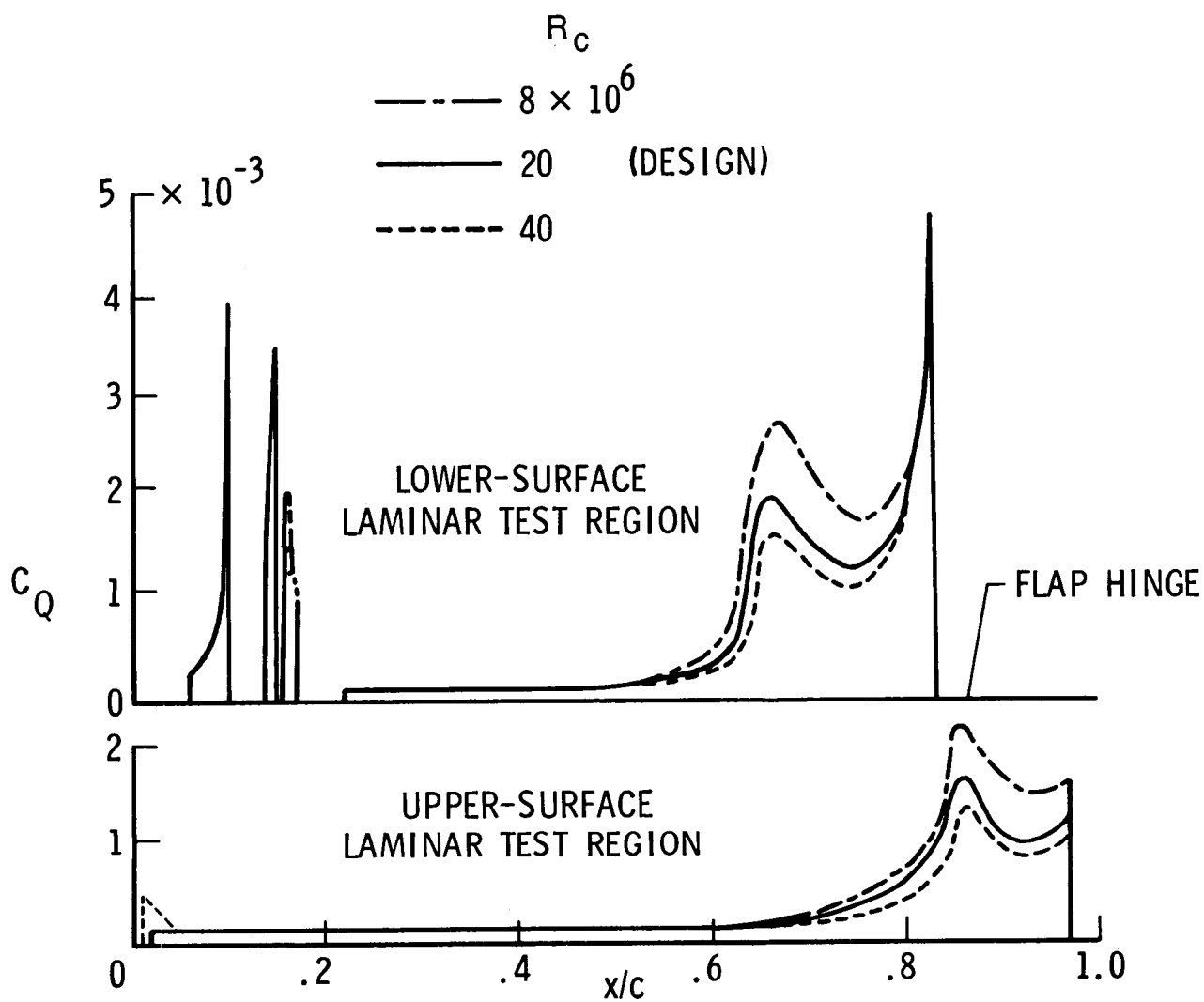


Figure 14. Theoretical suction distributions for LFC airfoil with continuous area suction. $C_Q = \rho_w w_w / \rho_\infty U_\infty$.

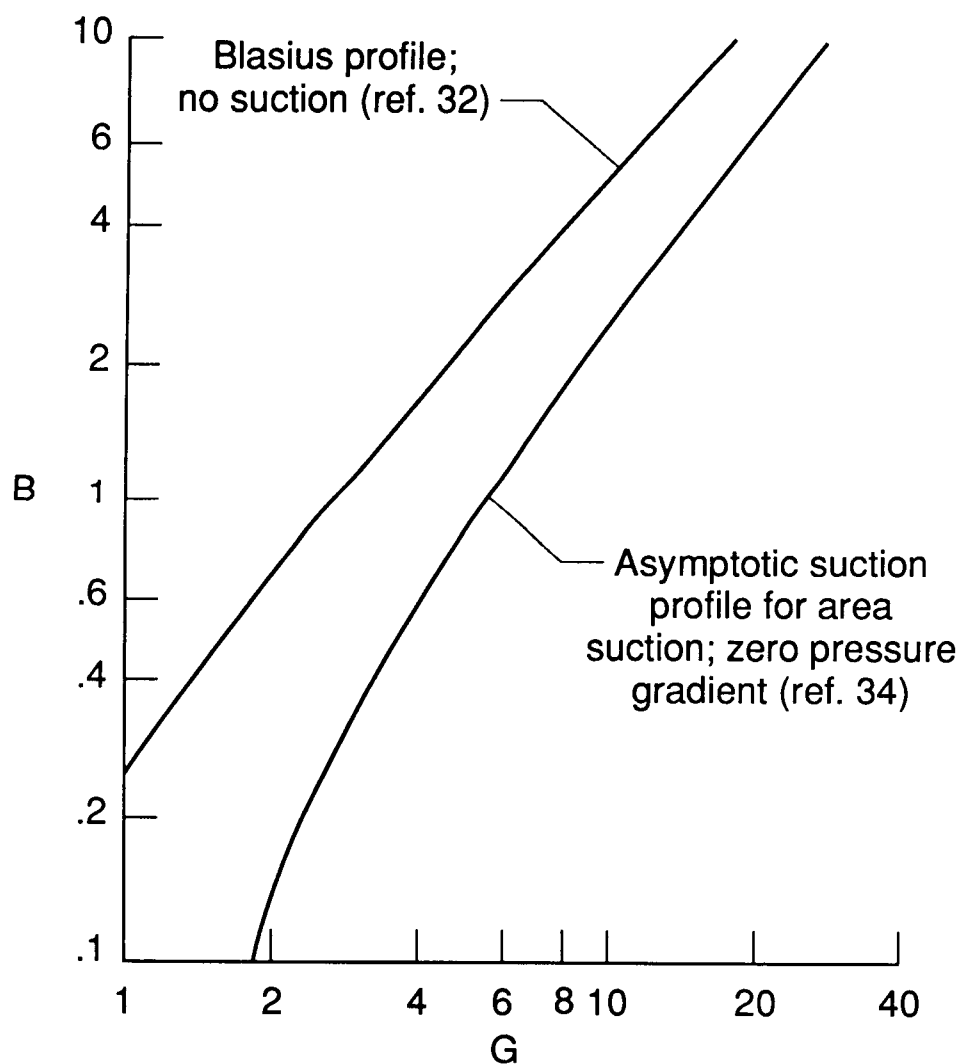


Figure 15. Linearized maximum growth factor B of Taylor-Görtler vortices versus Görtler parameter G for incompressible flow with and without suction. $B = (\beta \theta R_\theta)_{\max}$; $G = R_\theta (\theta/r)^{1/2}$.

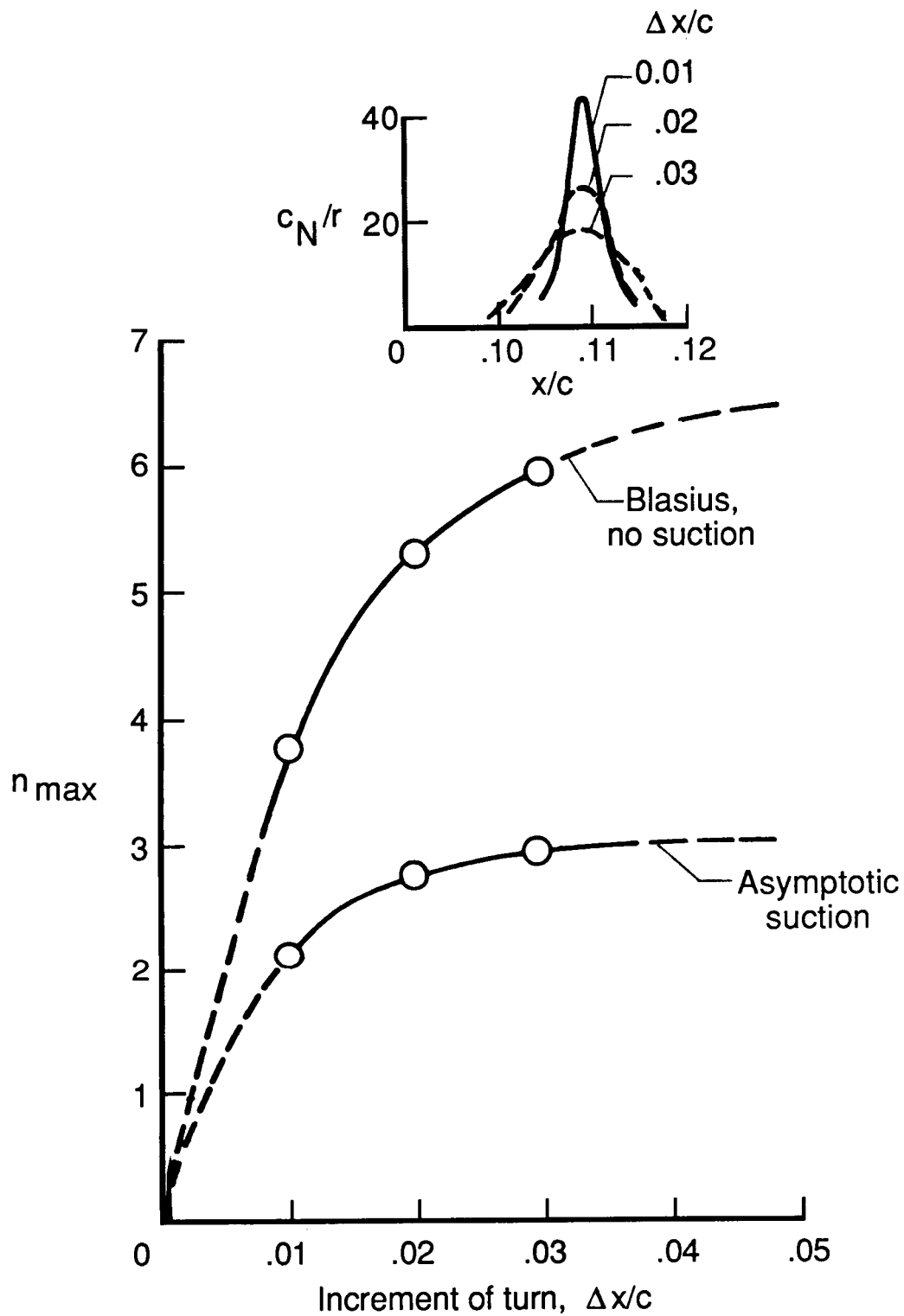


Figure 16. Representative values of theoretical maximum-disturbance amplitude ratio for Taylor-Görtler vortices with small incremental turn of flow.

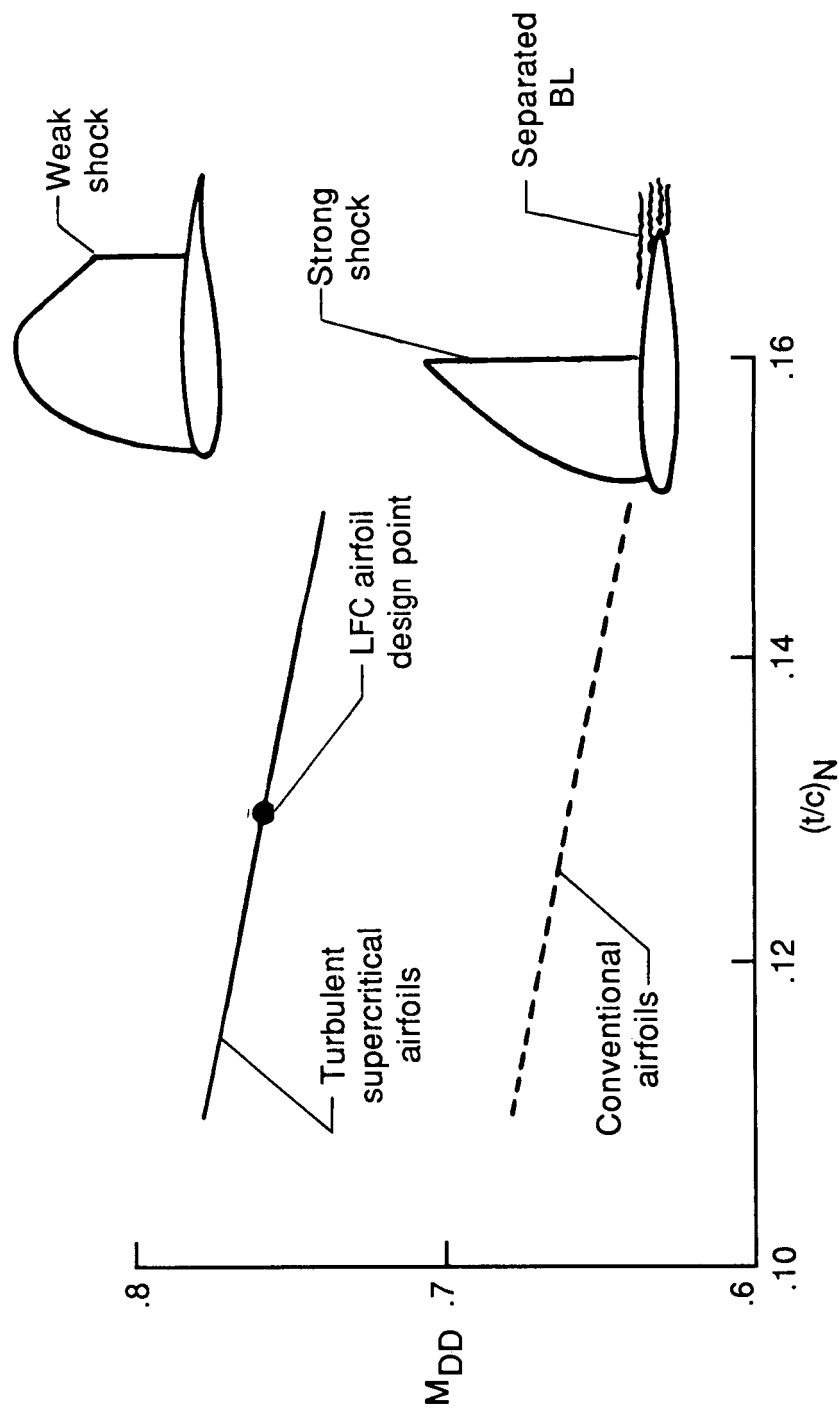
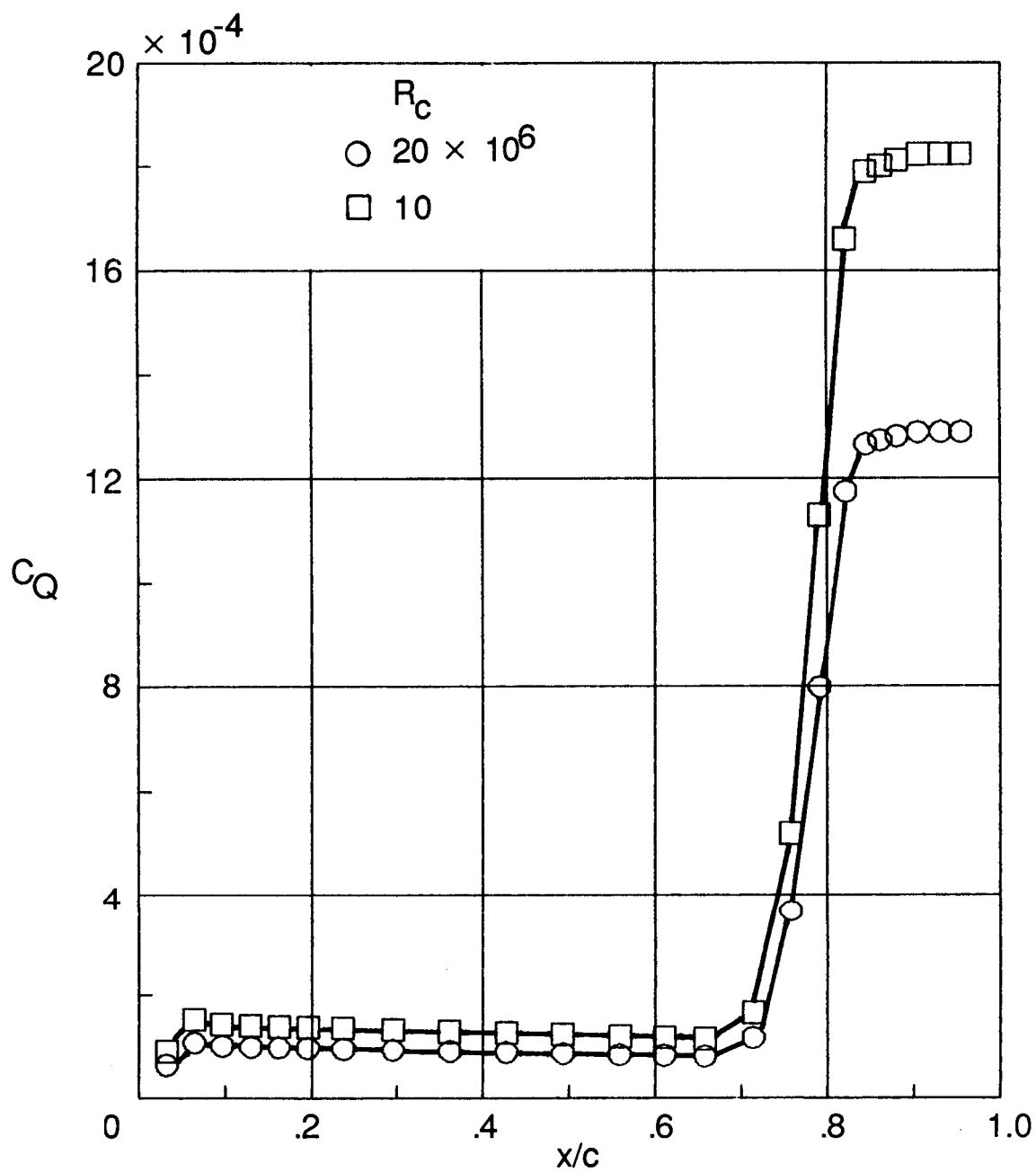
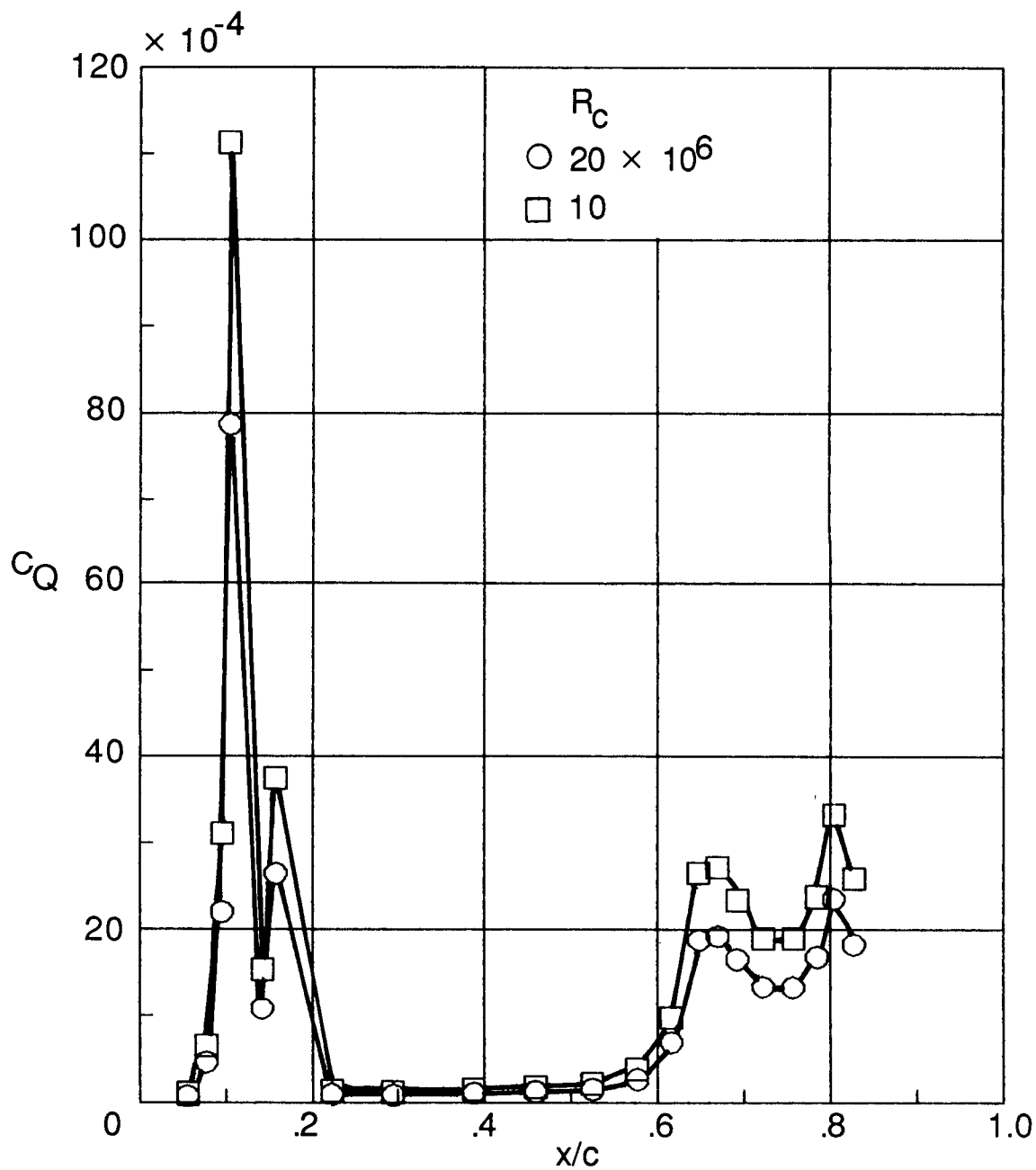


Figure 17. Comparison of drag-divergence Mach number for present LFC airfoil with turbulent supercritical and conventional airfoils. $c_{l,N} = 0.55$.



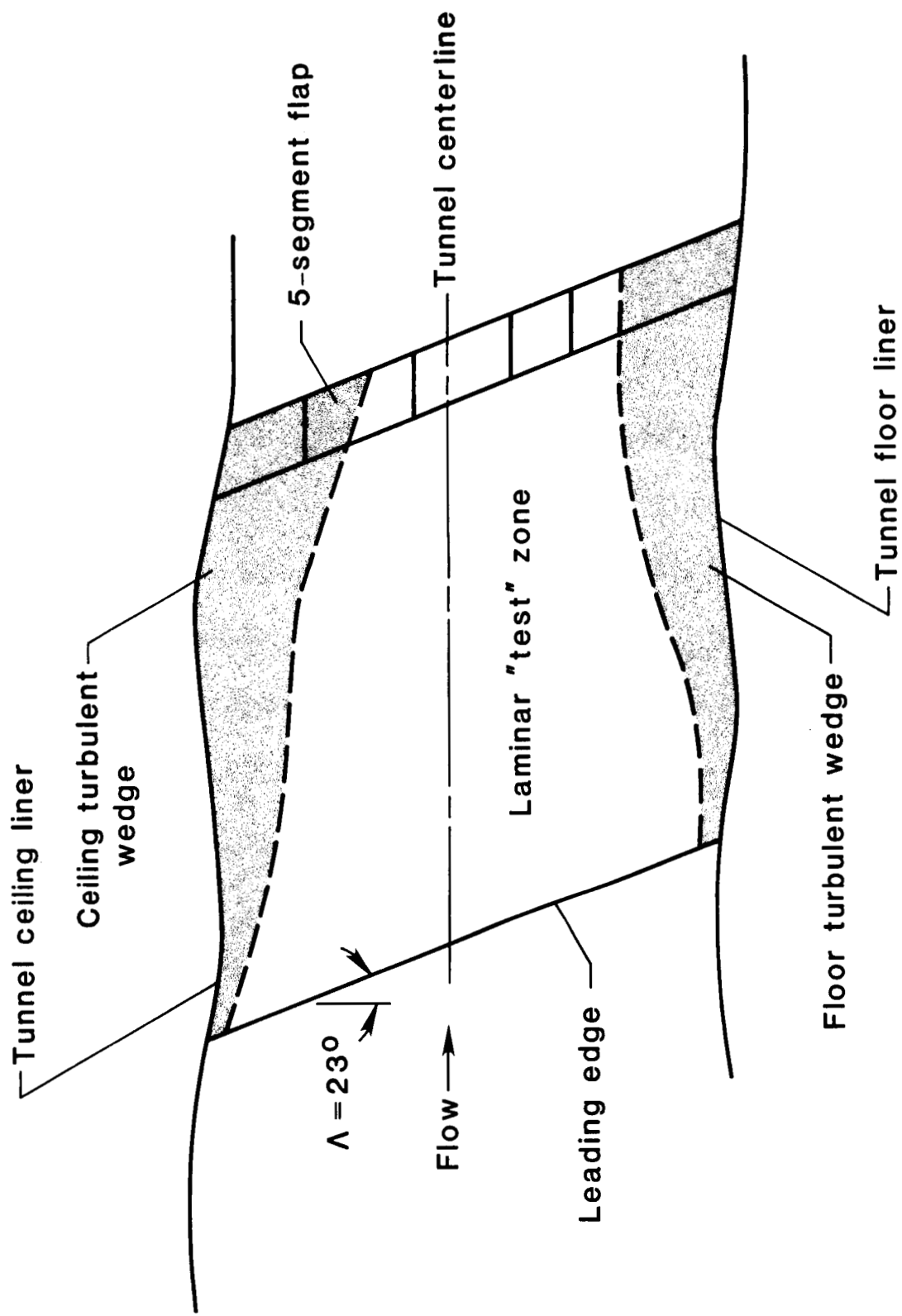
(a) Upper surface.

Figure 18. Theoretical suction requirements for slotted LFC airfoil for $R_c = 10 \times 10^6$ and 20×10^6 .



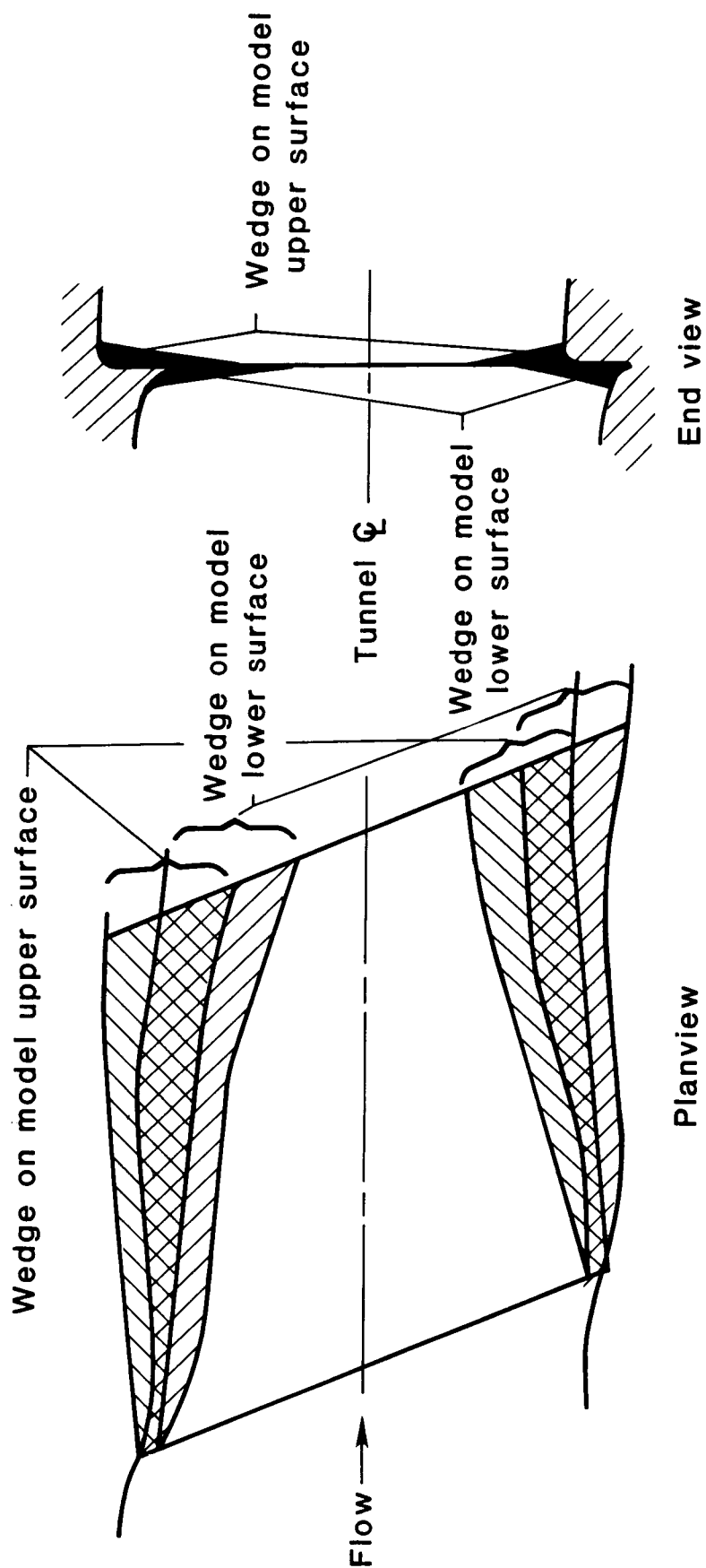
(b) Lower surface.

Figure 18. Concluded.



(a) Laminar "test" zone.

Figure 19. Planform view of model from lower surface in tunnel.



(b) Turbulent wedges in model/liner junctures.

Figure 19. Concluded.

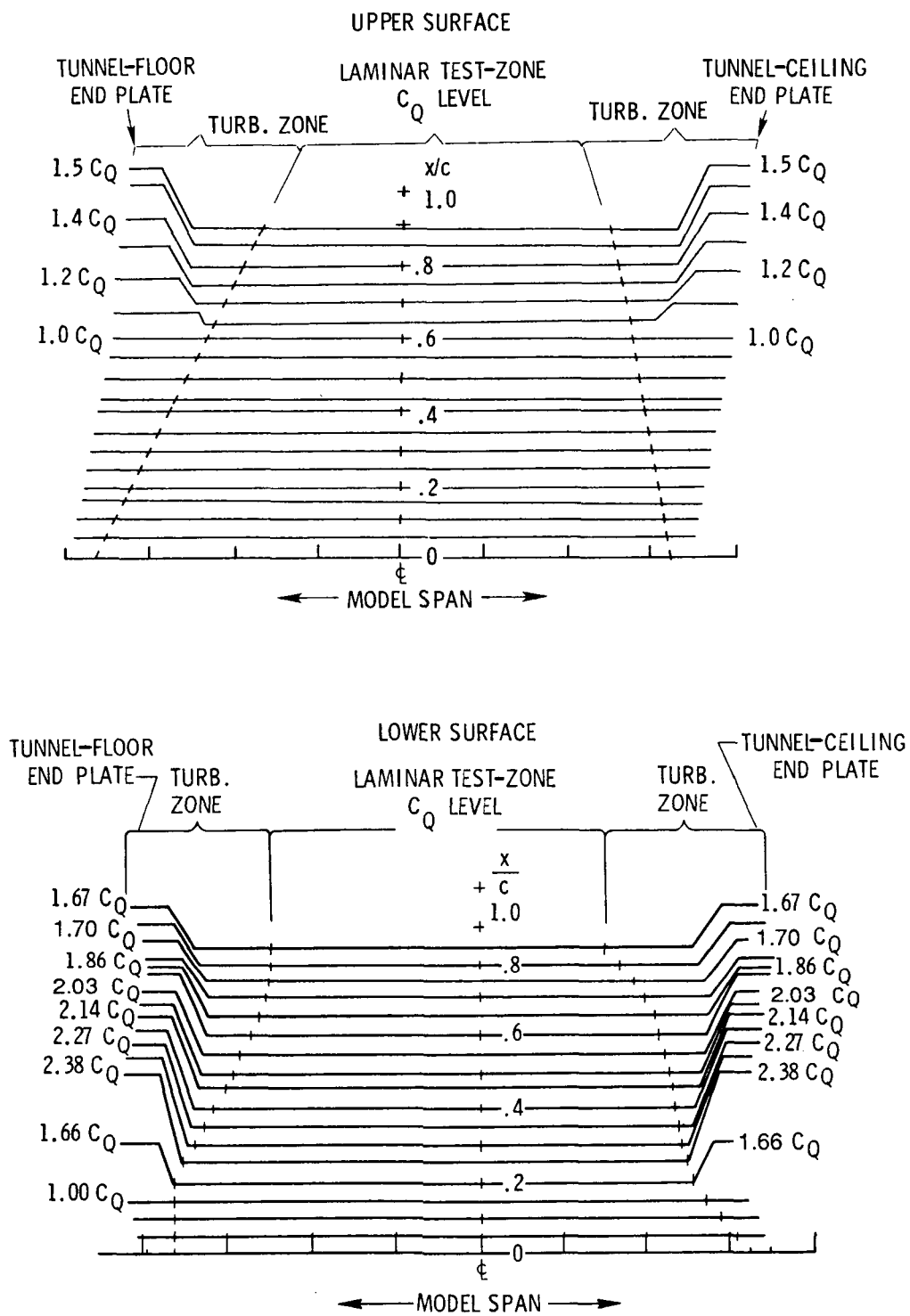


Figure 20. Spanwise variation of design suction distribution of slotted LFC airfoil.

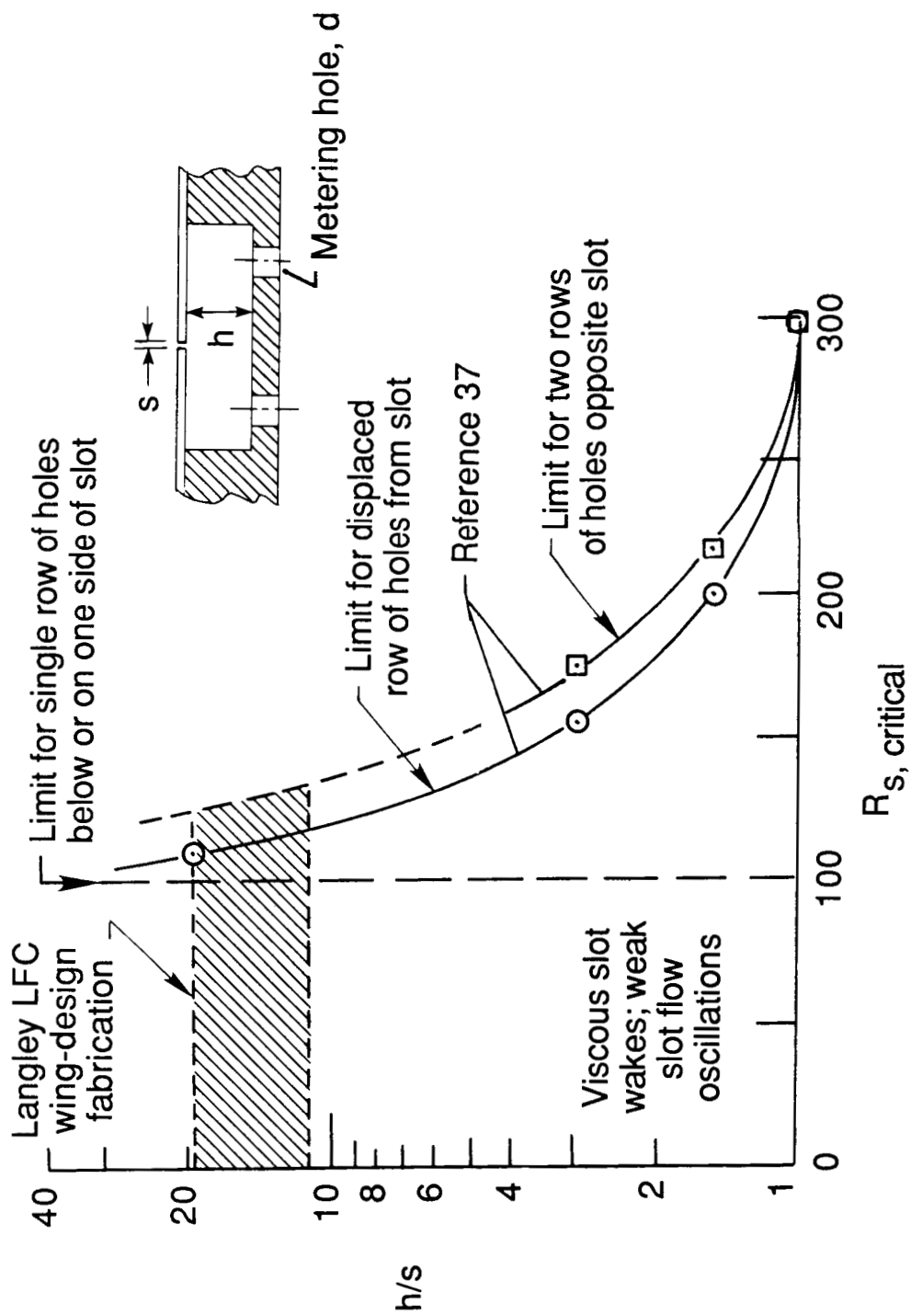


Figure 21. Experimental limits for variations of suction plenum ratio of height to slot width with slot Reynolds number for several limiting metering-hole geometries.

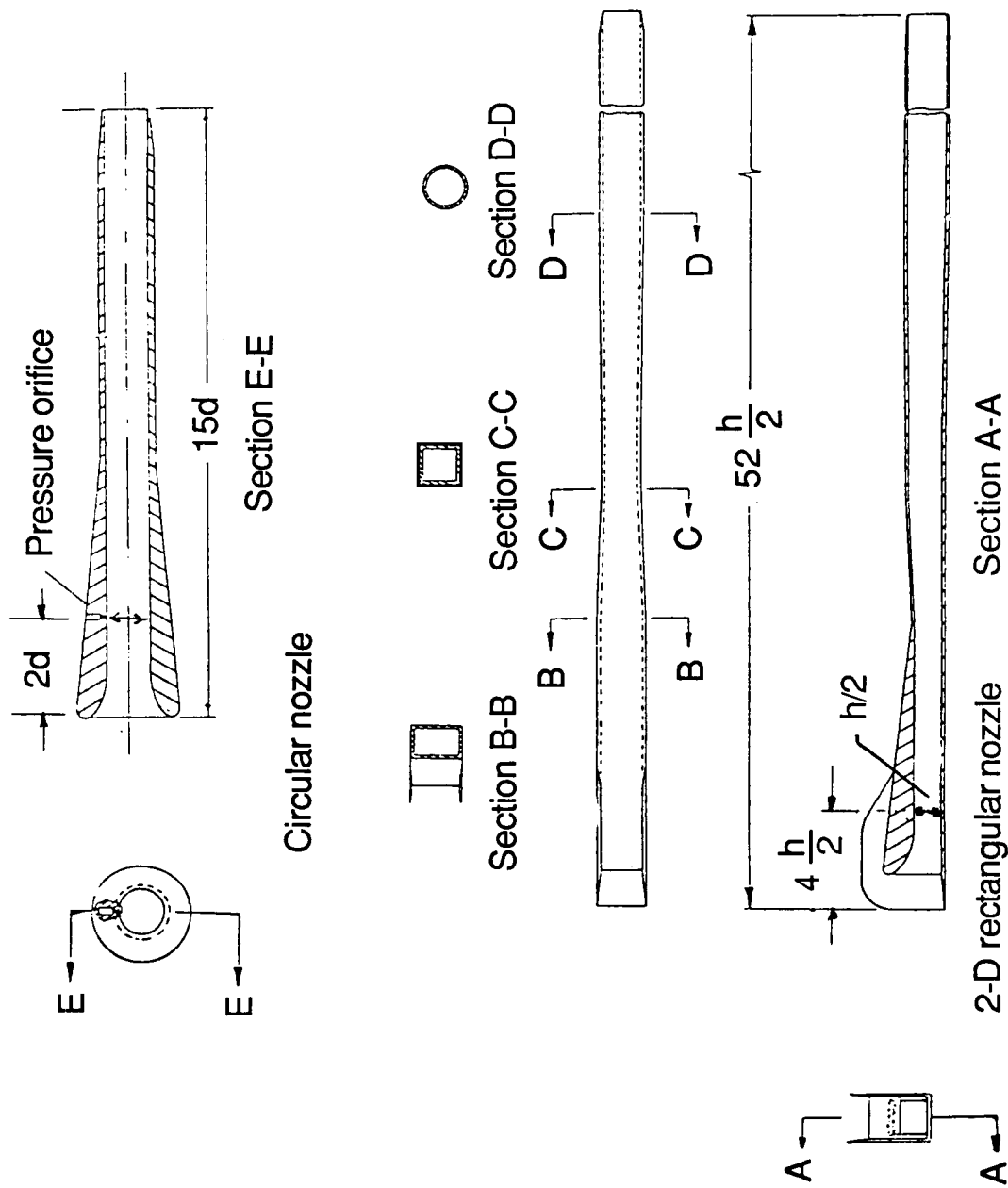
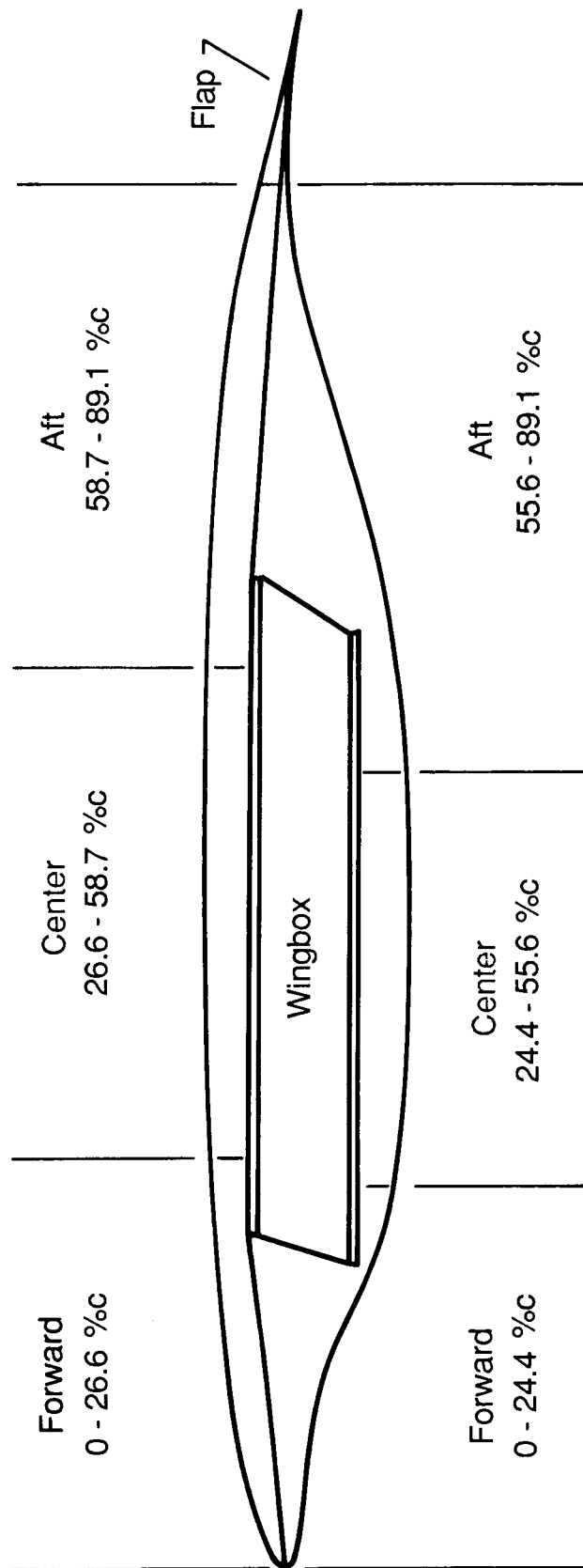


Figure 22. Sketches of suction duct nozzles.

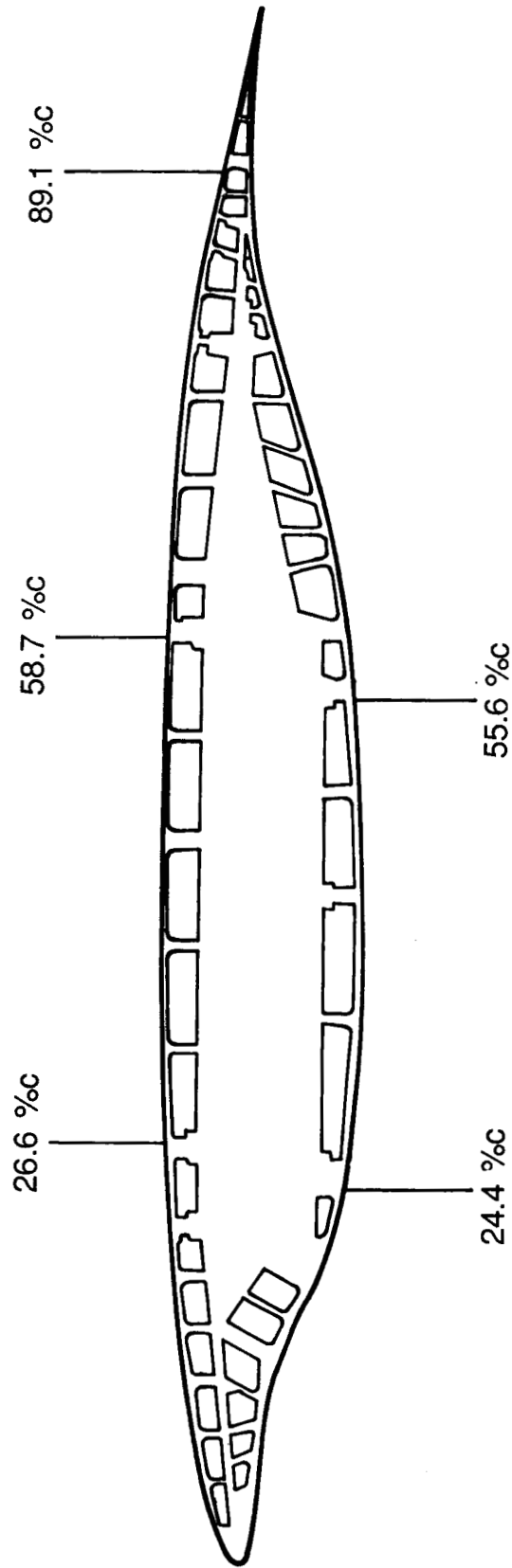
UPPER PANELS



LOWER PANELS

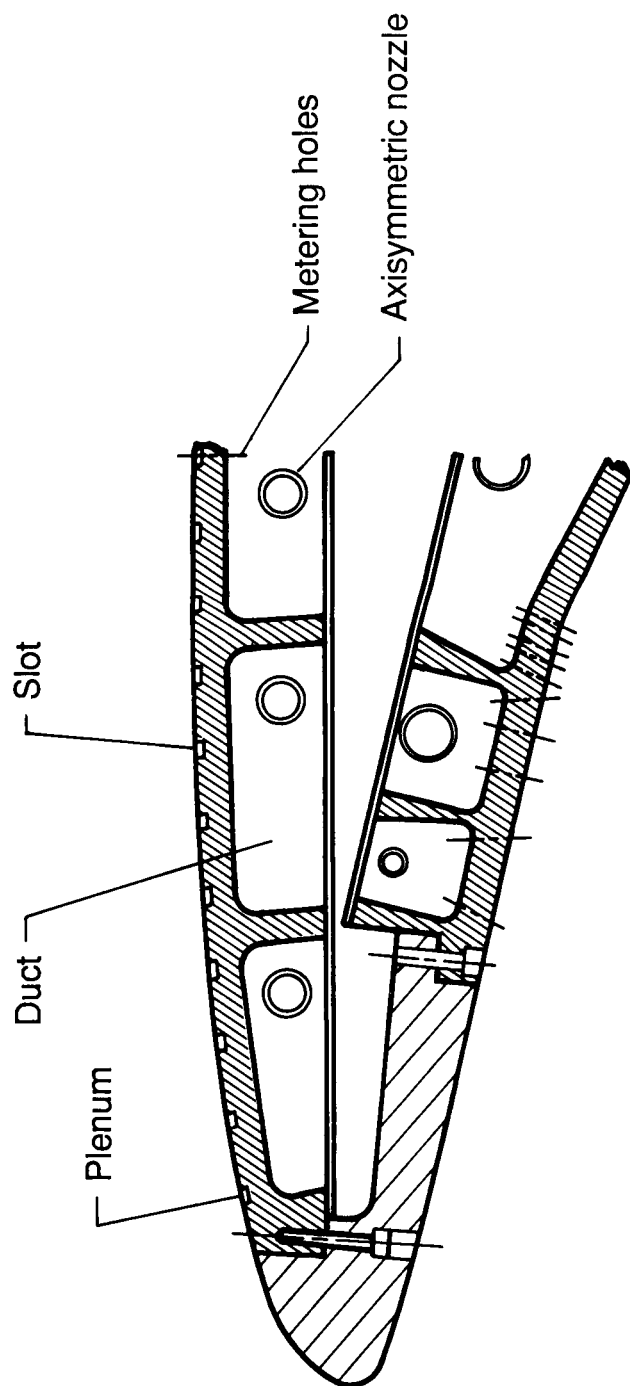
(a) Panel arrangement.

Figure 23. Cross section of LFC model normal to leading edge.

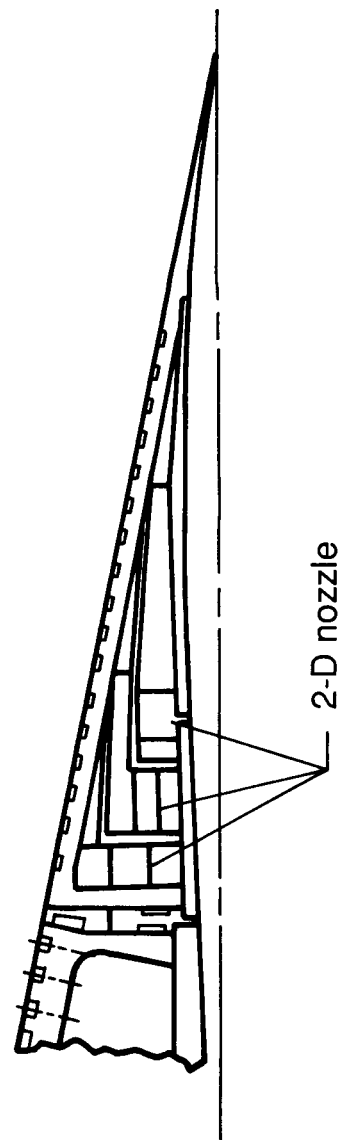


(b) Duct arrangement.

Figure 23. Concluded.

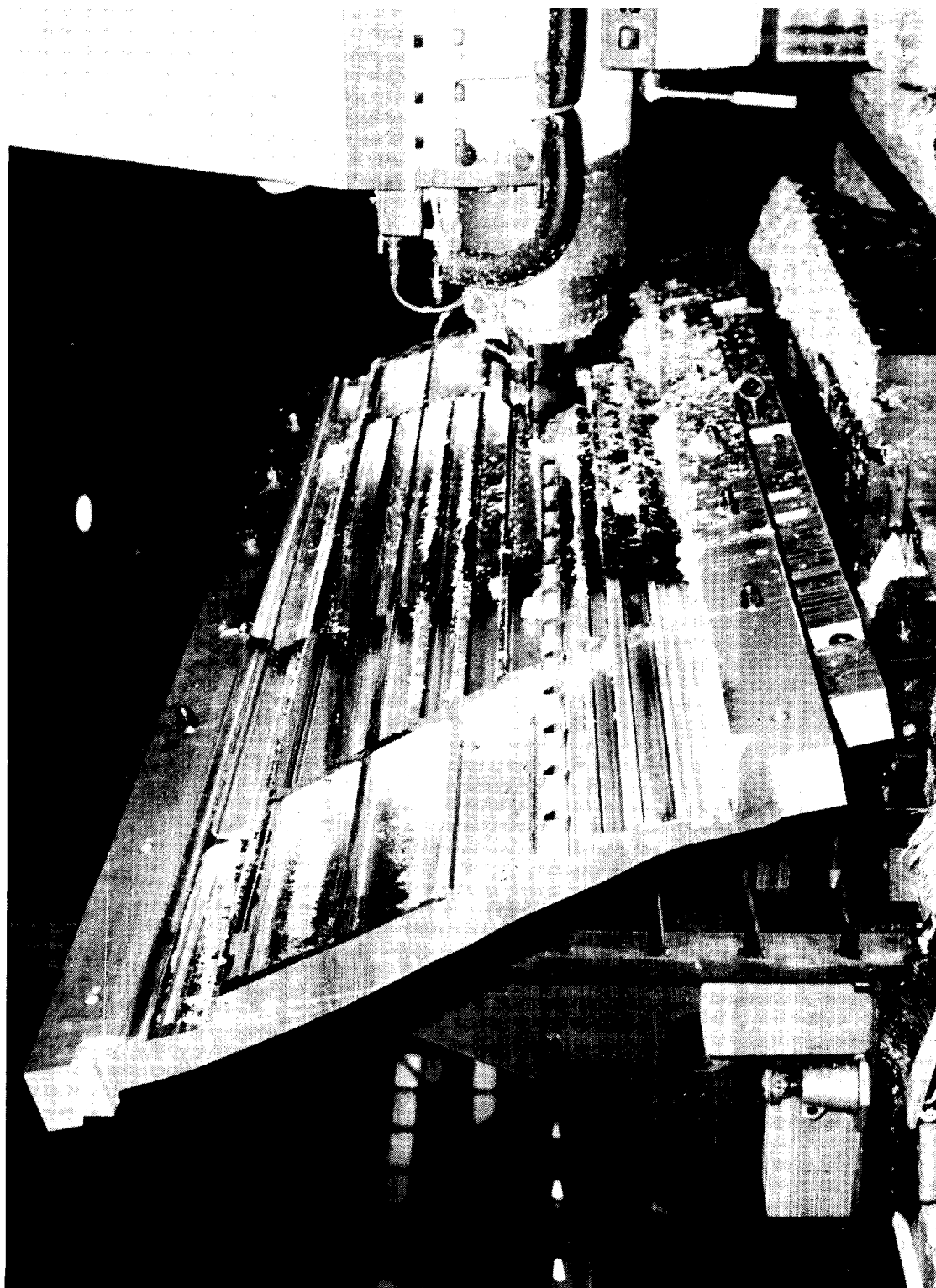


(a) Airfoil leading-edge region.



(b) Airfoil flap region.

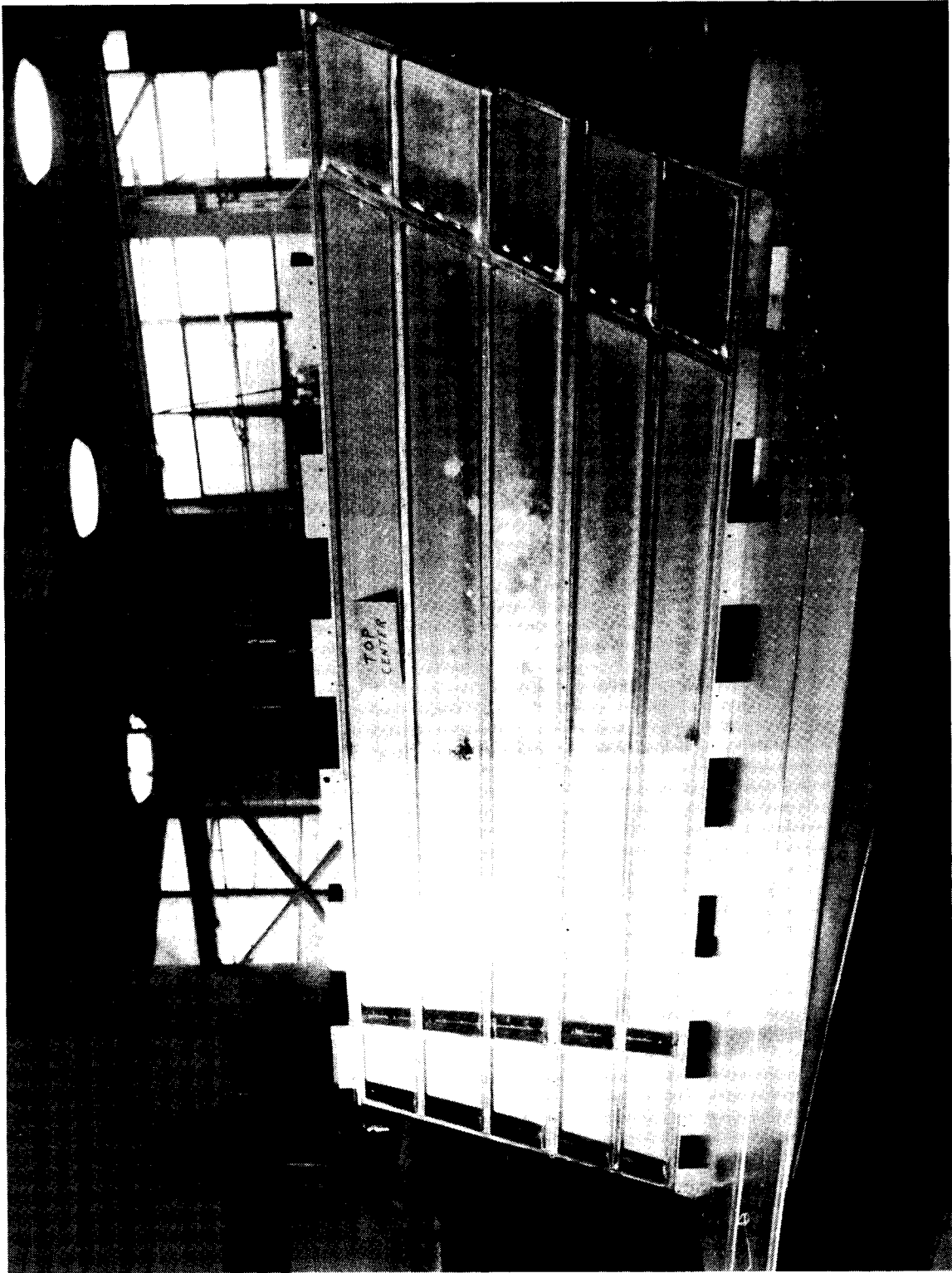
Figure 24. Sketches showing features of surface and internal suction system of model nose and flap regions.



L-81-1316

(a) Aft lower-surface panel during milling process.

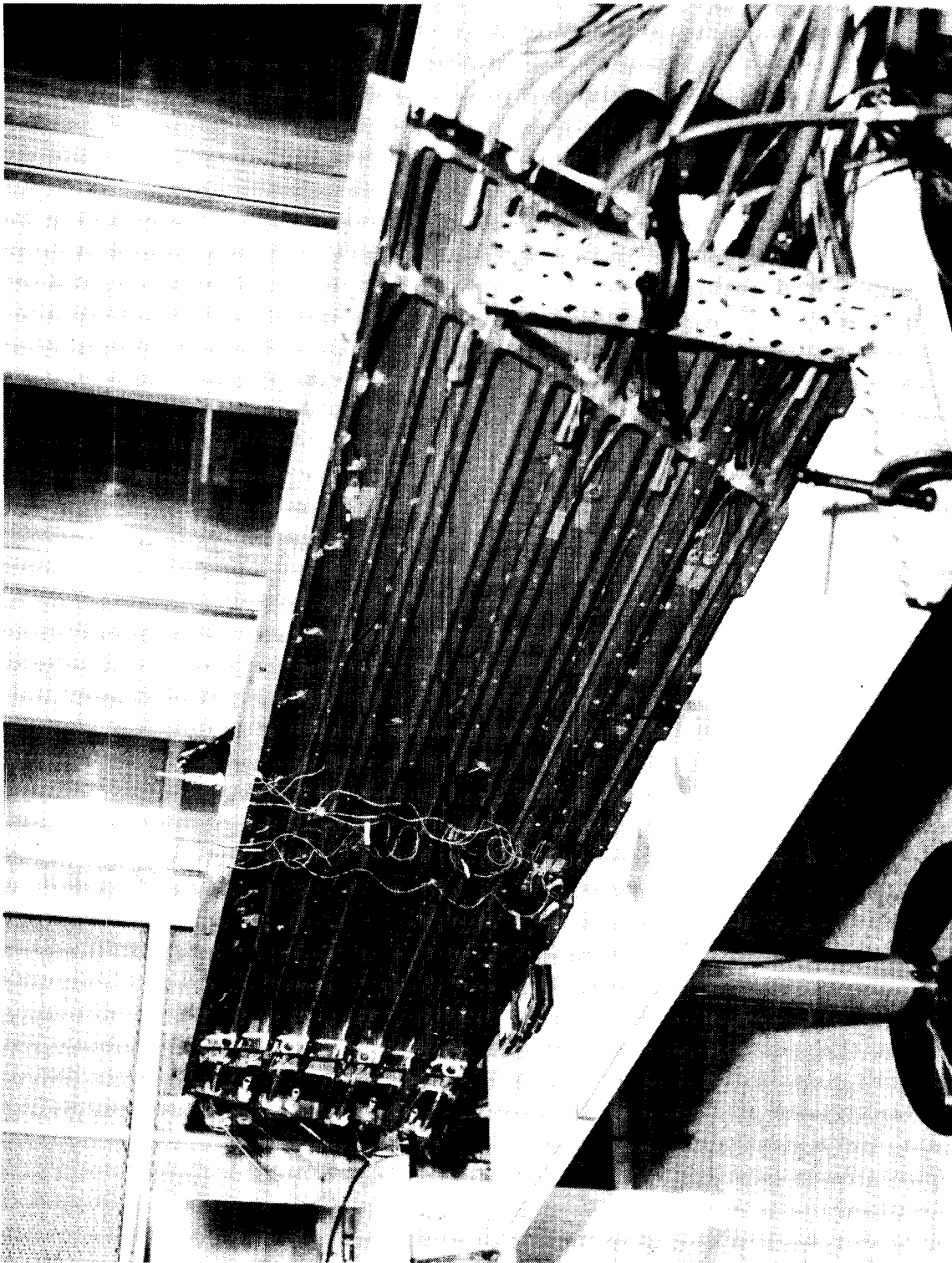
Figure 25. Photographs of model panels in various stages of fabrication.



L-79-5436

(b) Center upper-surface panel after milling process.

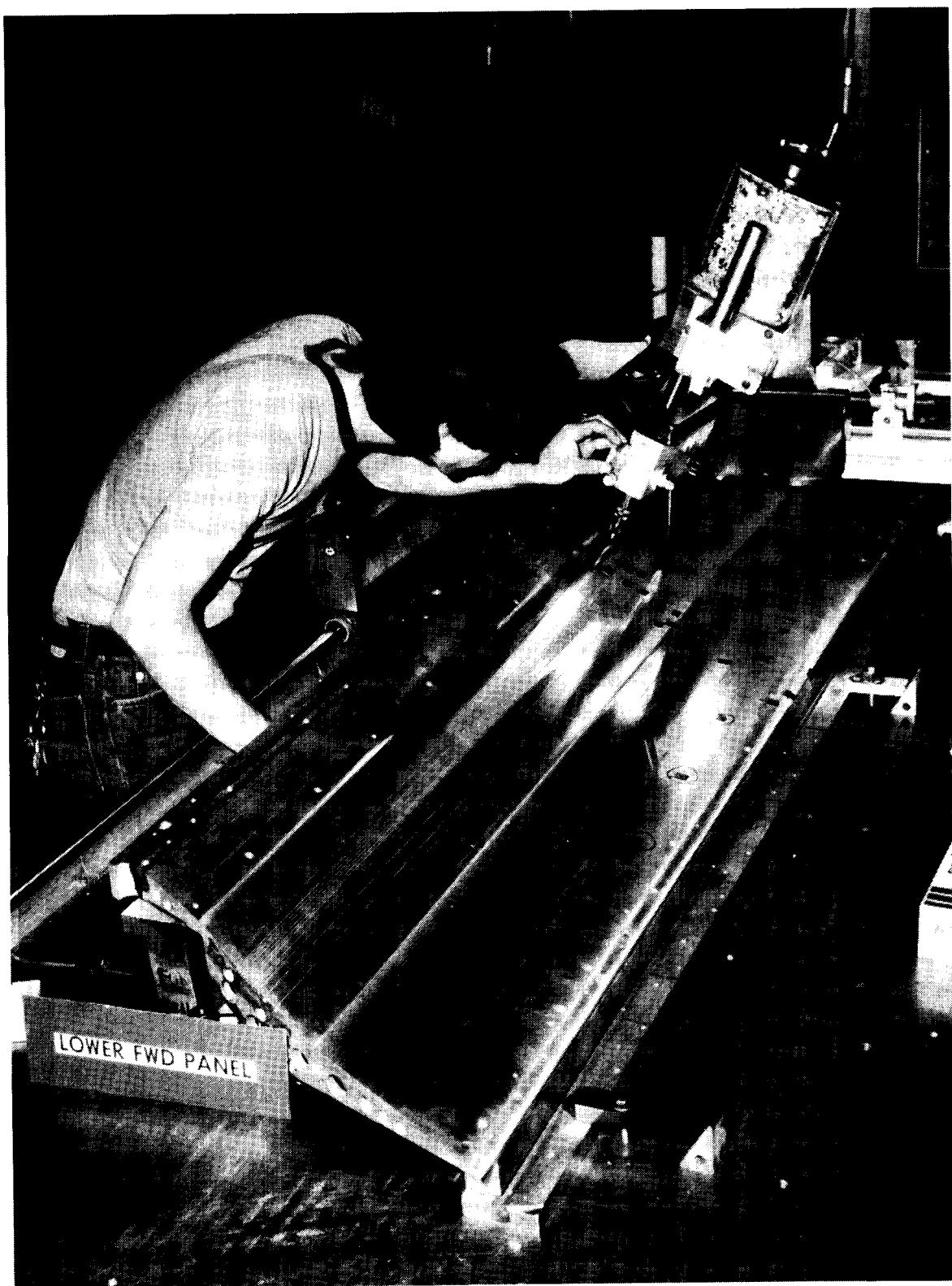
Figure 25. Continued.



L-81-8960

(c) Forward upper-surface panel during installation of suction nozzles.

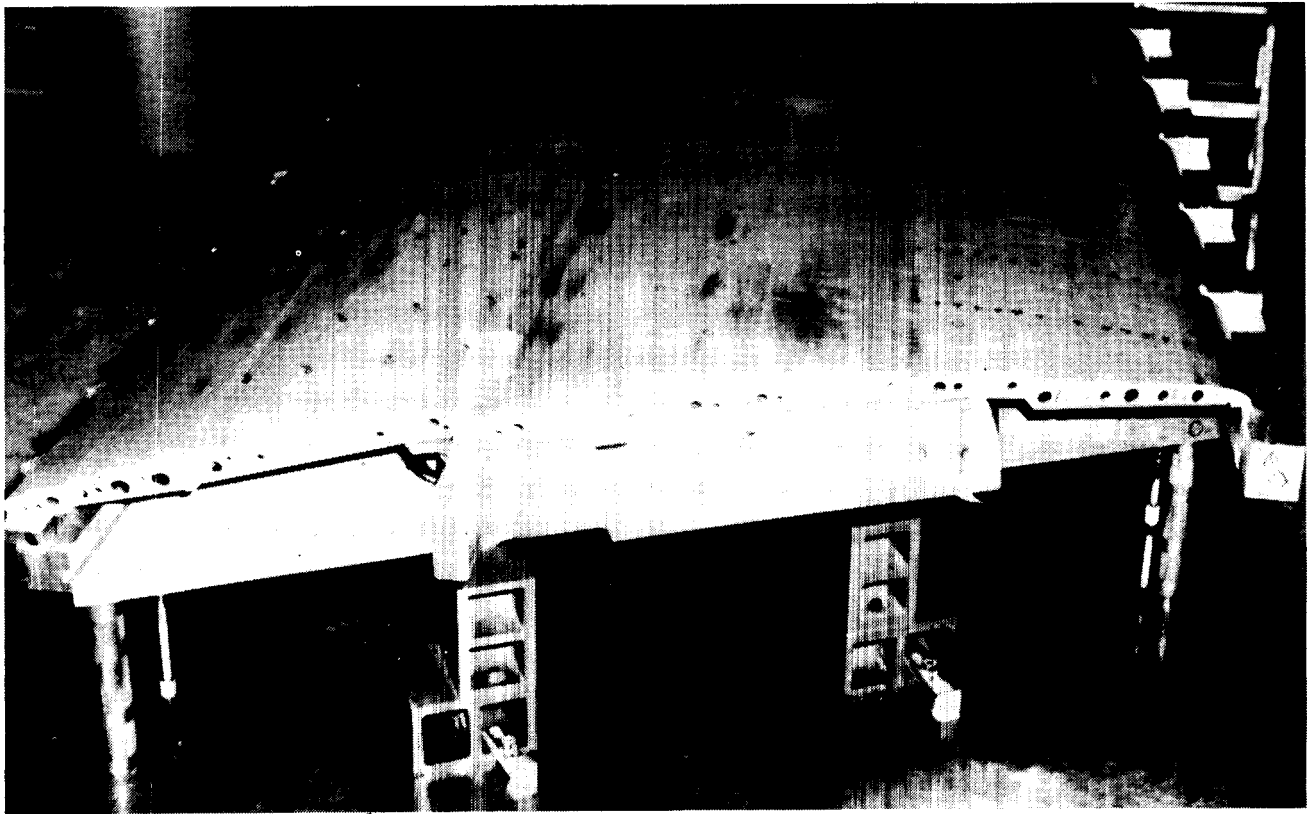
Figure 25. Concluded.



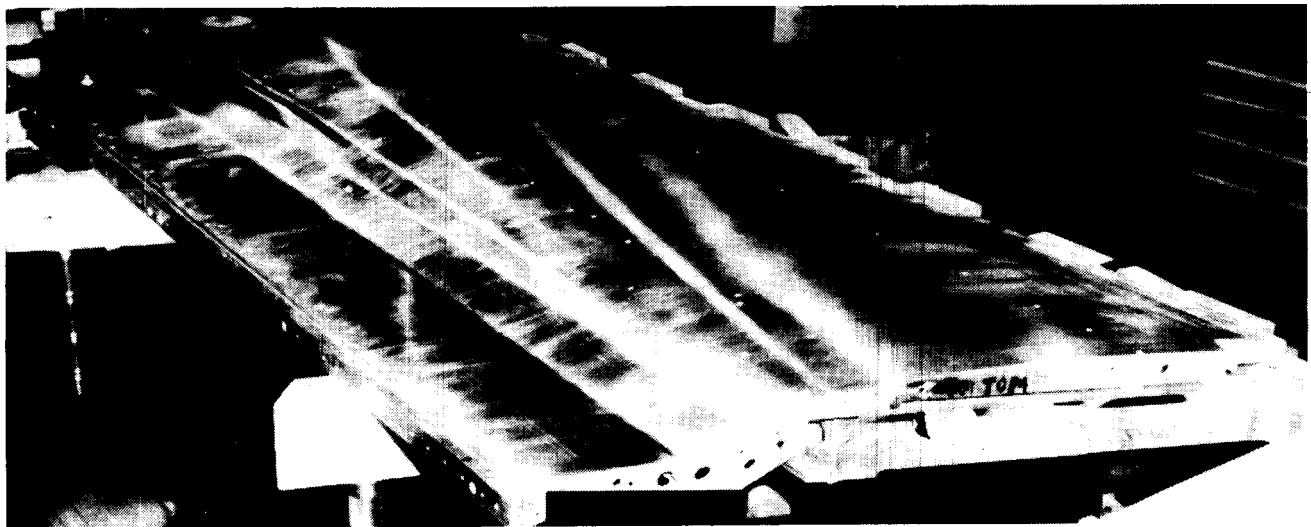
L-81-4677

Figure 26. Photograph of orifice drilling process on lower-surface forward panel.

ORIGINAL PAGE IS
OF POOR QUALITY



(a) Three upper-surface panels and box beam without flap.



(b) Lower-surface forward and center panels only and box beam.

Figure 27. Photographs of model suction-panel assemblies during fabrication process.

L-88-49



L-81-11,716

Figure 28. Photograph of wingbox installed in test section. Downstream view.

ORIGINAL PAGE IS
OF POOR QUALITY

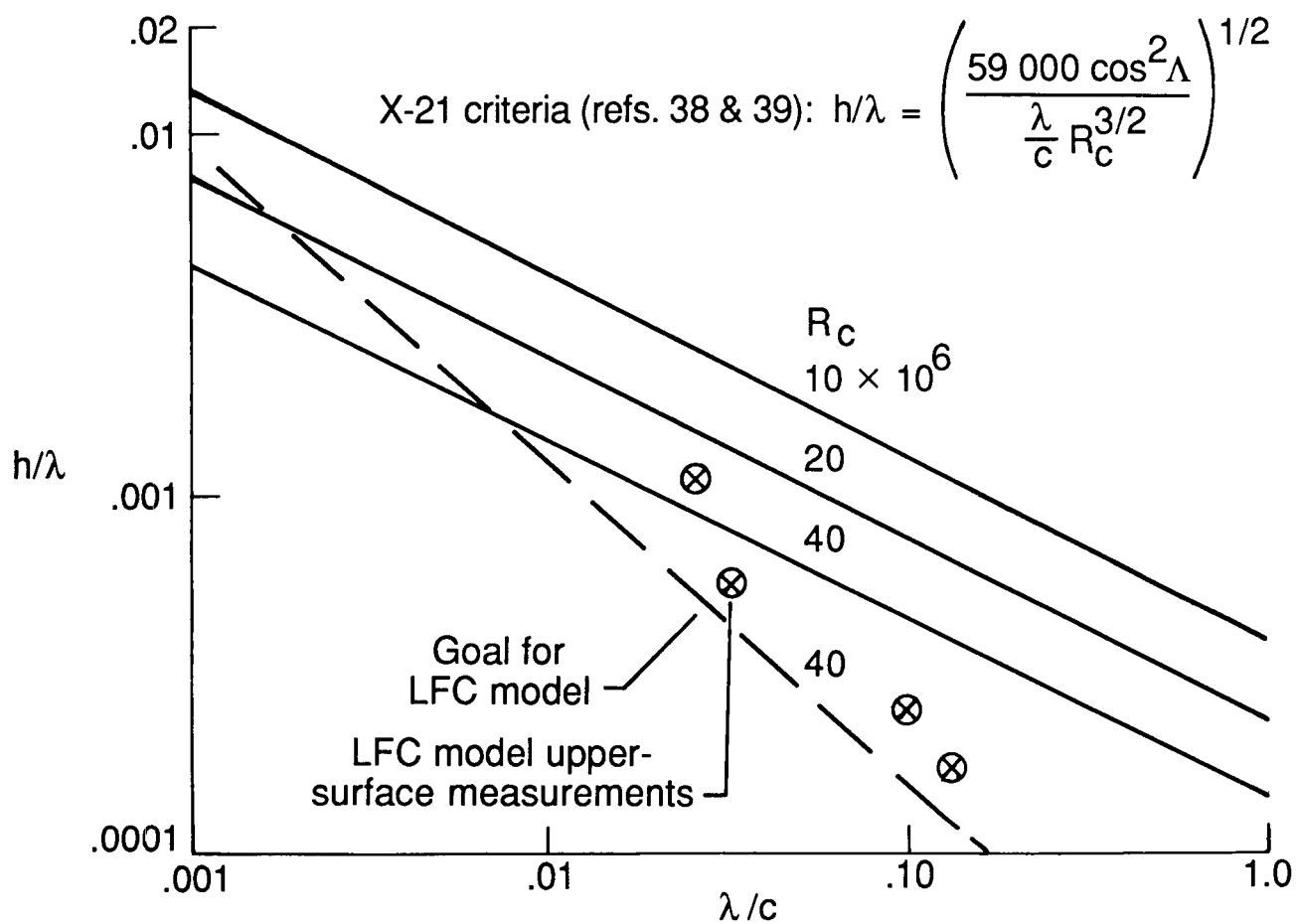
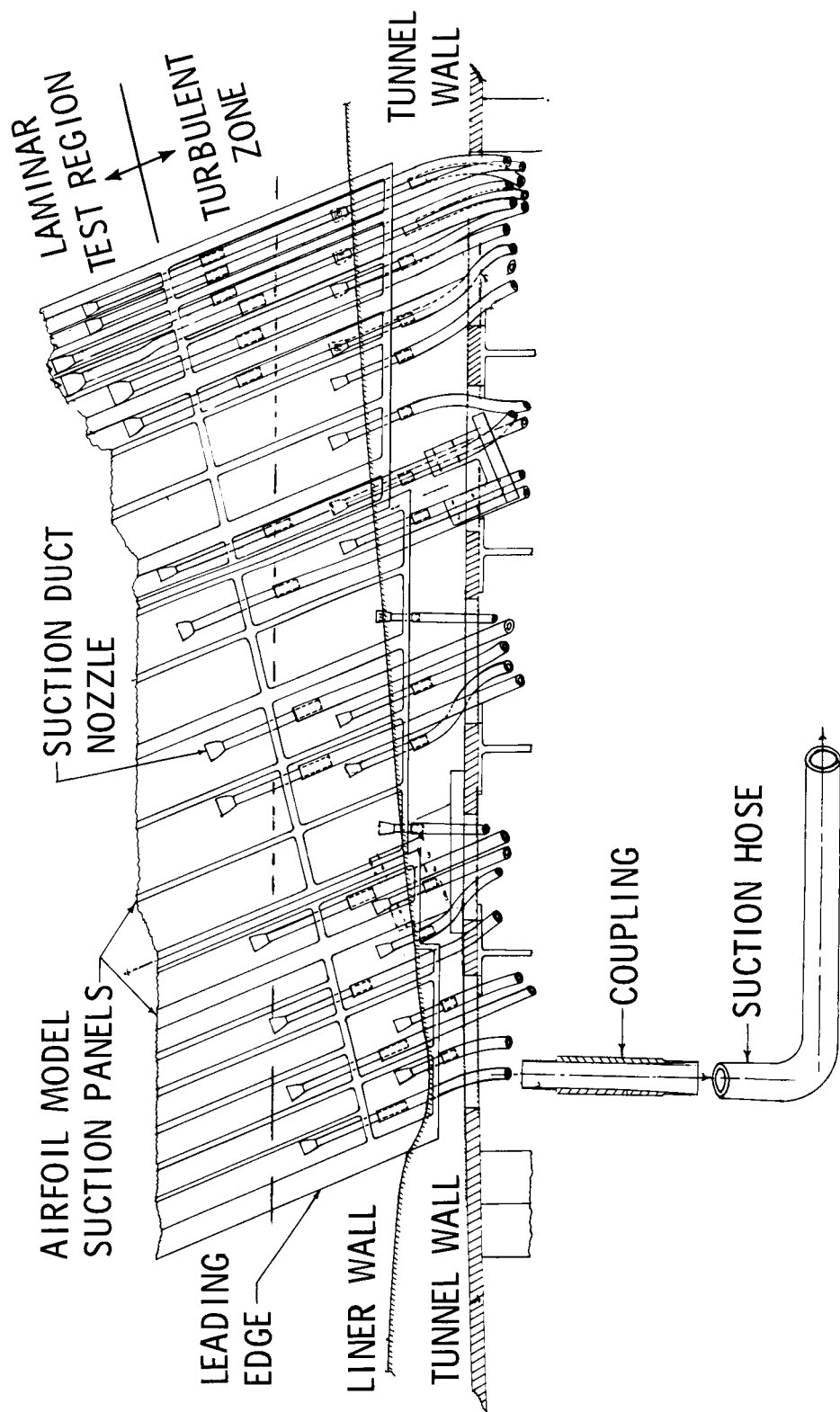


Figure 29. Comparison of variation of permissible amplitude ratio h/λ for multiple waves on subsonic and supercritical airfoils with full-chord LFC.



(a) Sketch of end of model nearest test section floor.

Figure 30. Internal suction ducting and nozzle layout.

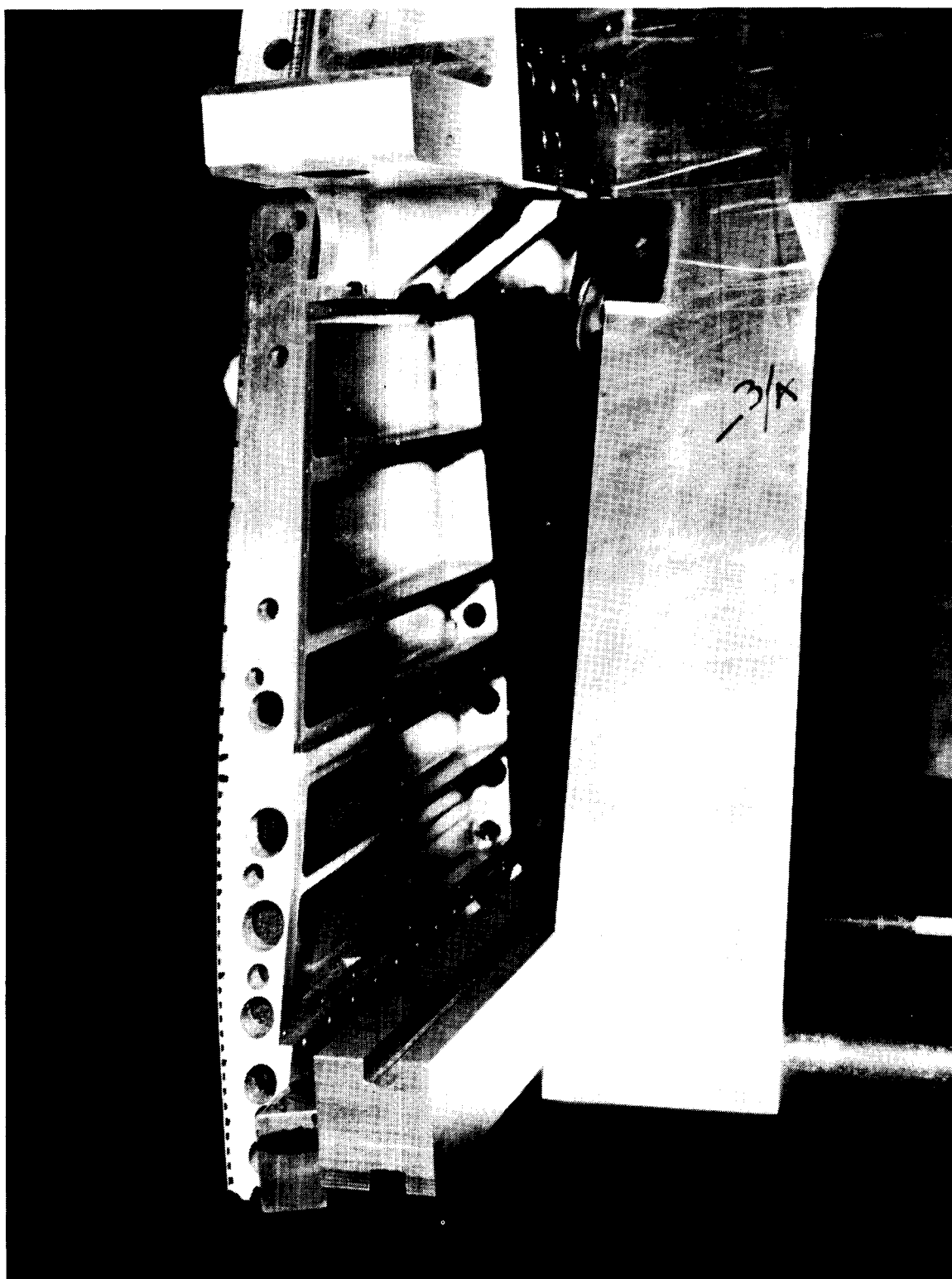
ORIGINAL PAGE IS
OF POOR QUALITY



L-81-8068

(b) Photograph of bulkheads and suction nozzles.

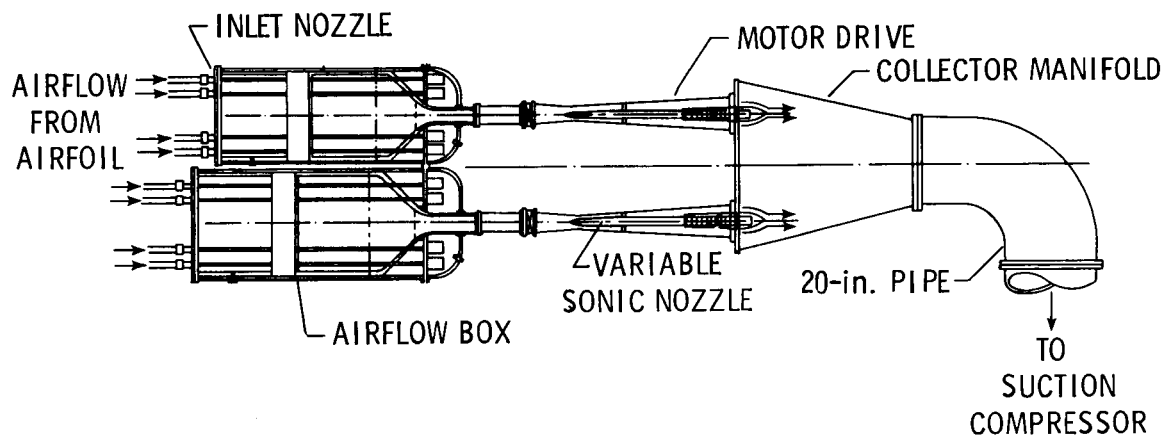
Figure 30. Concluded.



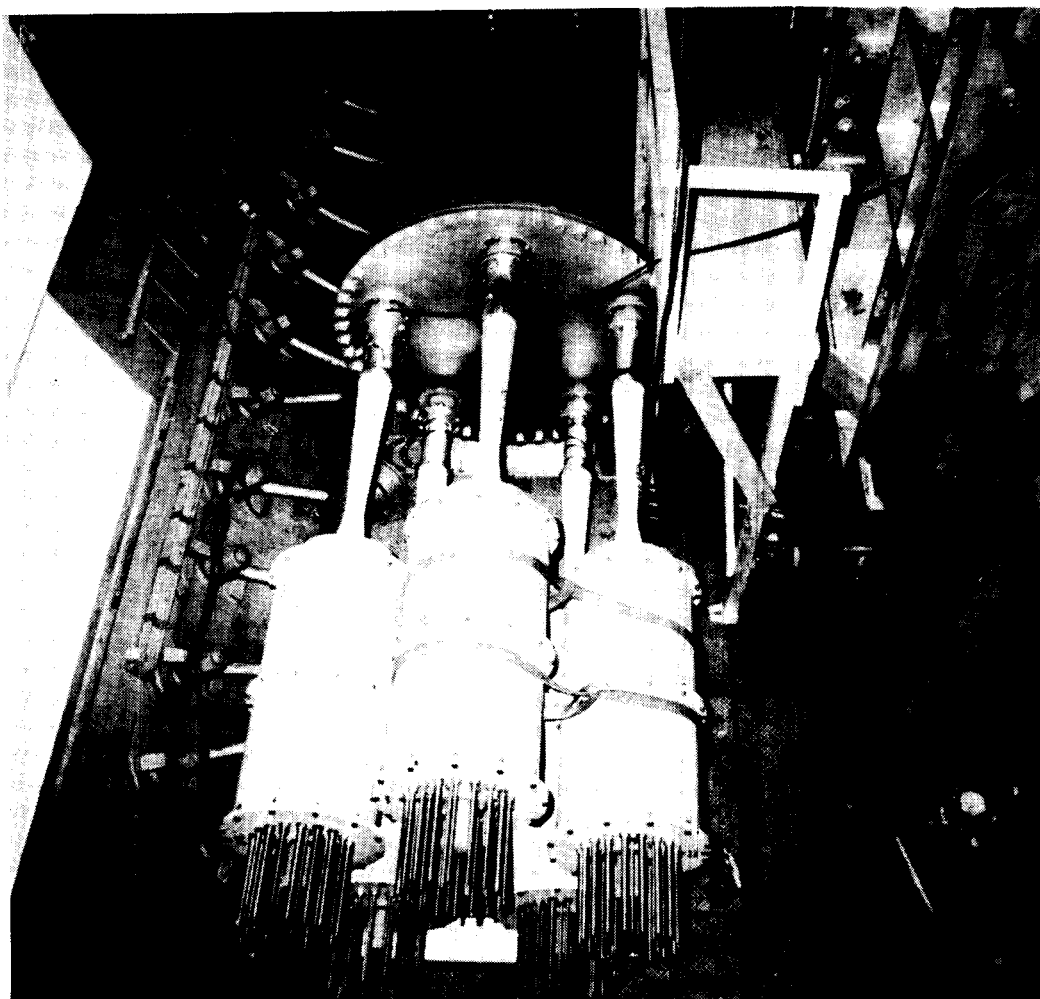
L-81-1313

Figure 31. Photograph of penetration holes in end of panel.

OF POOR QUALITY



(a) Sketch of airflow control boxes, variable sonic nozzles, and collector manifold and piping.



L-88-50

(b) Photograph of installed airflow boxes, variable sonic nozzles, and collector manifold and piping.

Figure 32. Airflow control system.

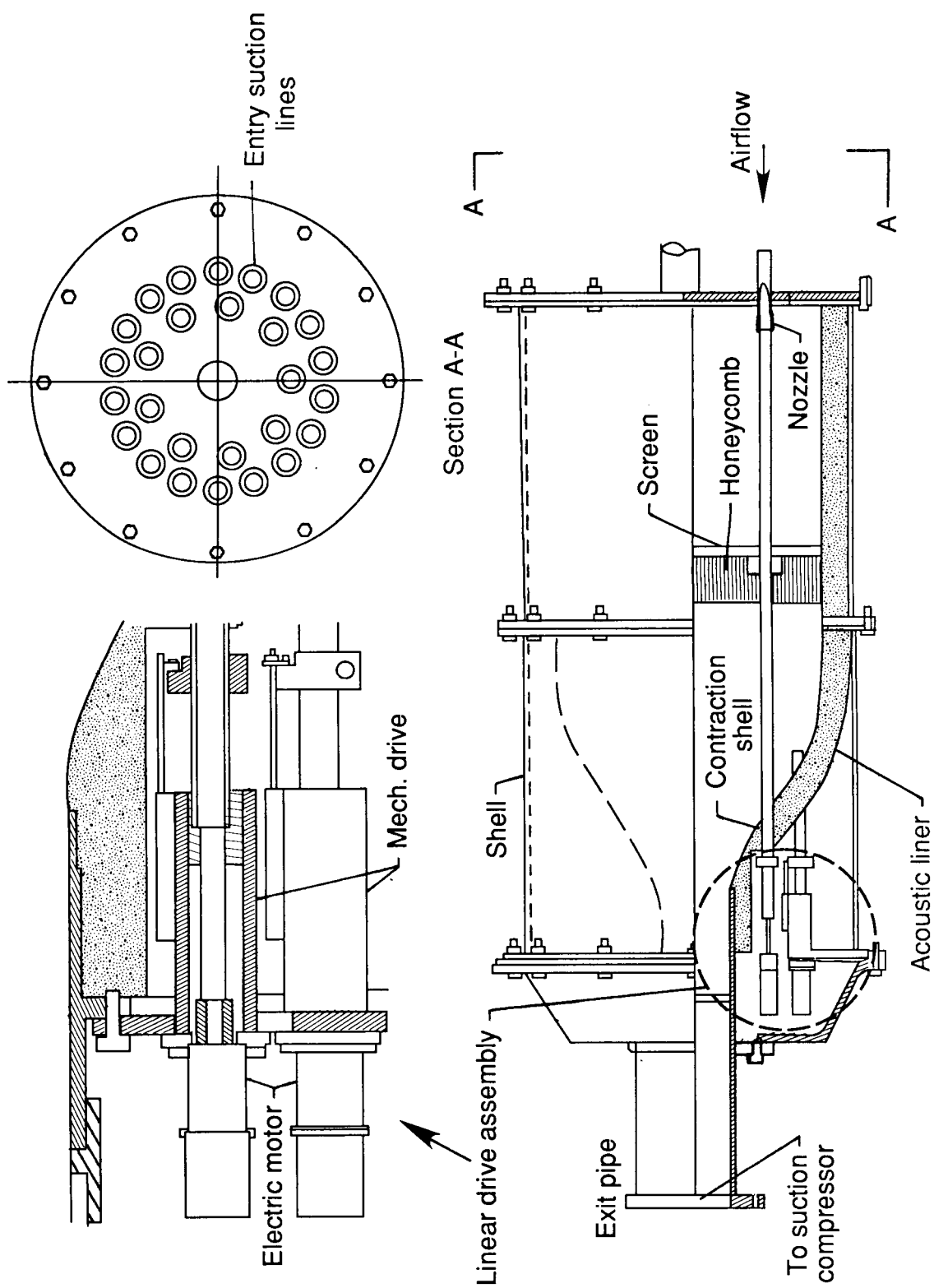
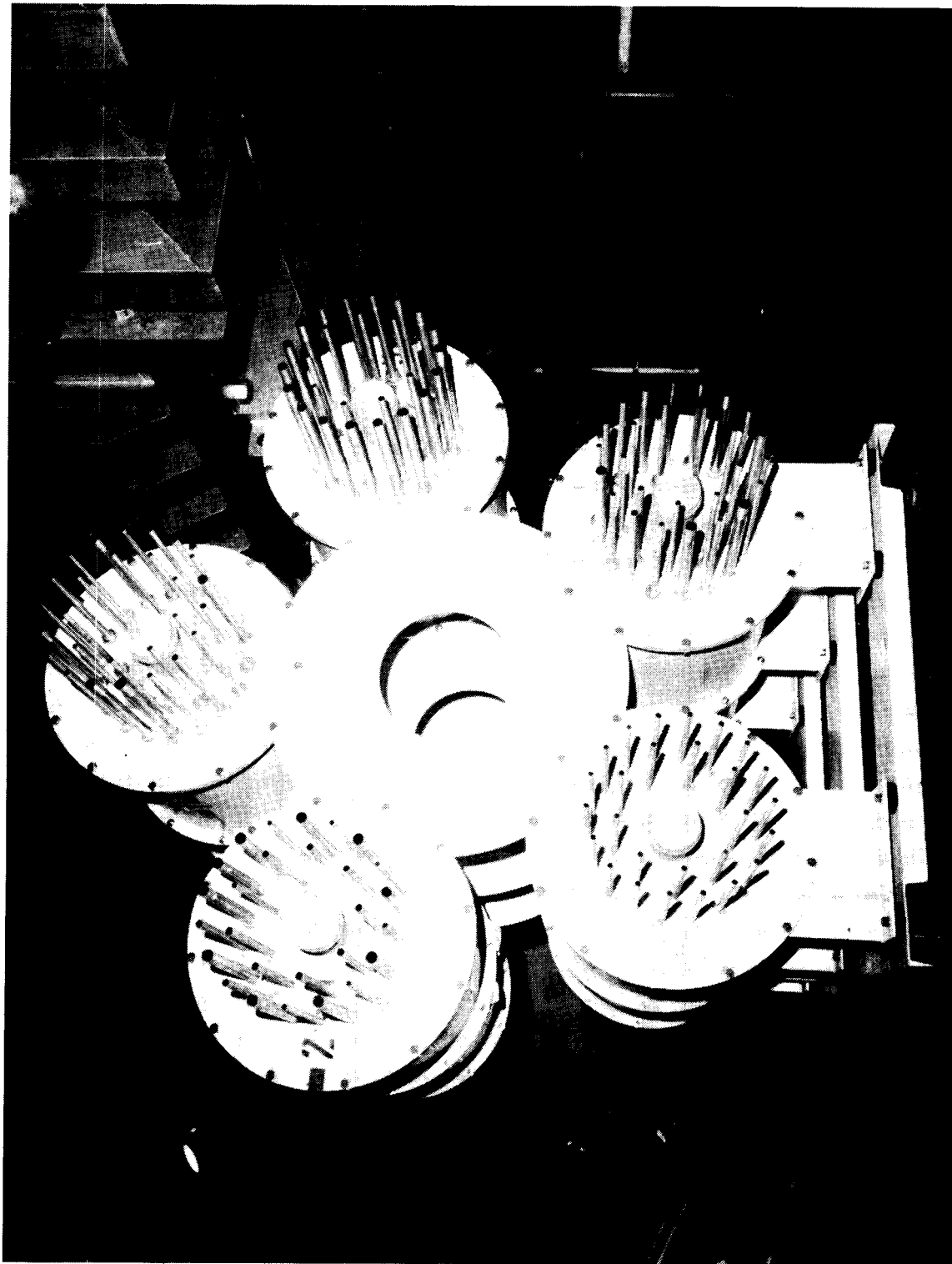


Figure 33. Sketch showing details of airflow control boxes.

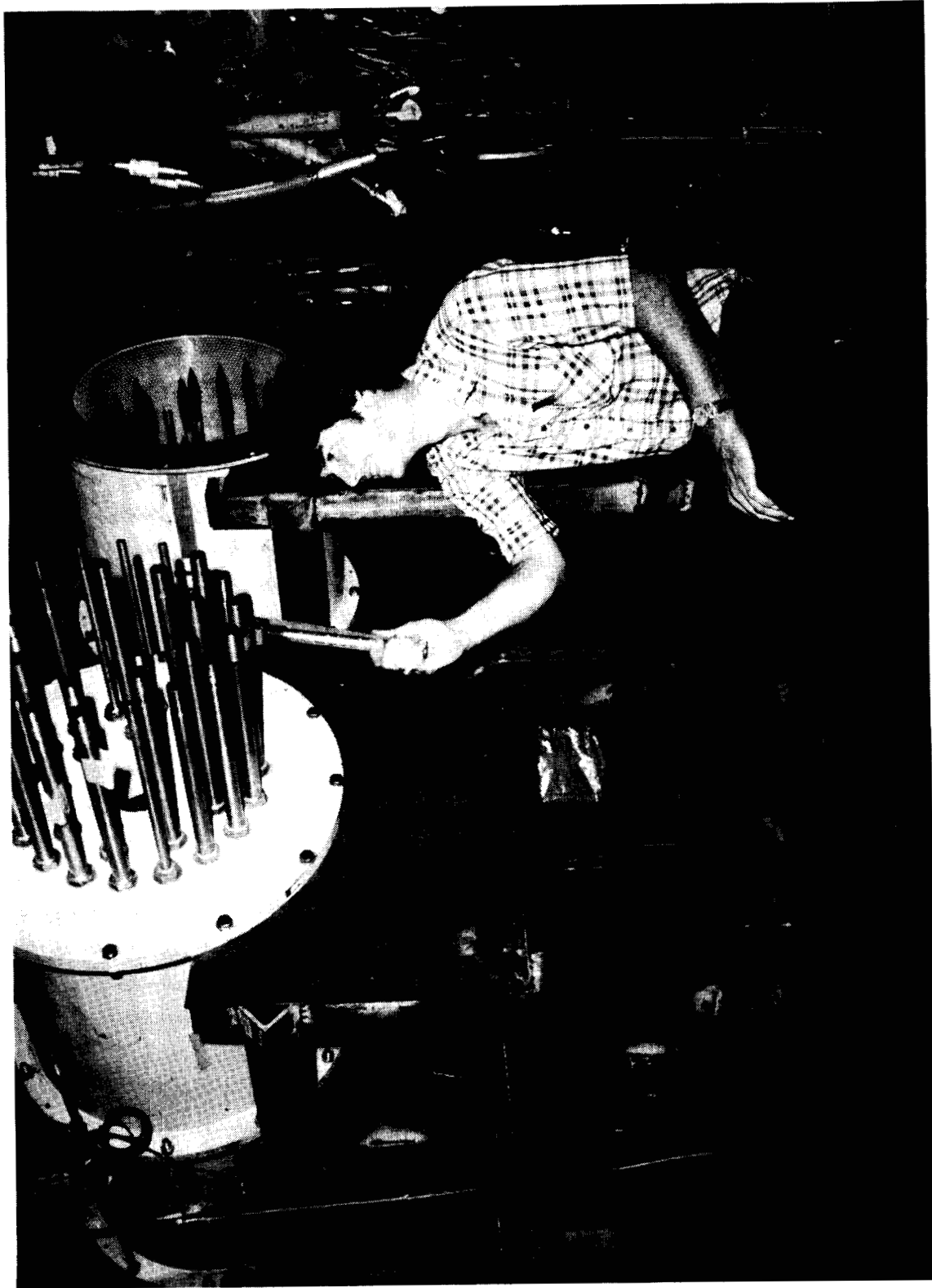


L-81-8928

(a) Upstream faces.

Figure 34. Photographs of airflow control boxes.

ORIGINAL PAGE IS
OF POOR QUALITY

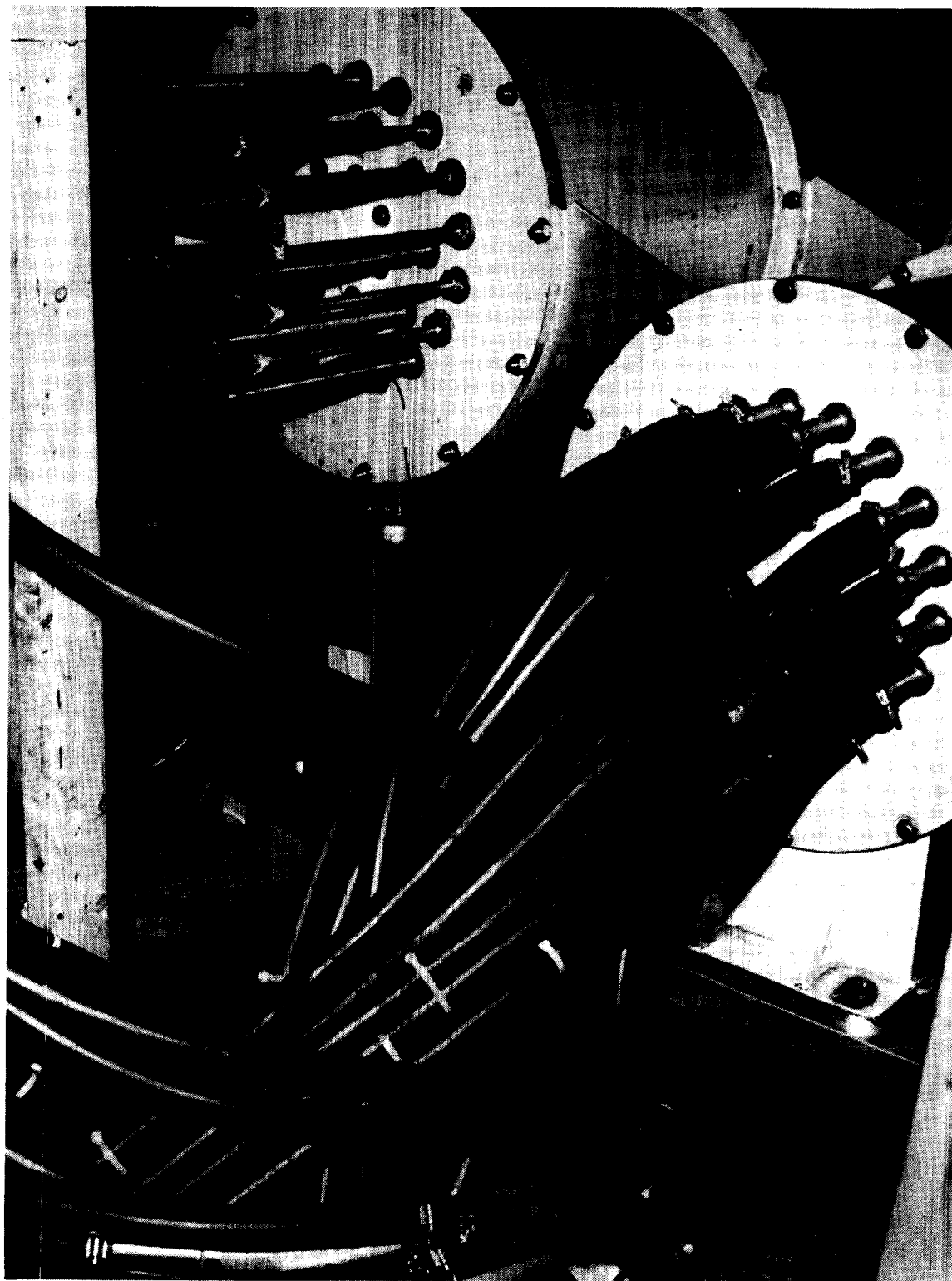


L-82-7,405

(b) Pipes in face of airflow control boxes.

Figure 34. Continued.

ORIGINAL PAGE IS
OF POOR QUALITY

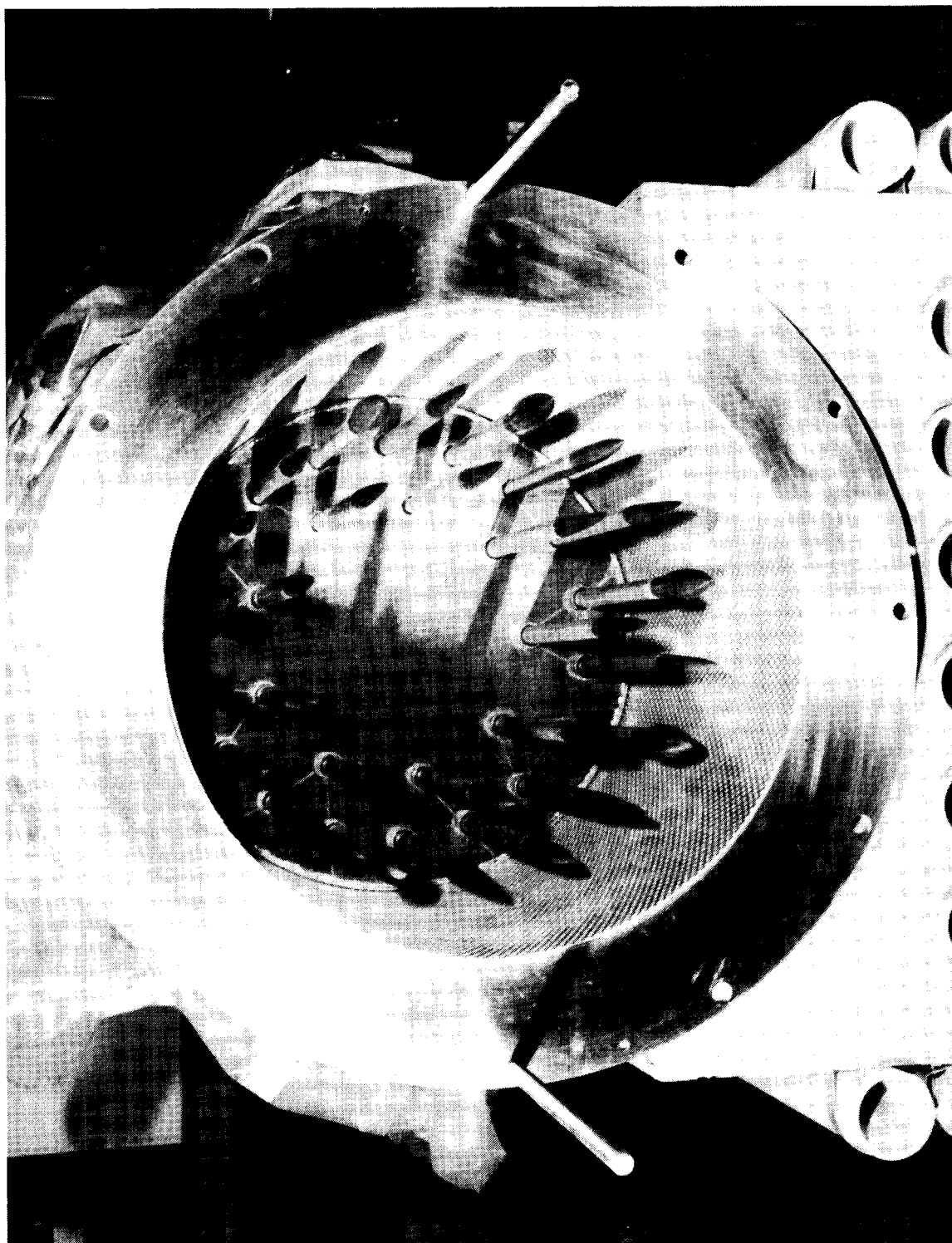


L-82-7,947

(c) Suction hoses to pipes connected to face of airflow control boxes.

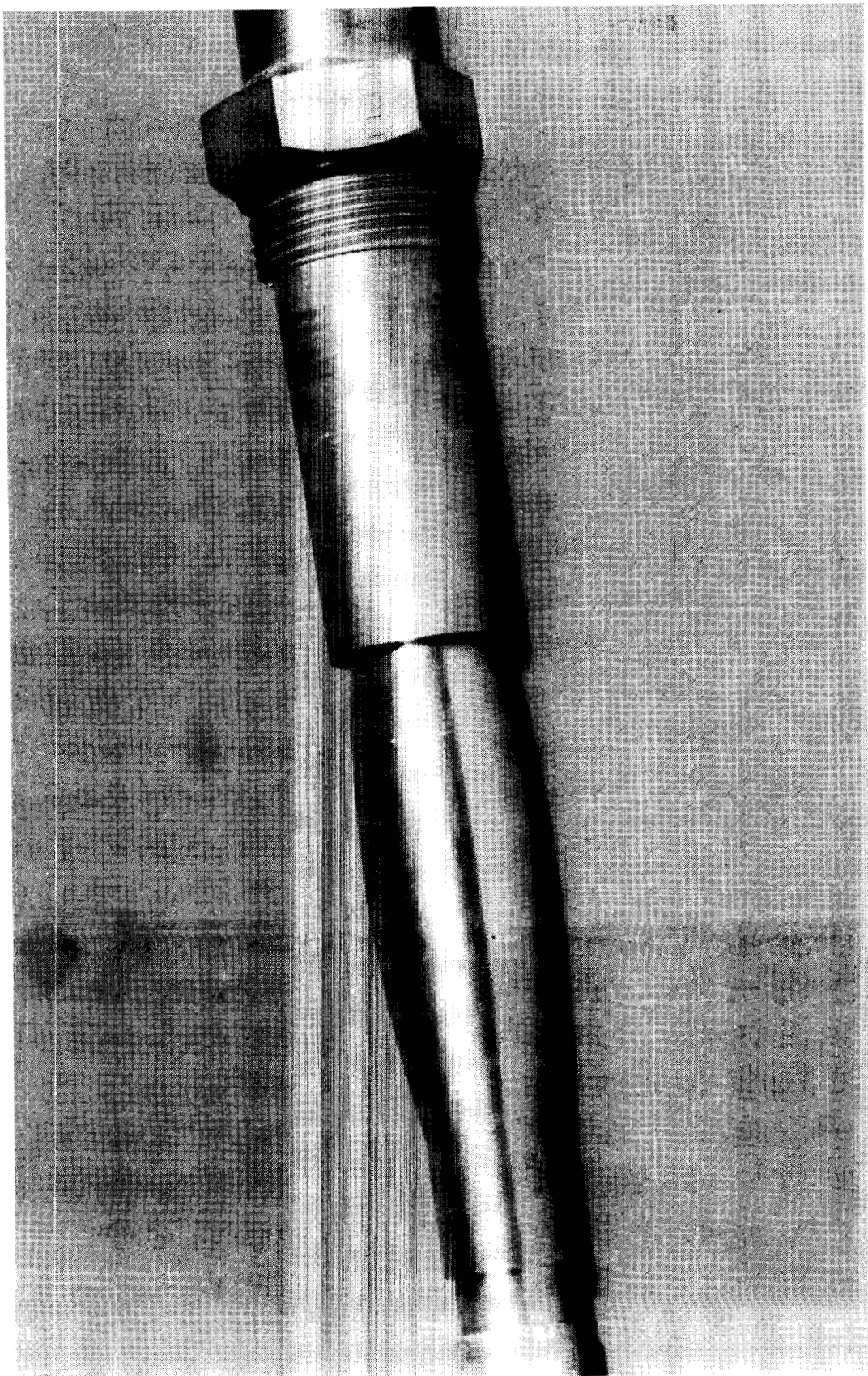
Figure 34. Continued.

L-81-8502



(d) Needle valves in airflow control box.

Figure 34. Continued.

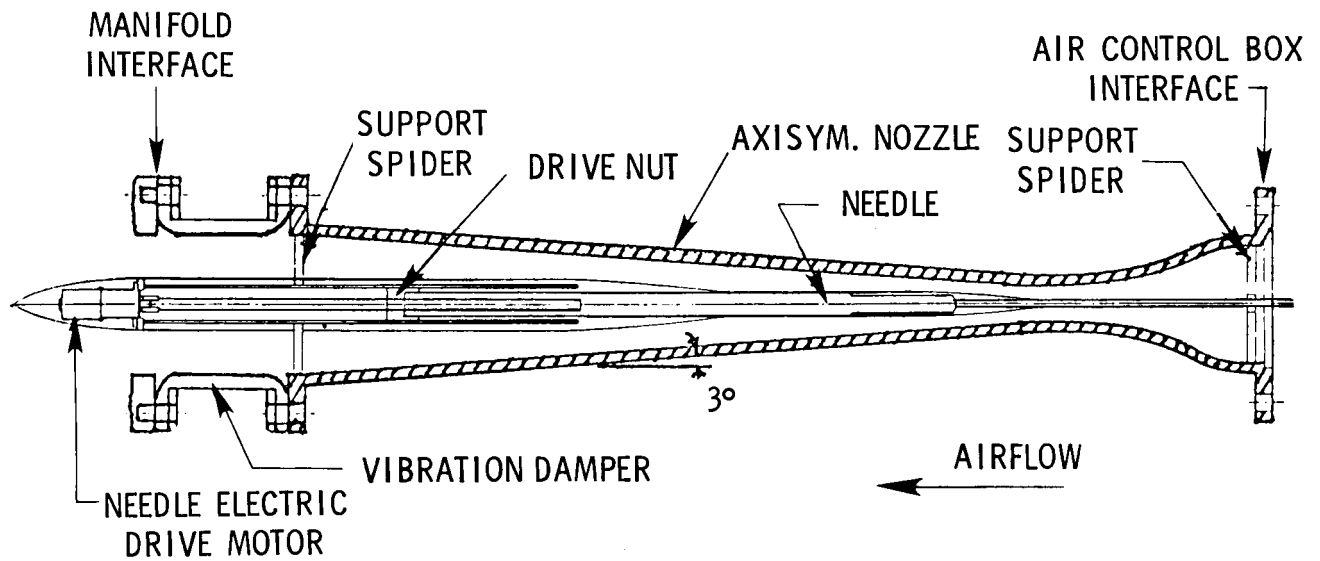


L-81-2385

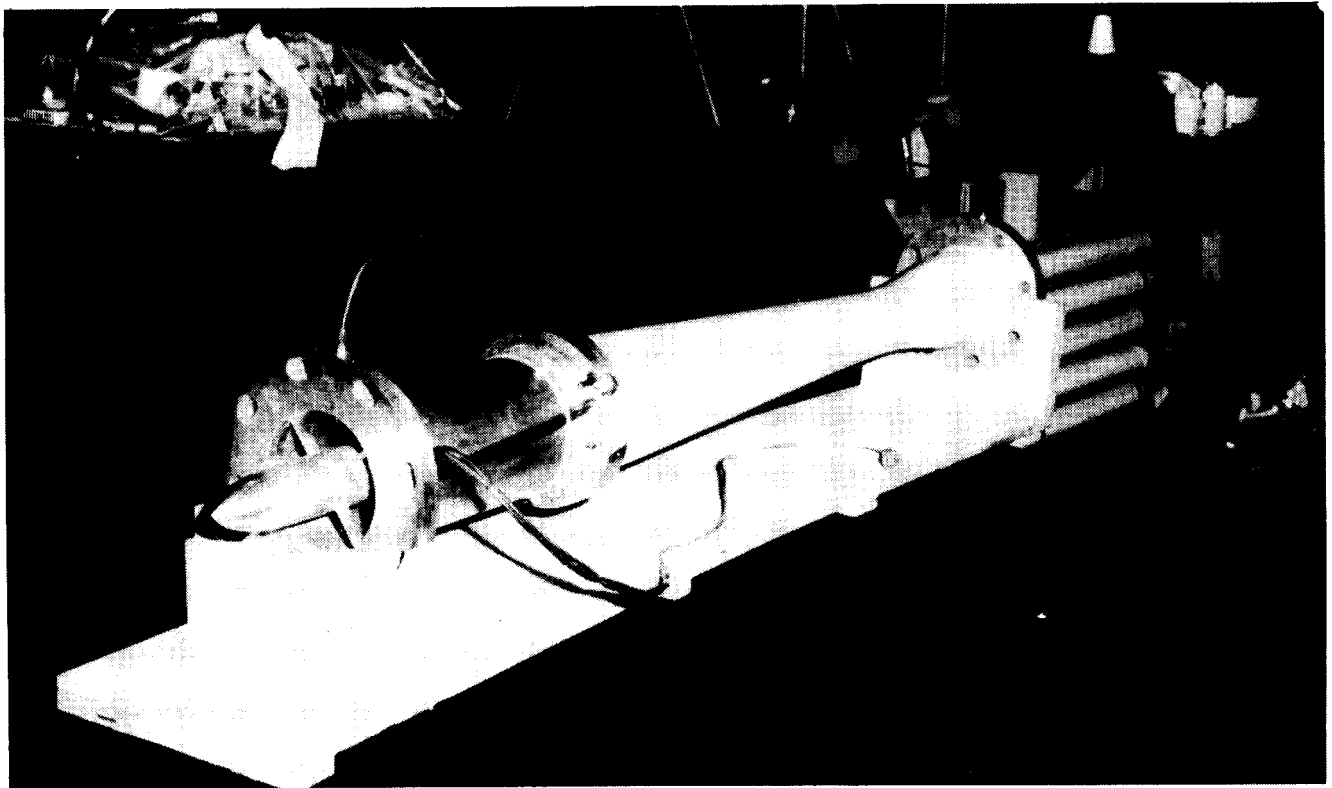
(e) Needle valve in pipe.

Figure 34. Concluded.

ORIGINAL PAGE IS
OF POOR QUALITY



(a) Sketch showing variable sonic nozzle concept.

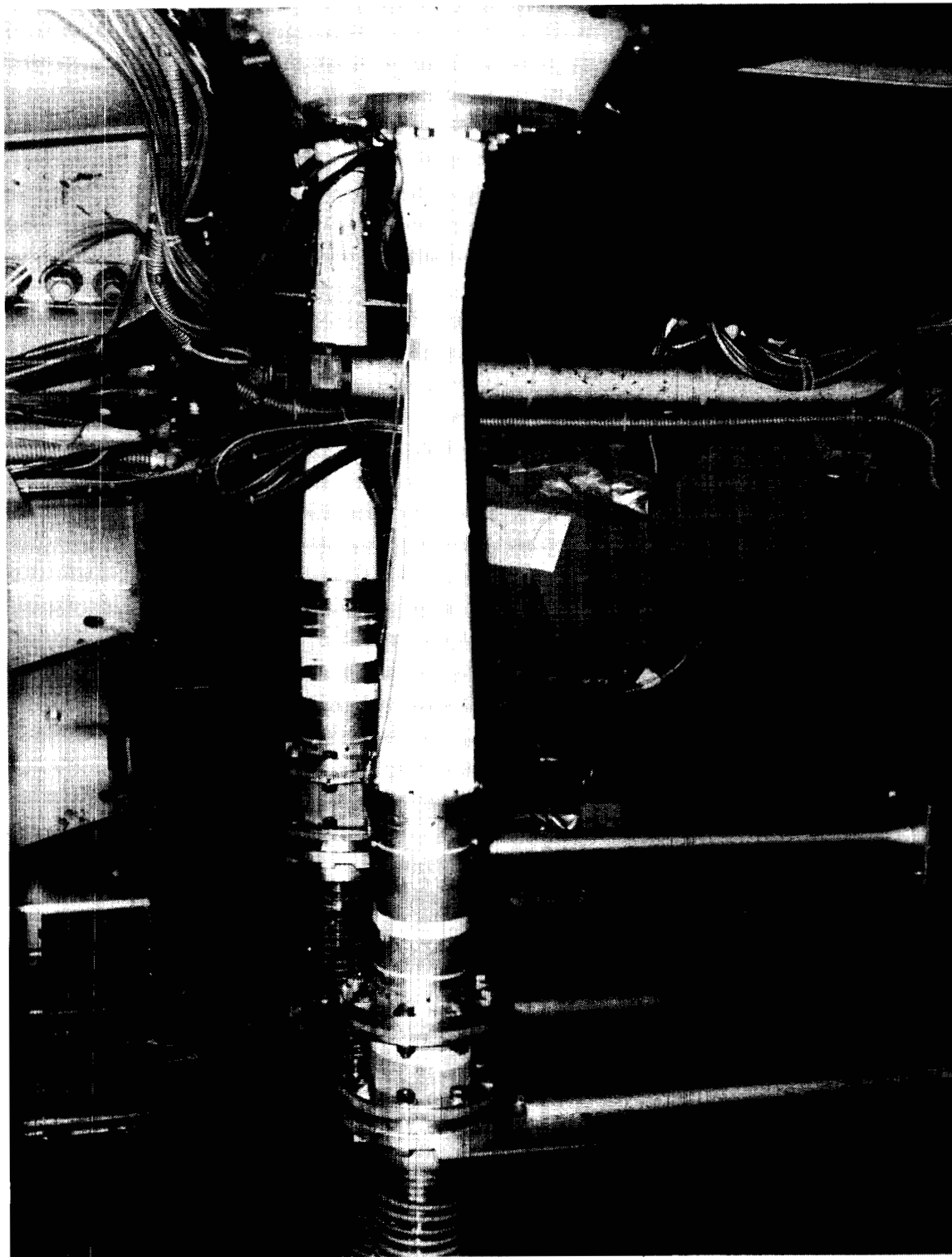


L-88-51

(b) Photograph of single sonic nozzle before installation.

Figure 35. Variable sonic nozzle.

ORIGINAL PAGE IS
OF POOR QUALITY



L-82-7,944

(c) Photograph of installed variable sonic nozzles.

Figure 35. Concluded.

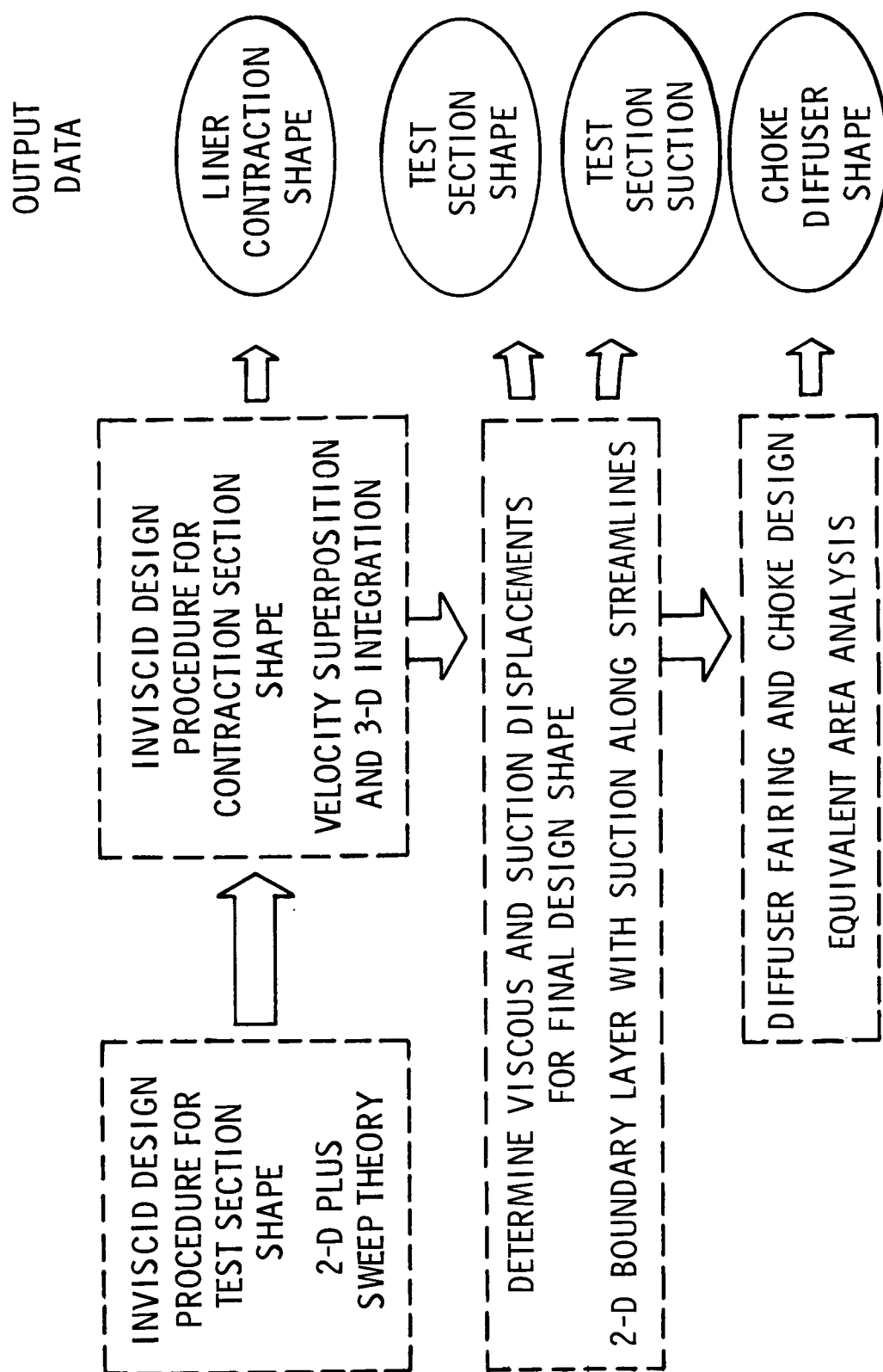


Figure 36. Block diagram outlining tunnel-liner contour-design procedure.

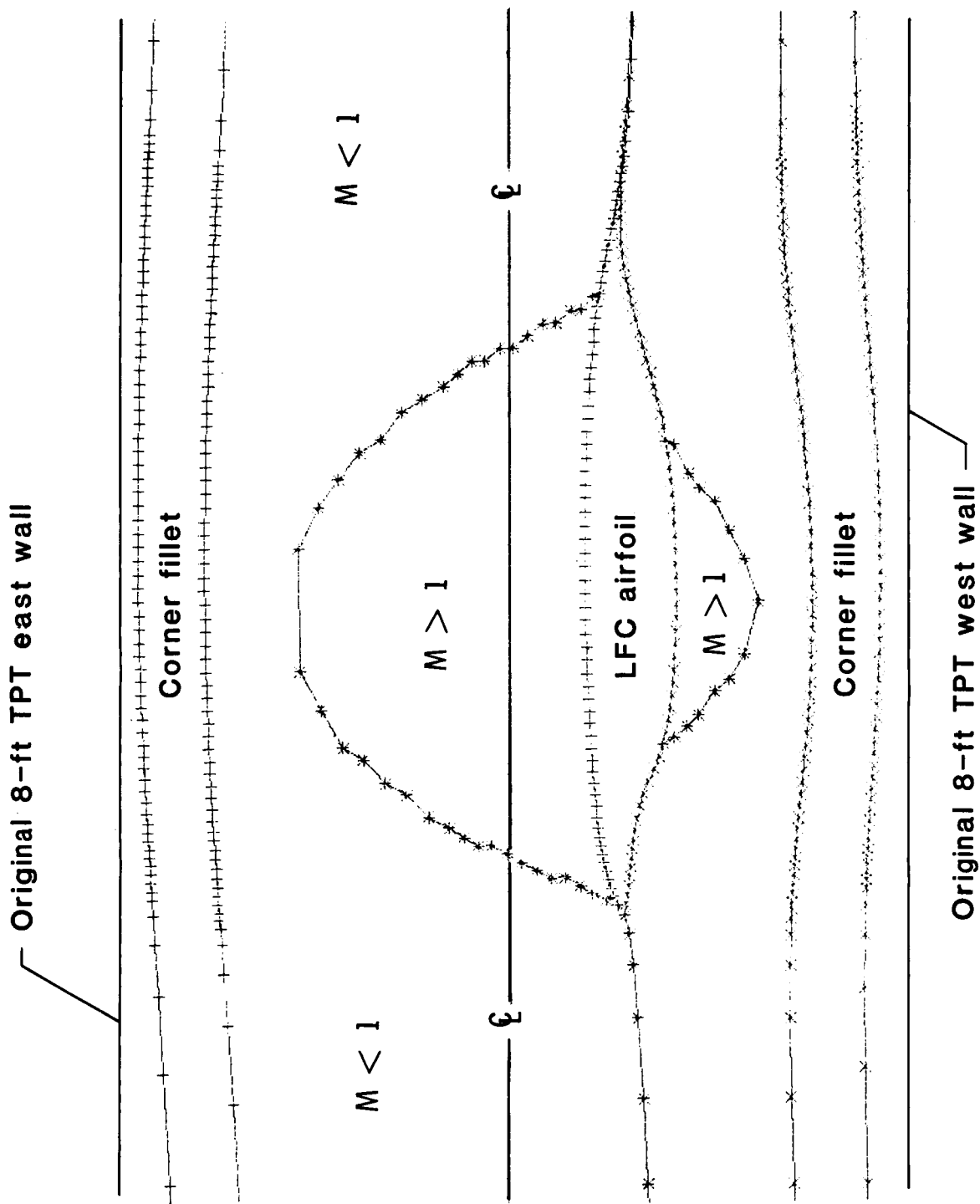


Figure 37. Scaled illustration of relative size of LFC airfoil model, 3-D supersonic flow regions, and inviscid liner shape.

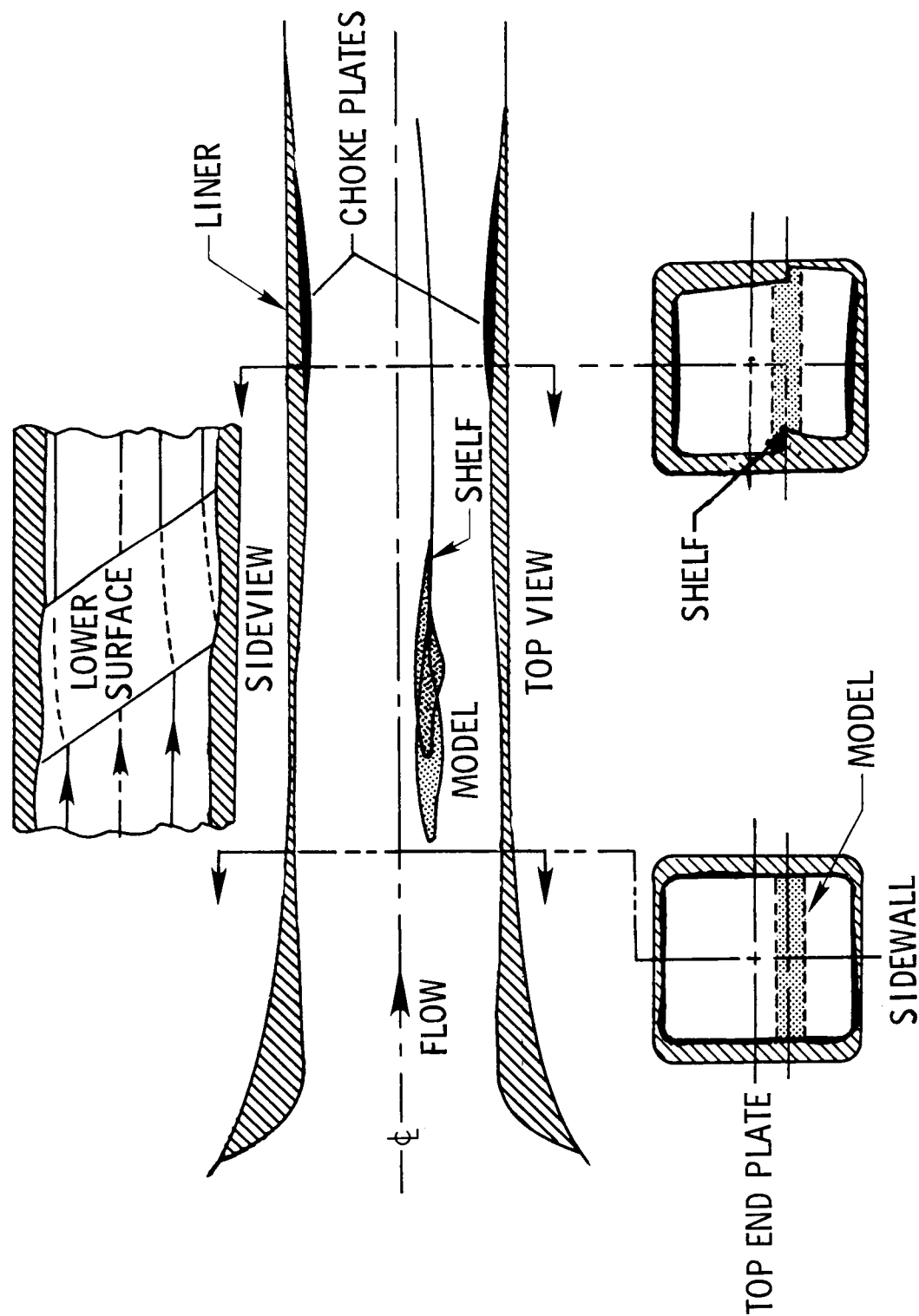


Figure 38. Sketch of liner contours.

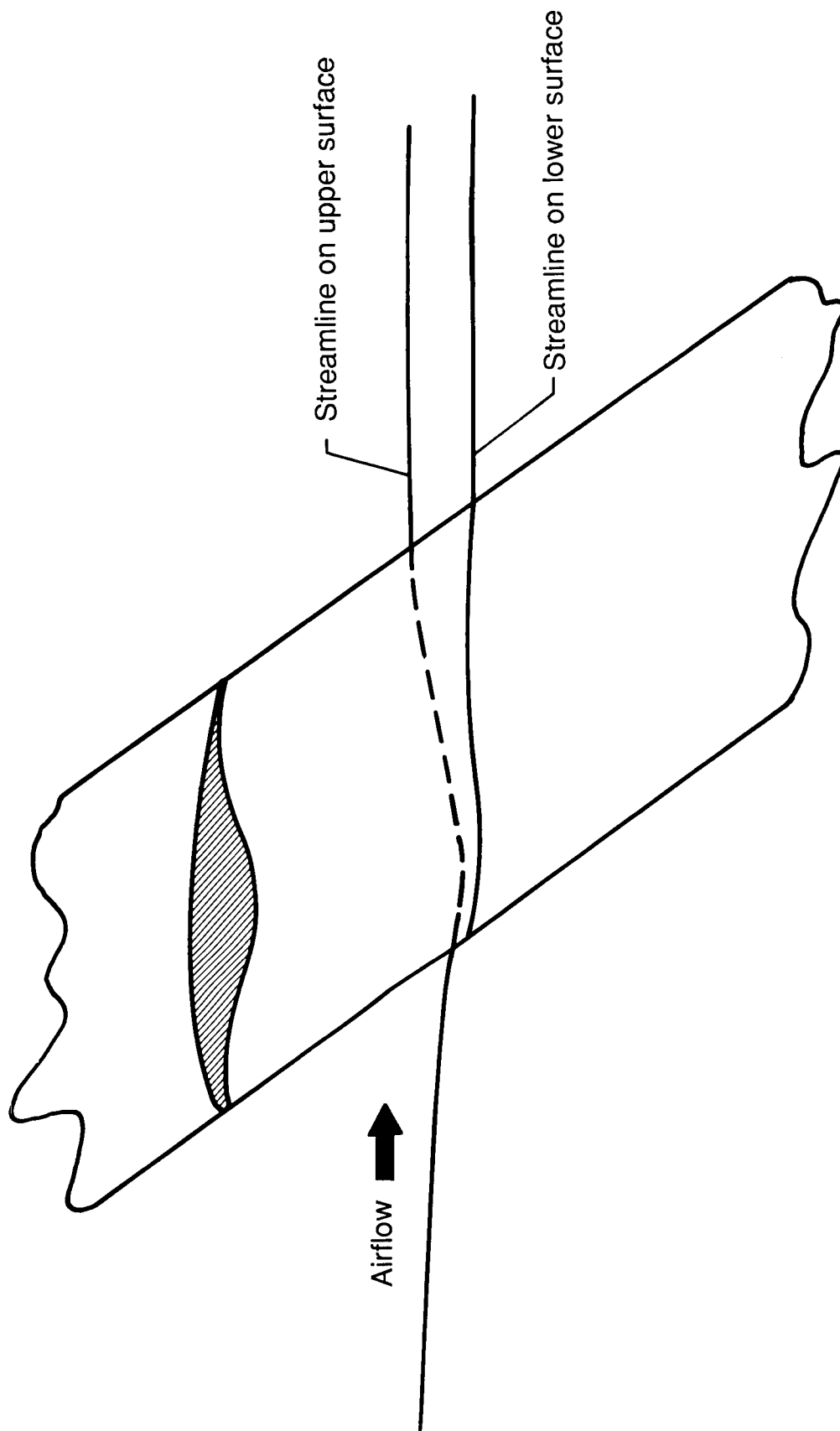
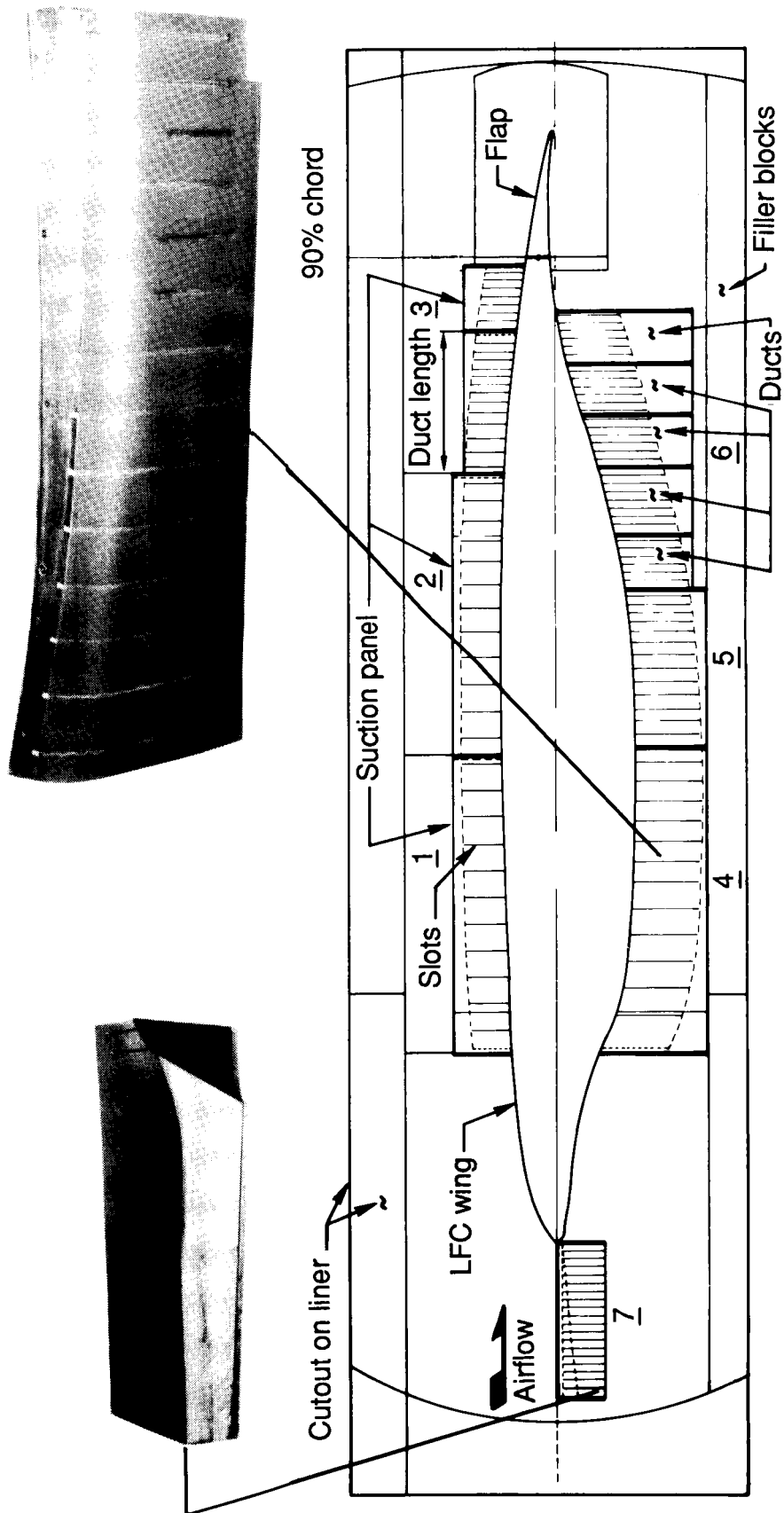


Figure 39. Sketch of spanwise streamline displacement over swept wing. View from lower surface.



End plate view

L-88-52

(a) Sketch of suction collar around ends of airfoil model.

Figure 40. Suction collar.

ORIGINAL PAGE IS
OF POOR QUALITY

L-82-3,623

(b) Segment of suction collar above aft upper surface in ceiling.

Figure 40. Continued.



L-82-3,628

(c) Segment of suction collar below aft lower surface in ceiling.

Figure 40. Continued.

ORIGINAL PAGE IS
OF POOR QUALITY



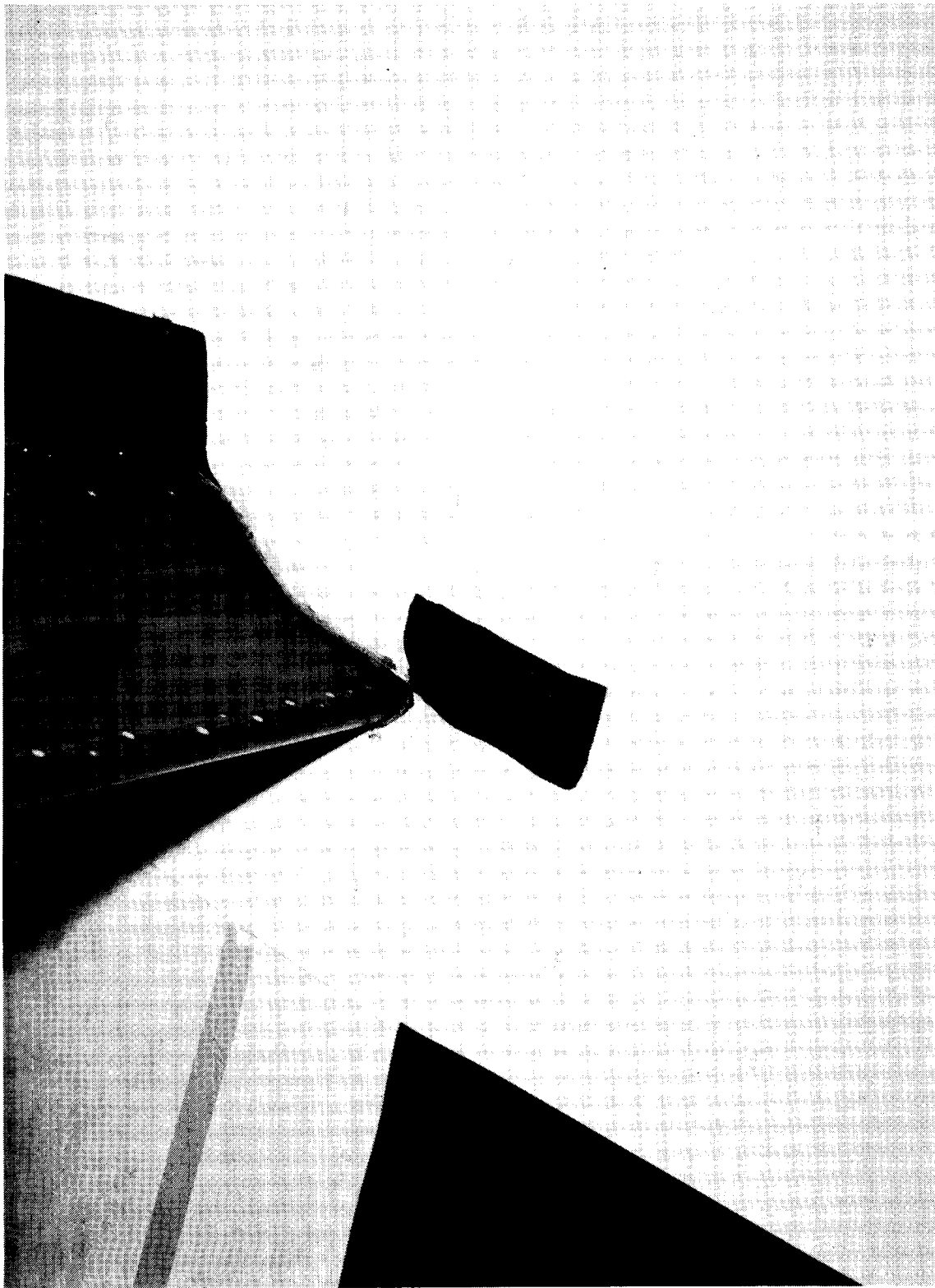
L-82-3,621

(d) Segments of suction collar above mid upper surface and ahead of leading edge in ceiling.

Figure 40. Continued.

ORIGINAL PAGE IS
OF POOR QUALITY

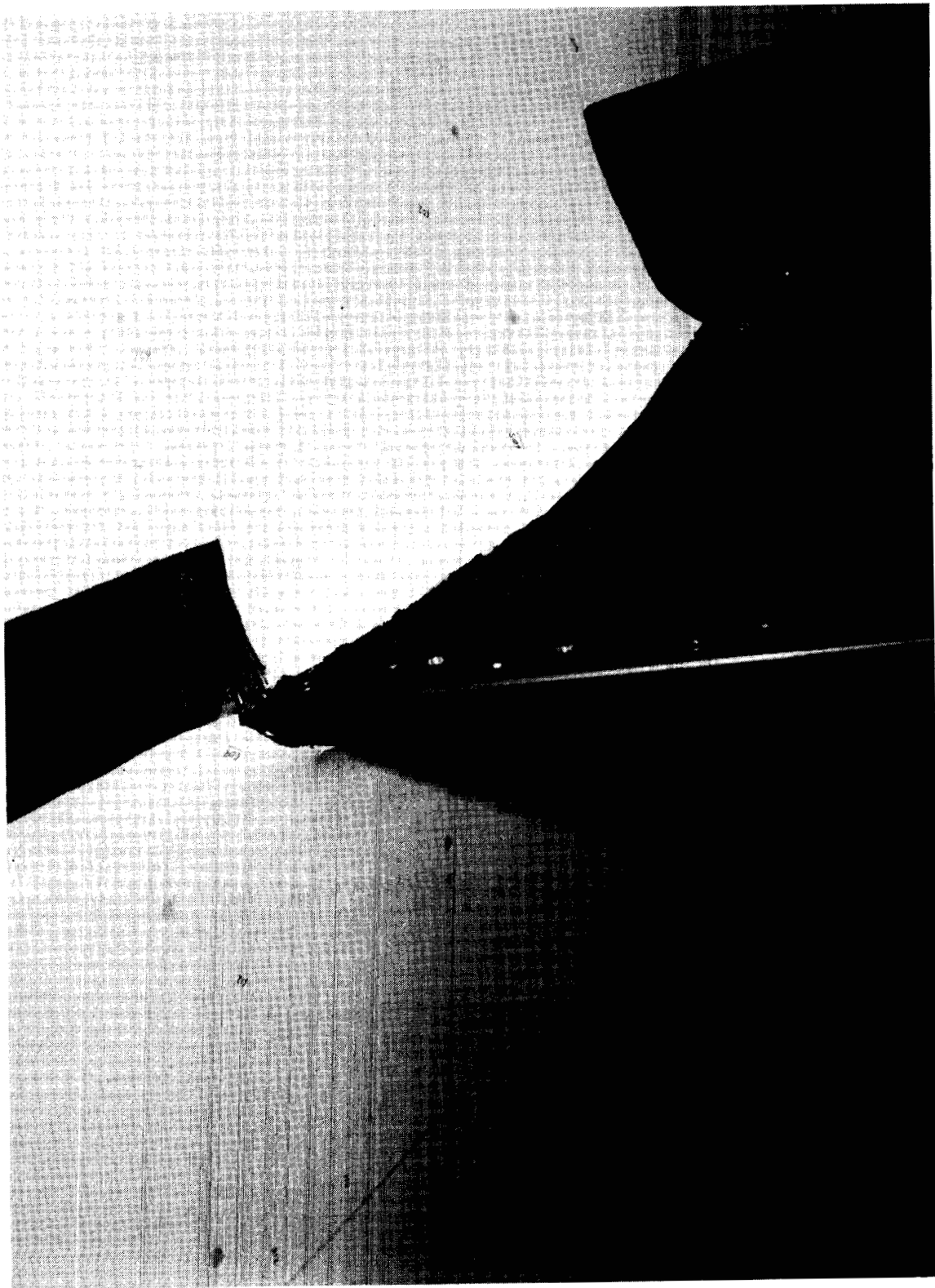
L-82-3,625



(e) Segment of suction collar ahead of leading edge in floor.

Figure 40. Continued.

ORIGINAL PAGE IS
OF POOR QUALITY

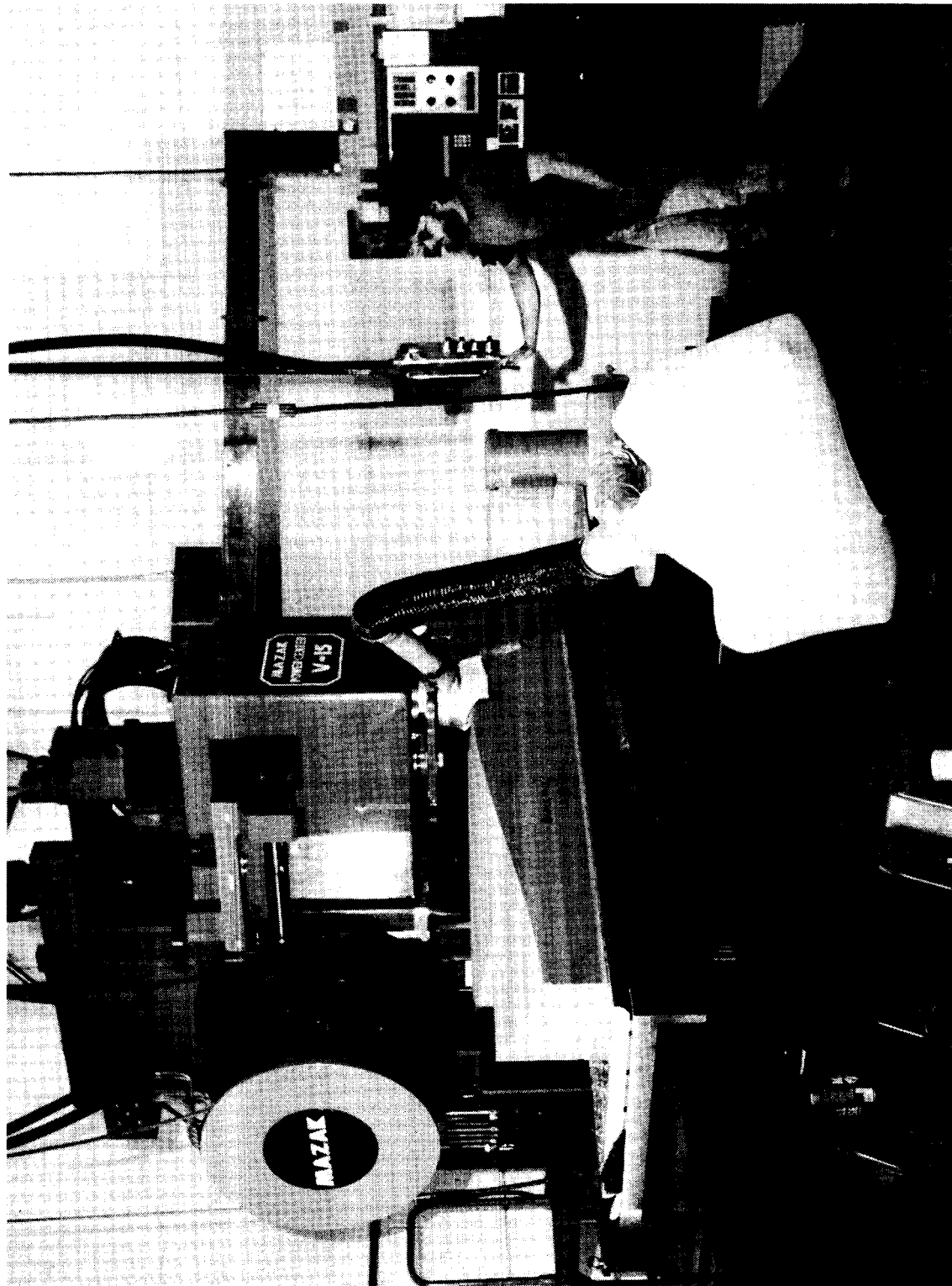


L-82-3,622

(f) Segments of suction collar ahead of leading edge and below mid lower surface in ceiling.

Figure 40. Concluded.

ORIGINAL PAGE IS
OF POOR QUALITY



L-80-9485

(a) Overall view.

Figure 41. Photographs of liner-block milling process.

ORIGINAL PAGE IS
OF POOR QUALITY

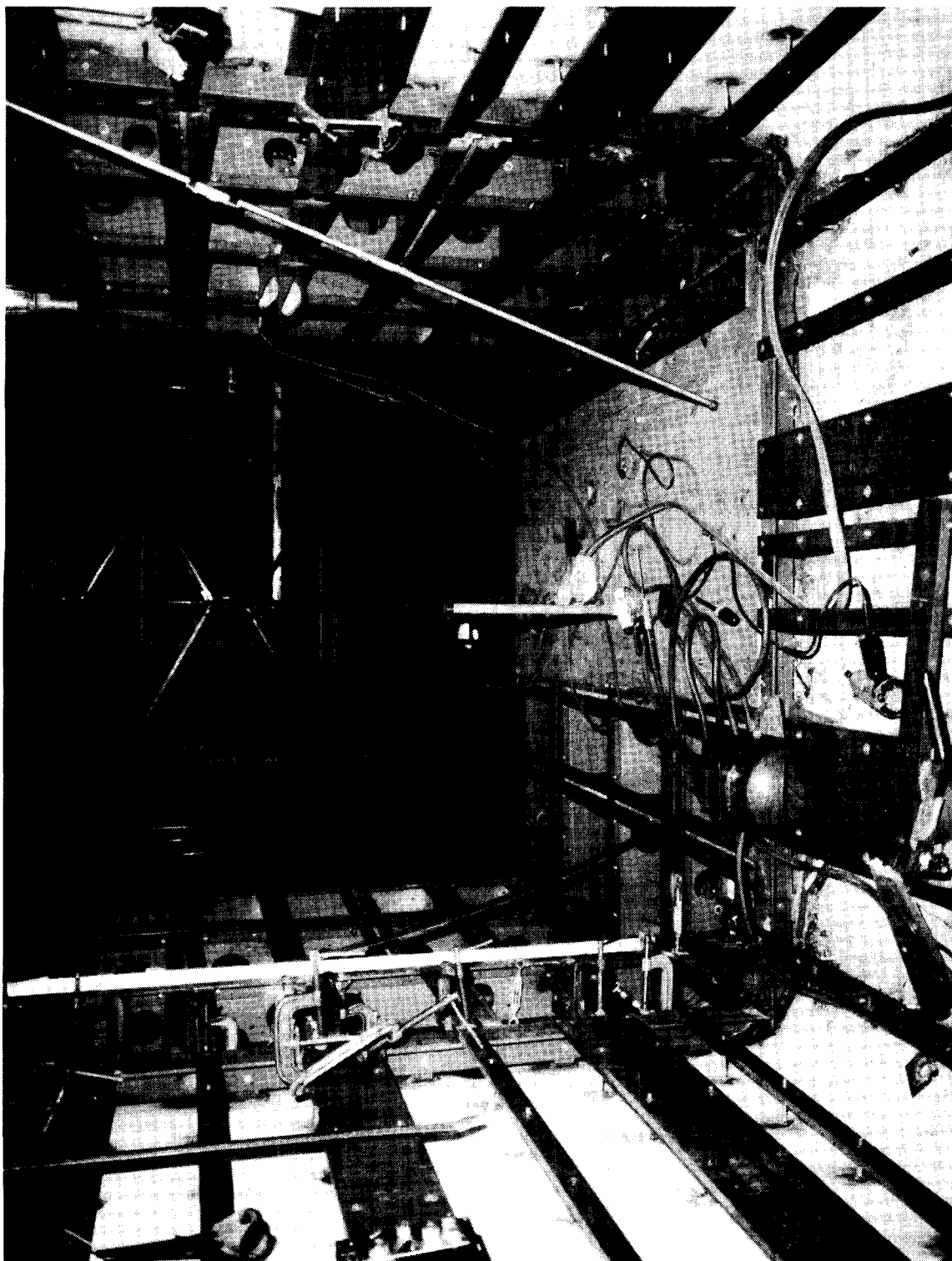


L-80-9483

(b) Closeup view.

Figure 41. Concluded.

ORIGINAL PAGE IS
OF POOR QUALITY



L-81-7721

(a) Upstream view of liner substructure.

Figure 42. Photographs of liner installation.

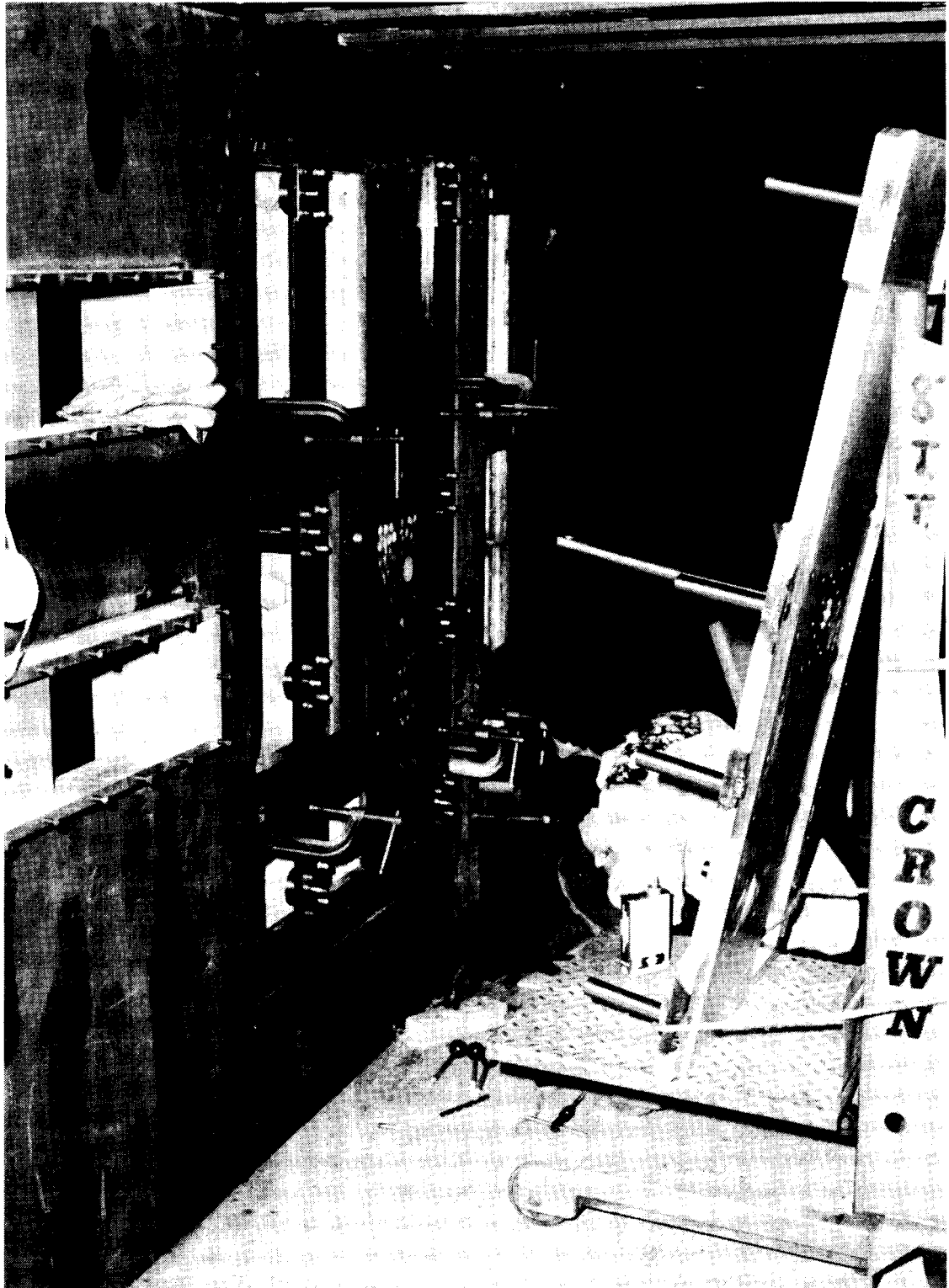
ORIGINAL PAGE IS
OF POOR QUALITY

L-81-11,414



(b) Attaching liner substructure to test section wall.

Figure 42. Continued.

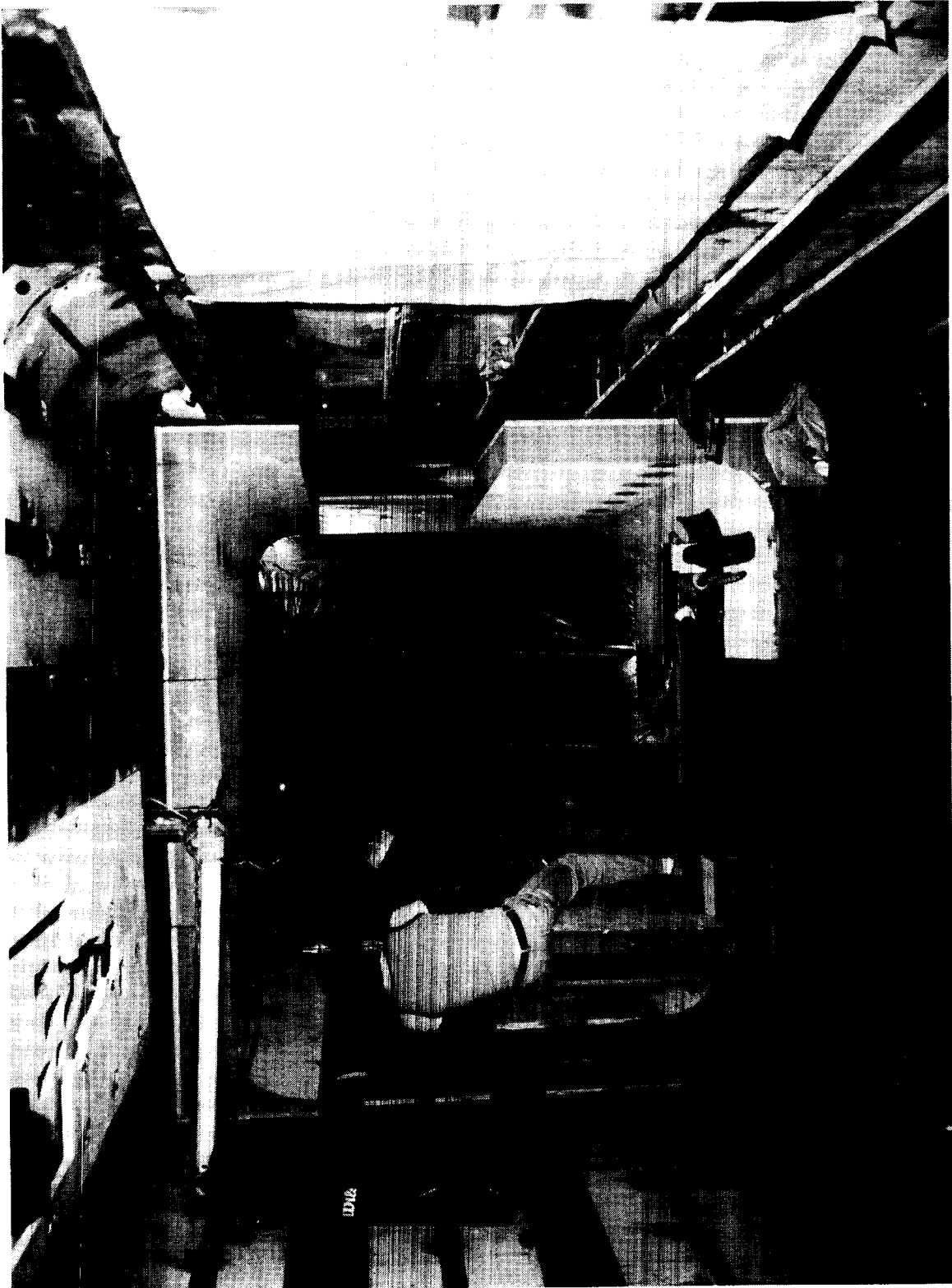


L-81-9809

(c) Substructure for sonic choke.

Figure 42. Continued.

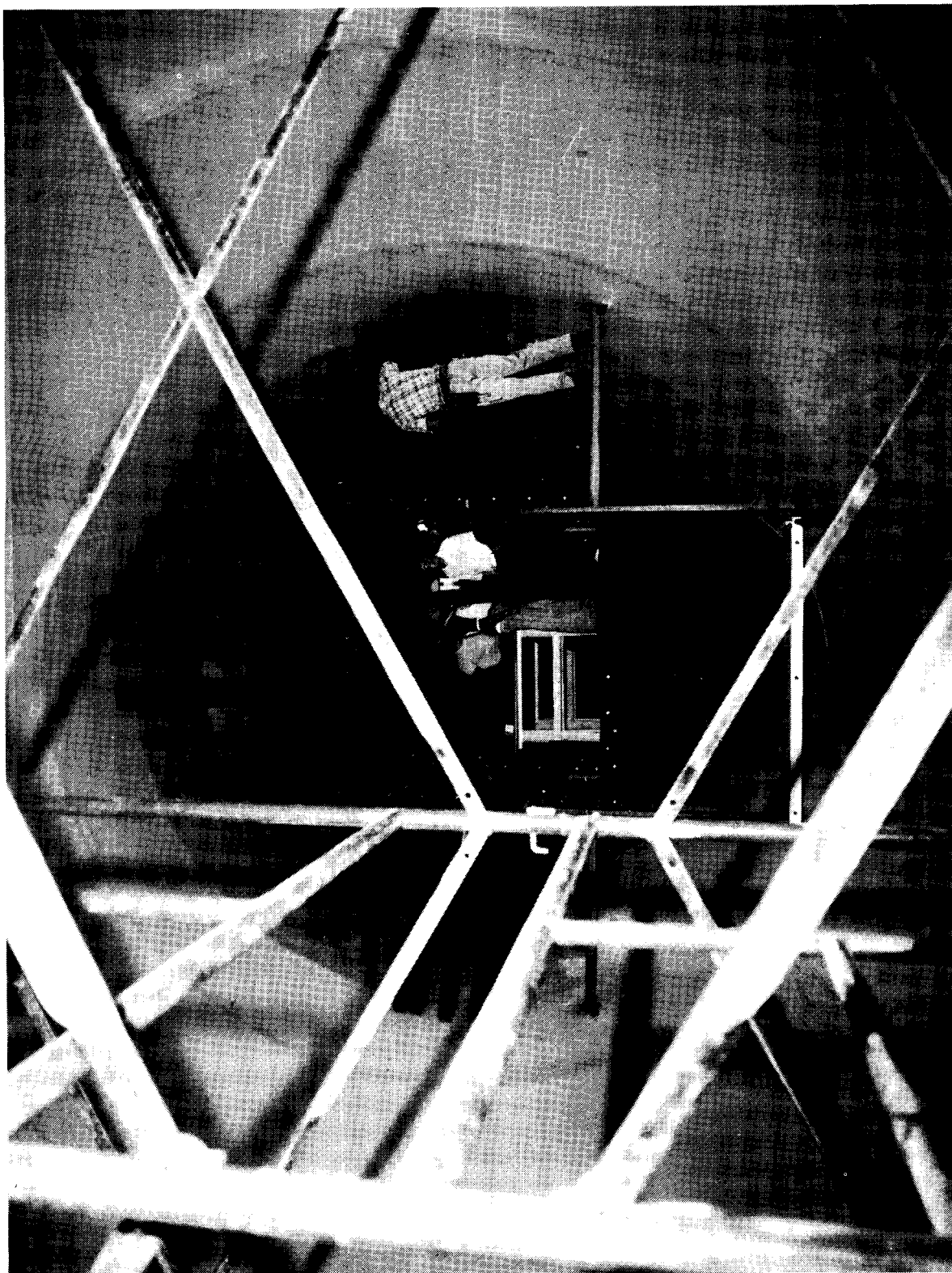
ORIGINAL PAGE IS
OF POOR QUALITY



L-81-11,052

(d) Upstream view of liner-block installation.

Figure 42. Continued.

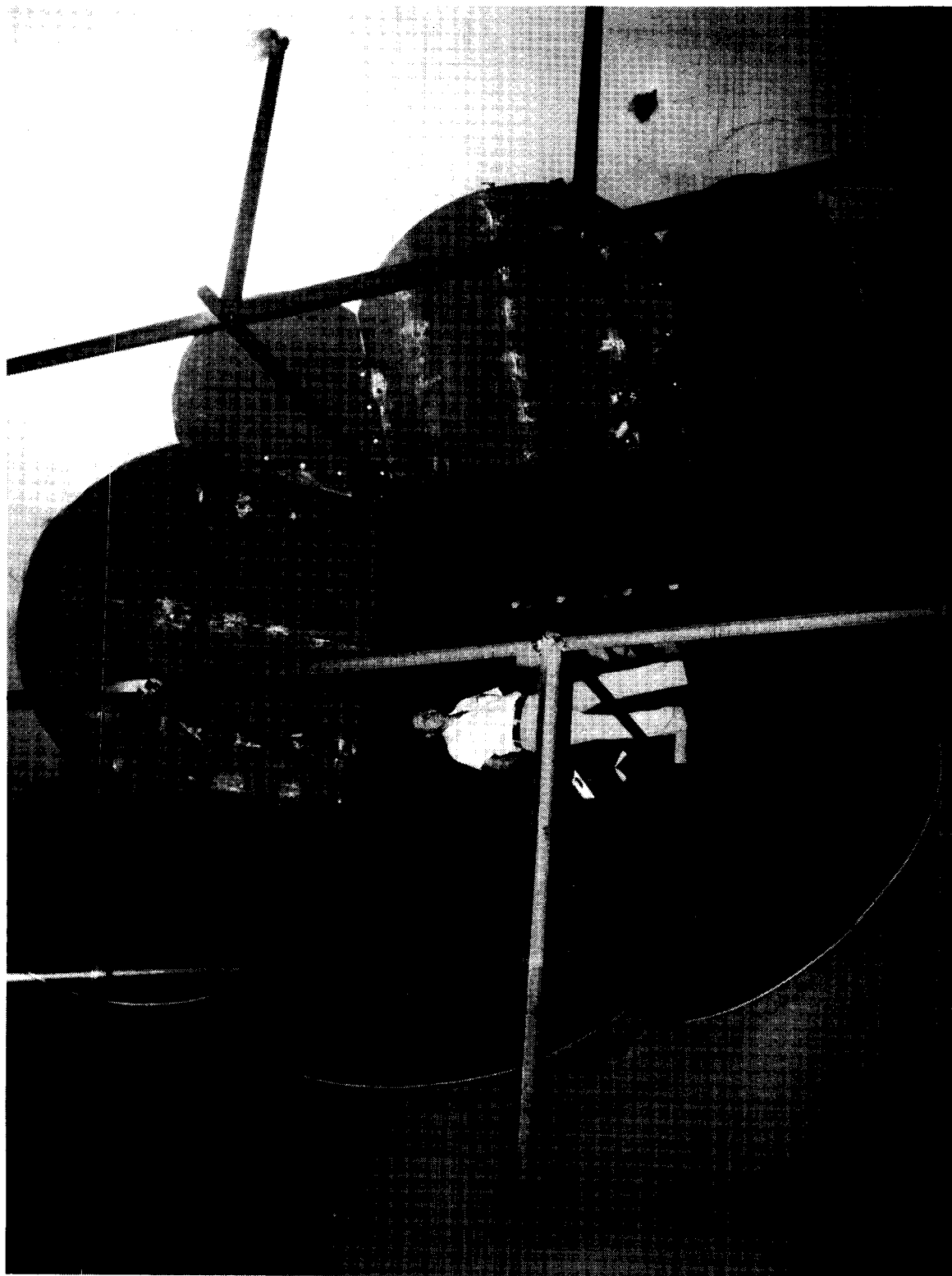


L-81-8074

(e) Downstream view from settling chamber of liner substructure during installation.

Figure 42. Continued.

ORIGINAL PAGE IS
OF POOR QUALITY

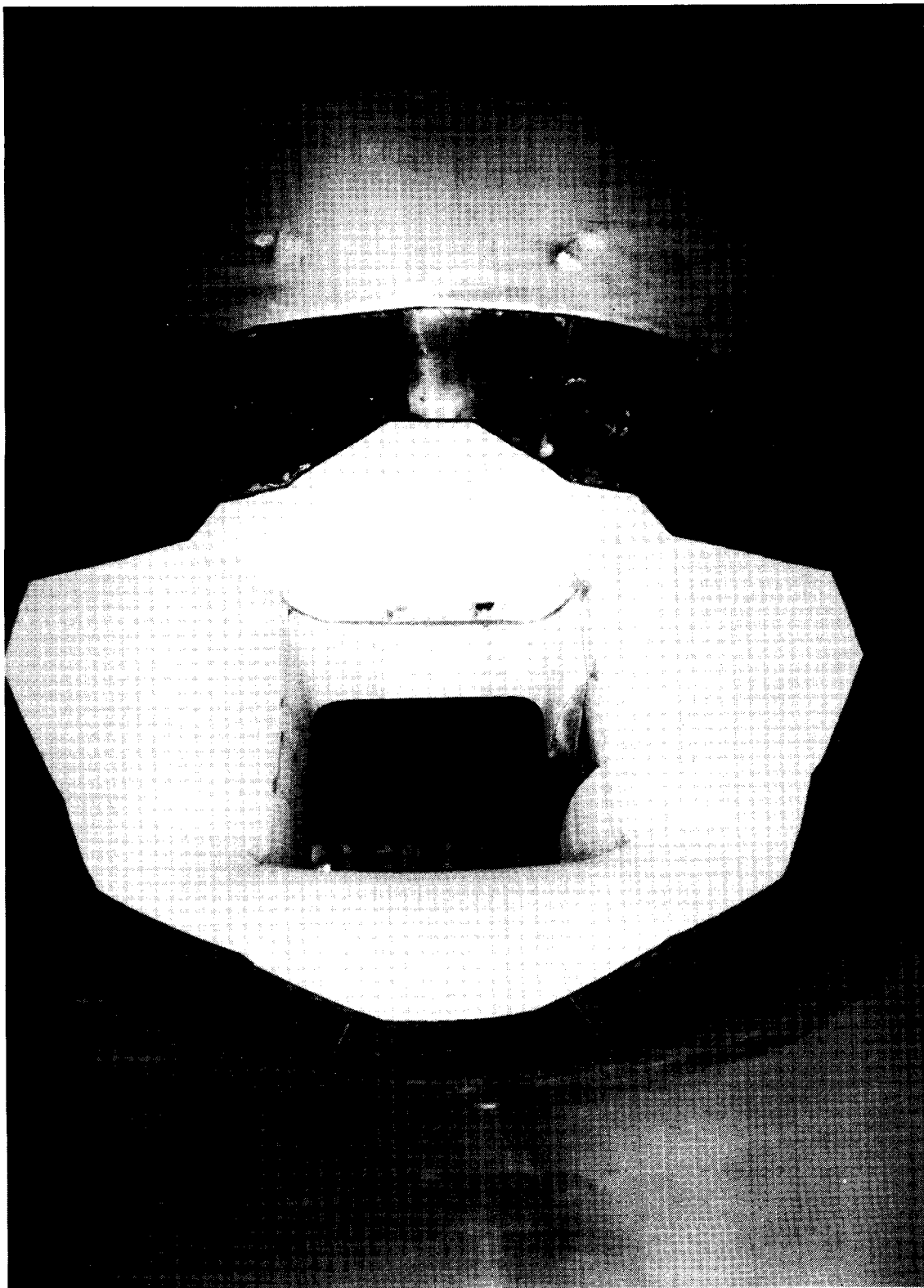


L-81-8496

(f) Downstream view from settling chamber of completed liner substructure.

Figure 42. Continued.

ORIGINAL PAGE IS
OF POOR QUALITY



L-81-11,046

(g) Downstream view from settling chamber of test section entrance region with one floor block removed.

Figure 42. Concluded.

Tunnel	Config.	Λ , deg	c, ft	t/c, percent	Ref.
▽ ARC 12-ft PWT	Body of rev.	0	12	12.5	2
◻ LaRC TDT	Wing	0	7.5	15	
◊ Norair 7 × 10	Body of rev.	0	12	12.5	
○ Zurich 7 × 10	Wing	0	3.97	17	
◻◊ ARC 12-ft PWT	Wing	30, 33	7, 10	12, 15	
△ Norair 7 × 10	Body of rev.	0	12	12.5	46
◻ LaRC LTPT	Wing	0	10	7	
◻◻ LaRC LTPT	Wing	0, 0	7, 18		47
◻◊ Norair 7 × 10	Wing	30, 0	7	12, 5	2

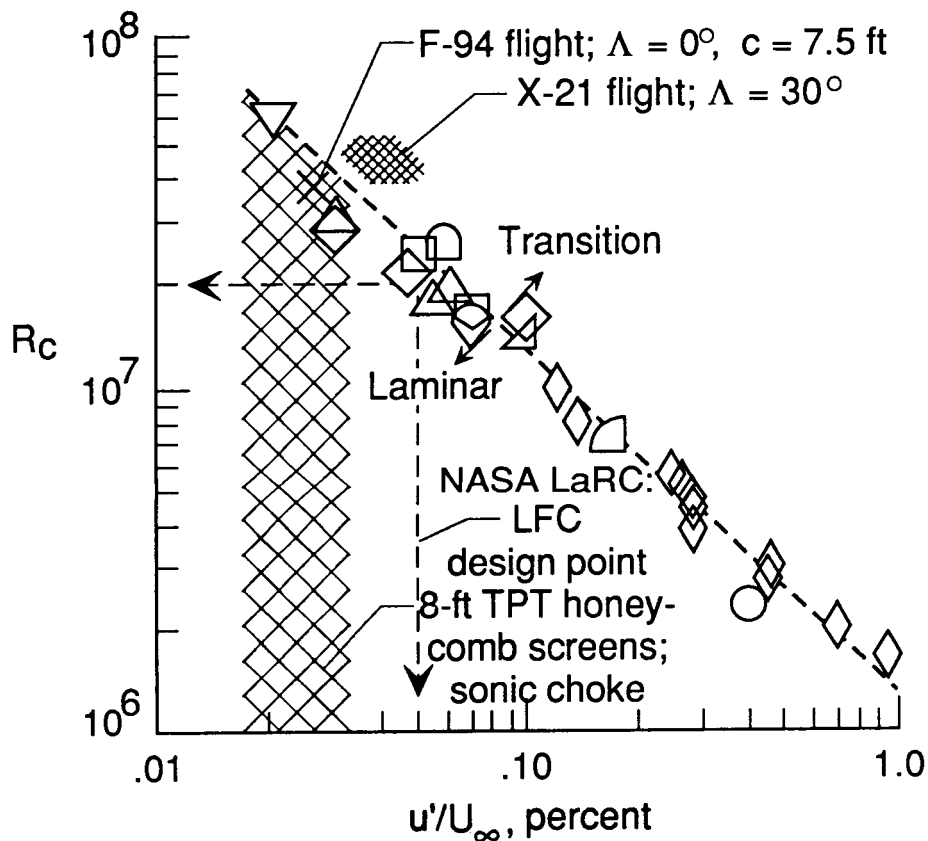


Figure 43. Influence of turbulence level on maximum chord Reynolds number with laminar-flow suction control for low-drag wings and bodies of revolution in wind tunnels and flight. The Mach number of the tunnel data varied from 0 to 0.3, and the Mach number of the flight data varied from 0.4 to 0.8.

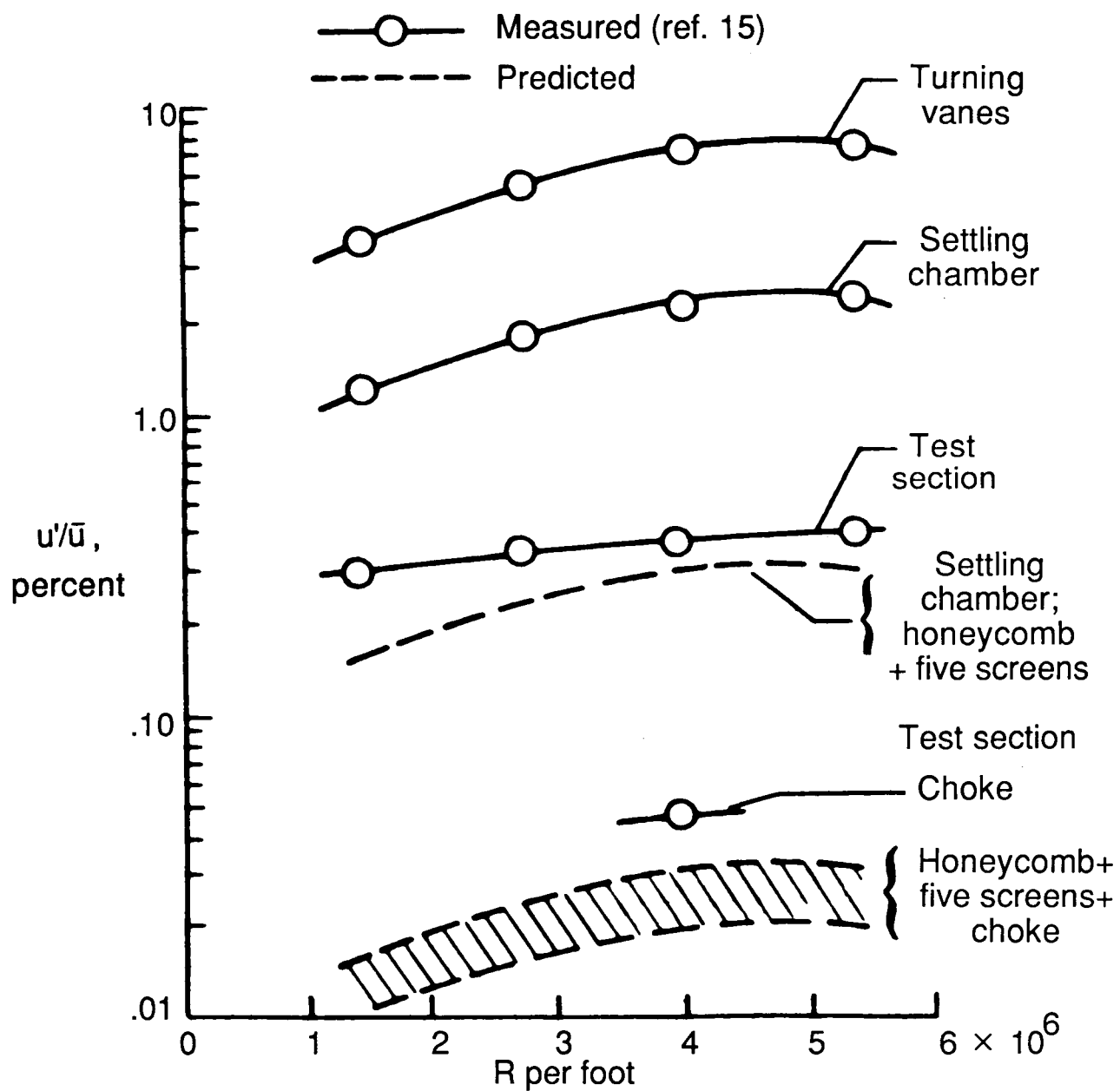
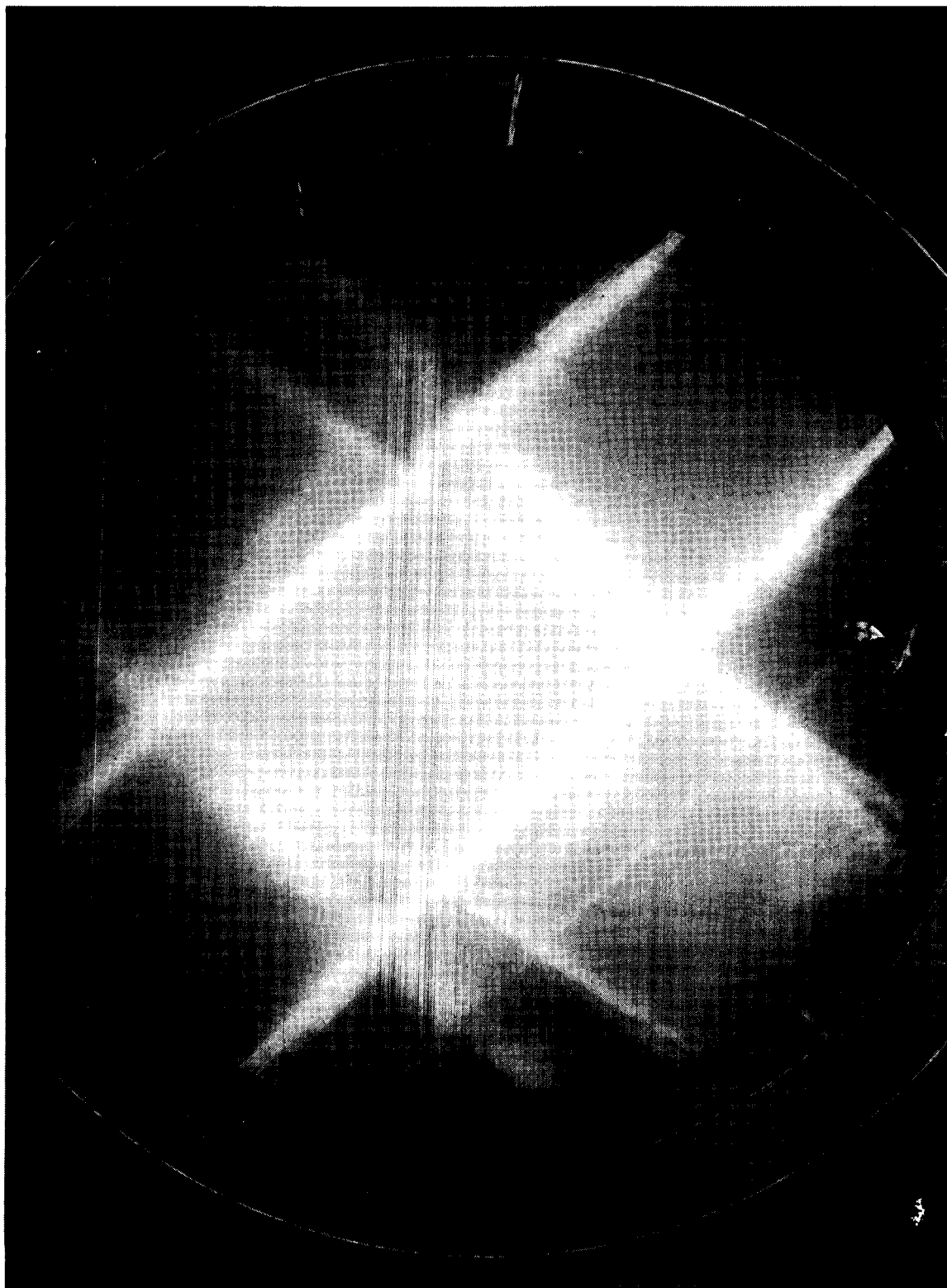


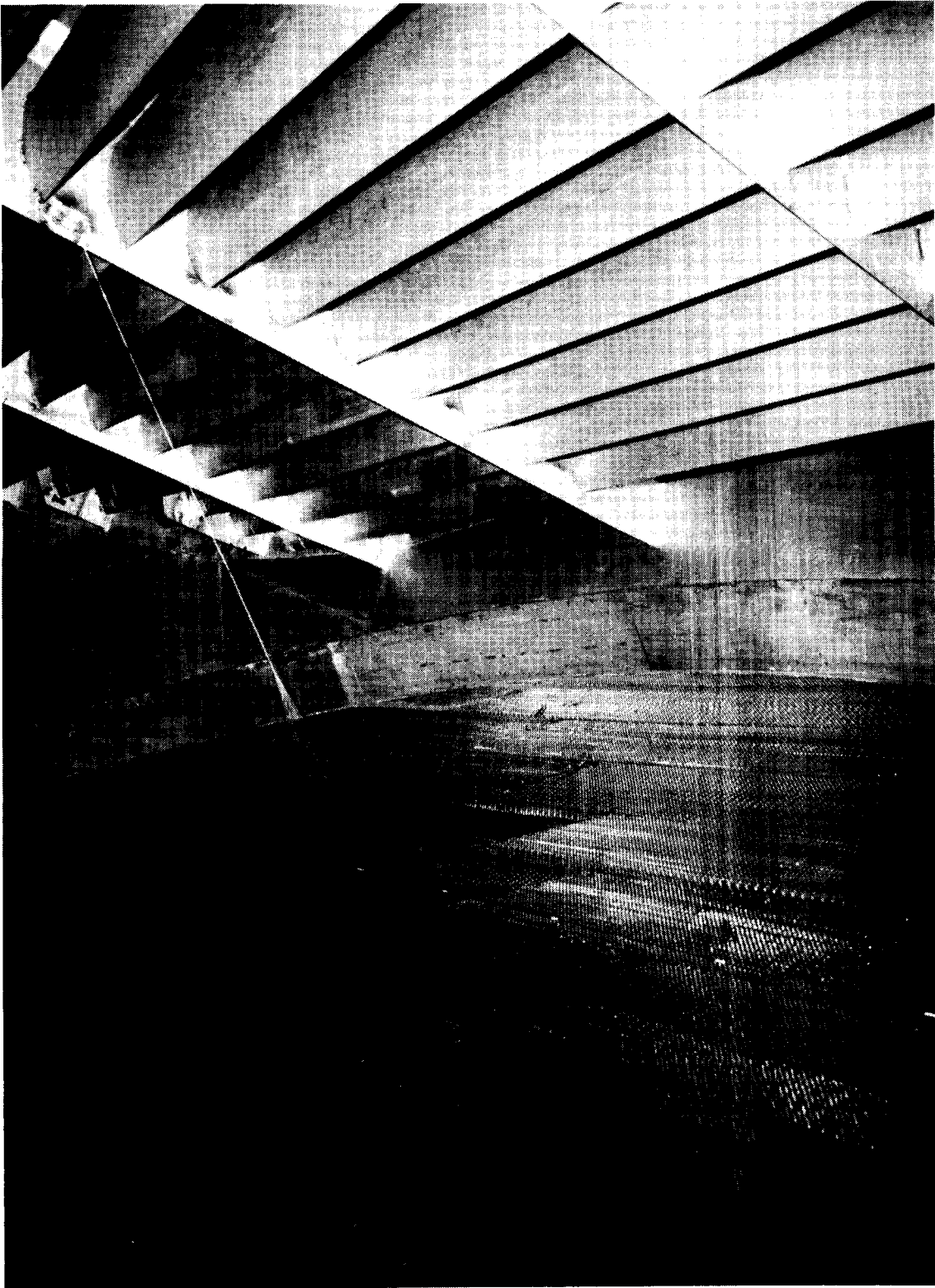
Figure 44. Measured and predicted disturbance levels in the 8-ft TPT with and without choke, honeycomb, and screens at $M_\infty = 0.80$.

ORIGINAL FILE IS
OF POOR QUALITY.



L-84-4065

Figure 45. Upstream view from test section of fifth screen.



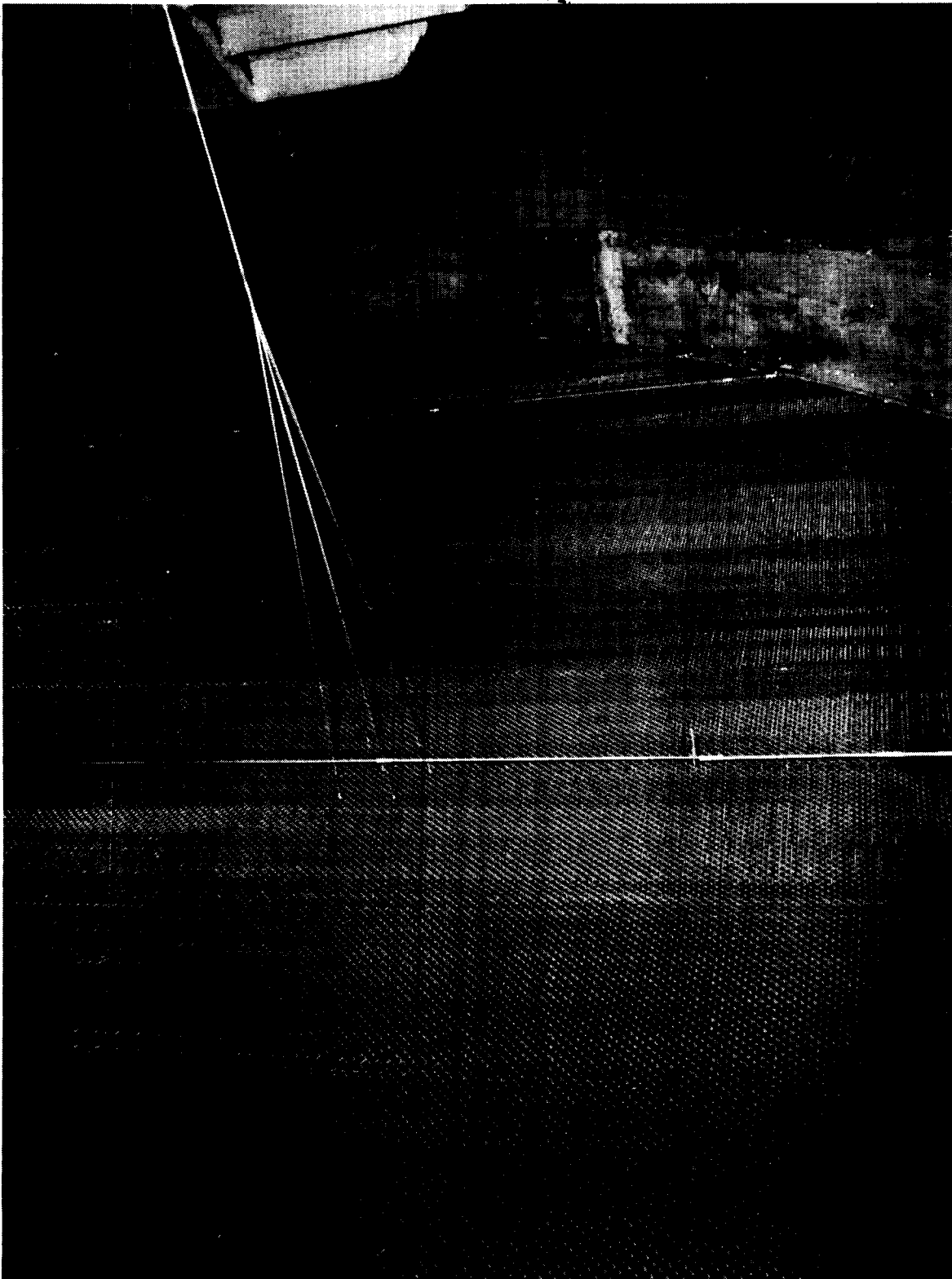
L-82-644

(a) View toward inside upper corner.

Figure 46. Photographs of honeycomb and turning vanes from floor of tunnel between honeycomb and turning vanes.

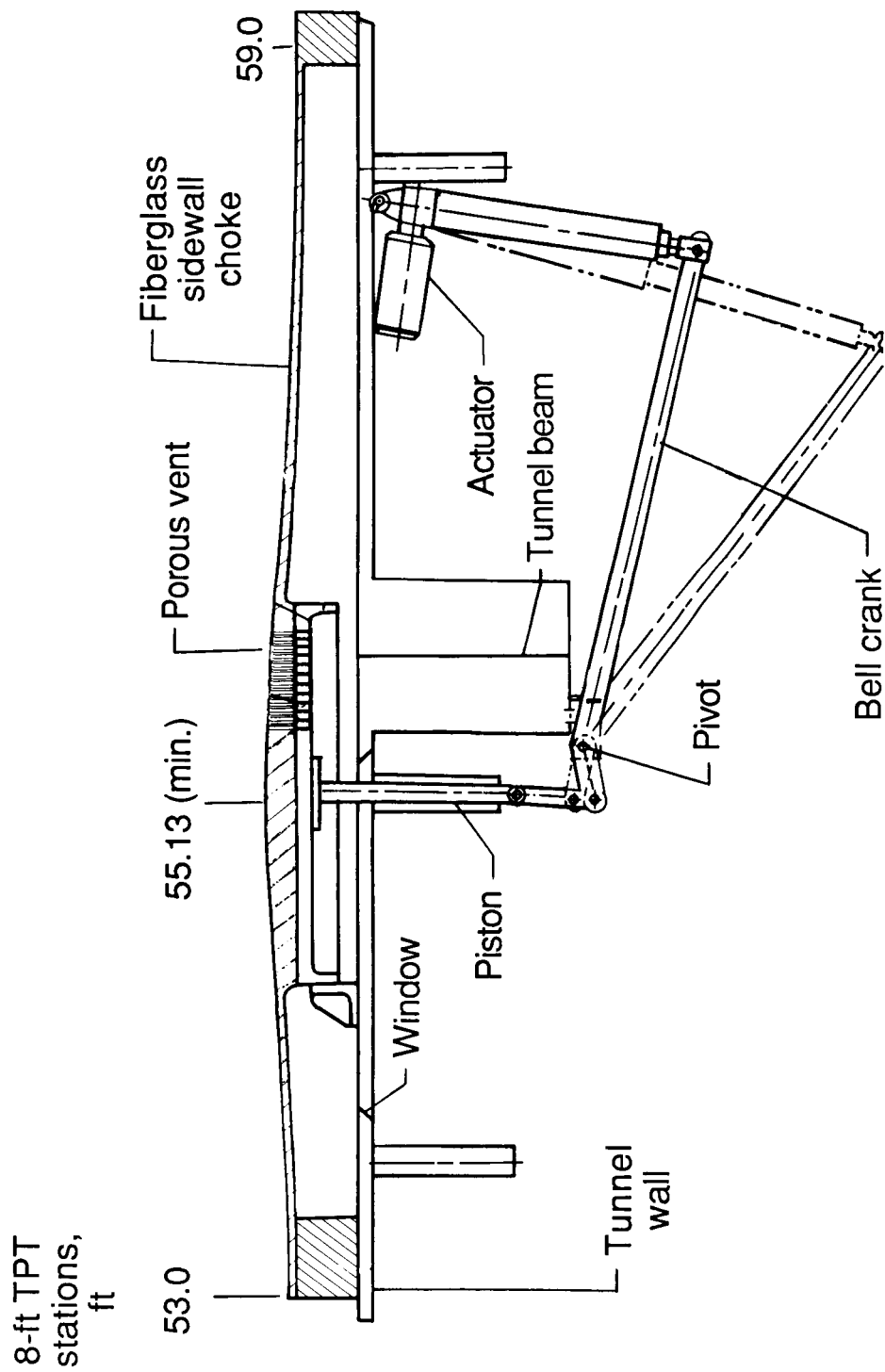
ORIGINAL PAGE IS
OF POOR QUALITY

L-82-647



(b) View toward inside lower corner.

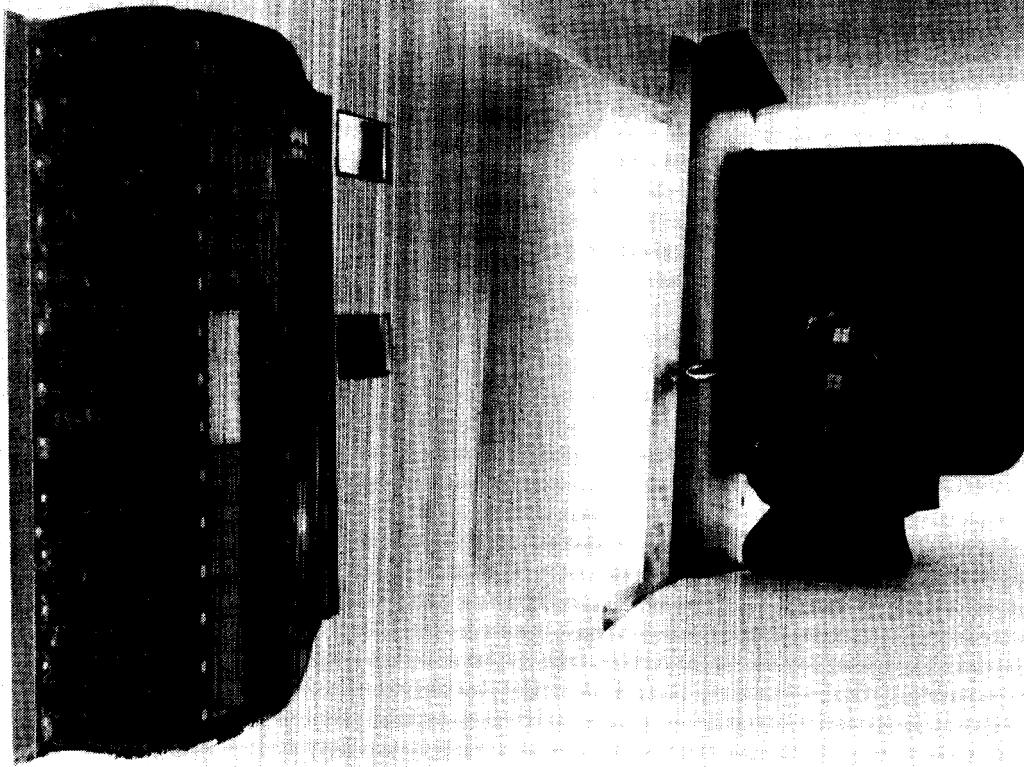
Figure 46. Concluded.



(a) Sketch of liner and choke plate.

Figure 47. Adjustable wall choke plates.

ORIGINAL PAGE IS
OF POOR QUALITY



L-82-3,071

(b) Photograph of choke plate.

Figure 47. Concluded.

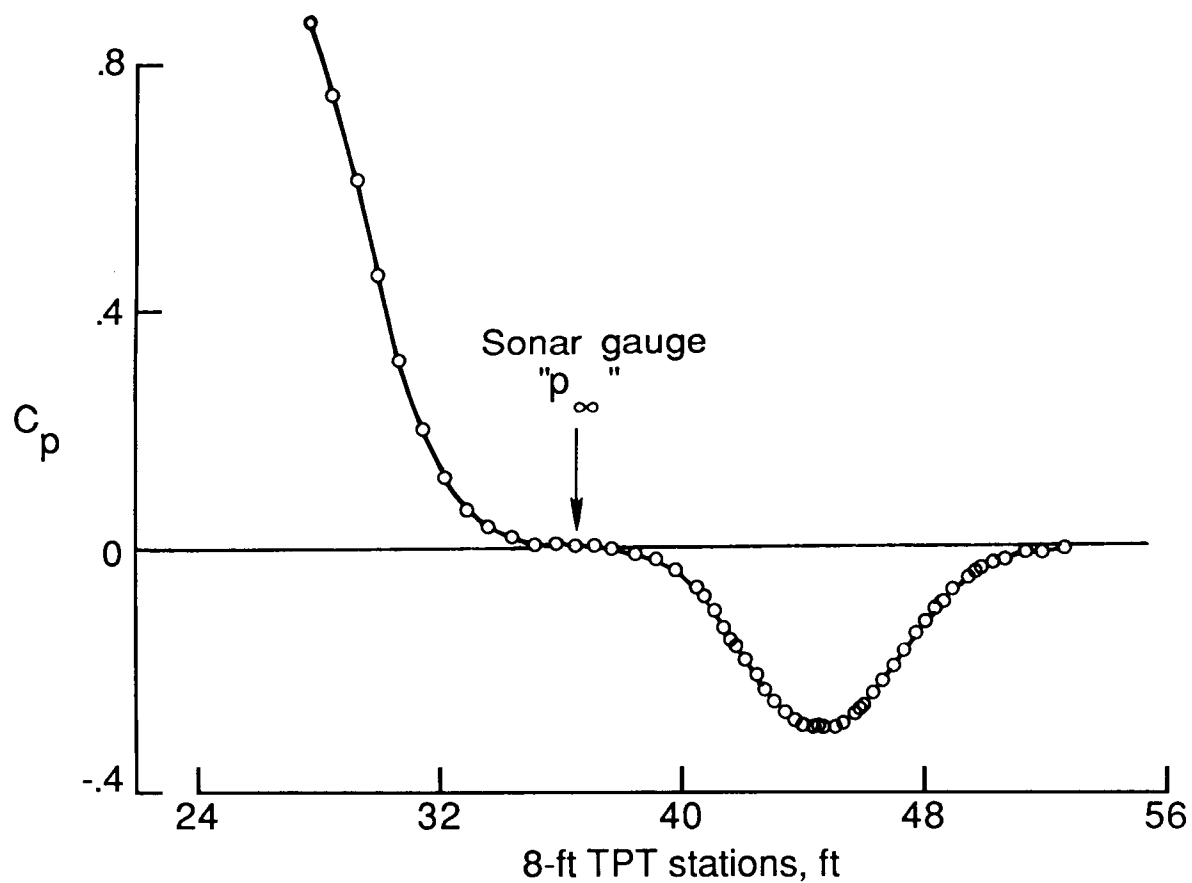
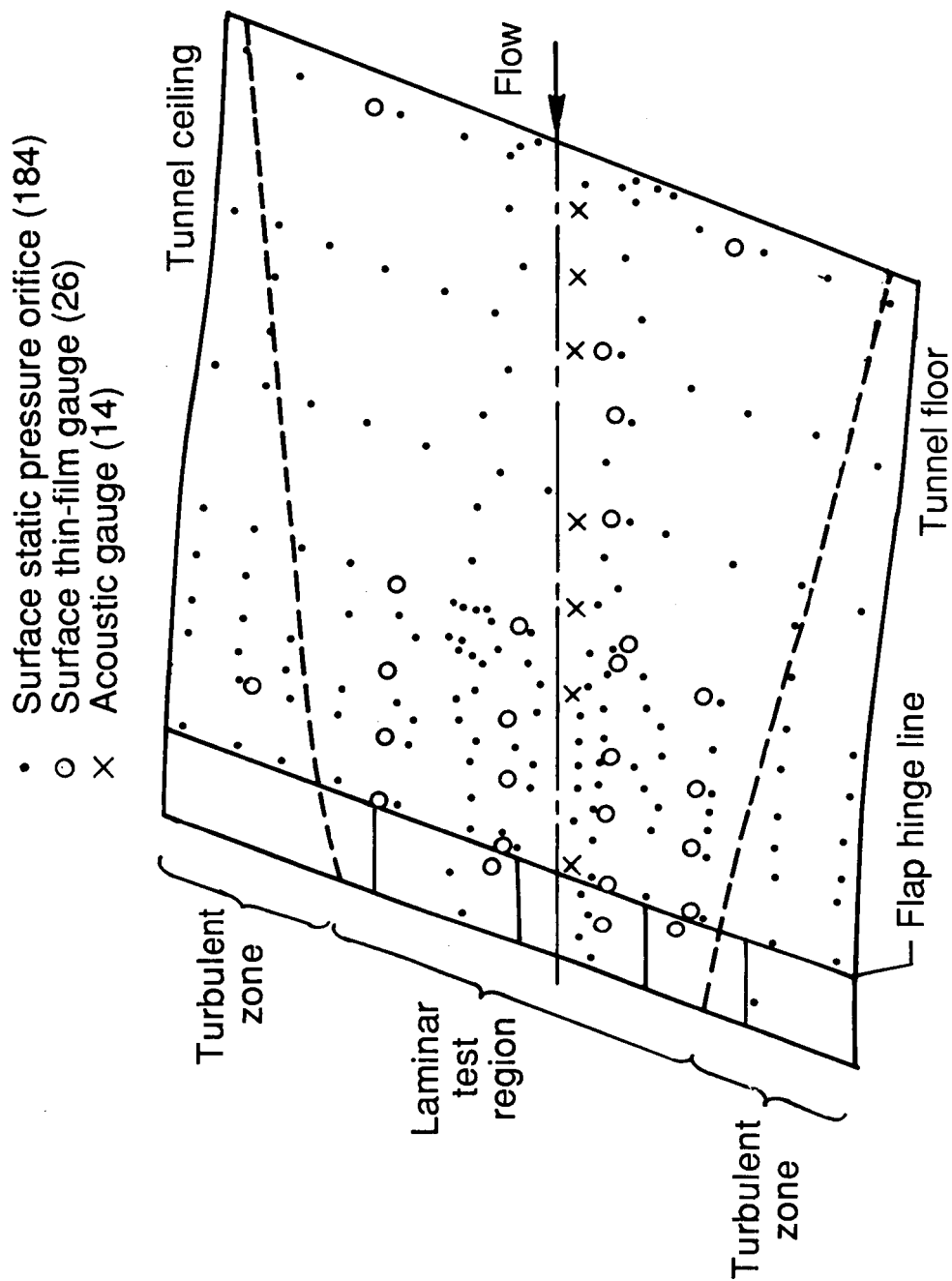
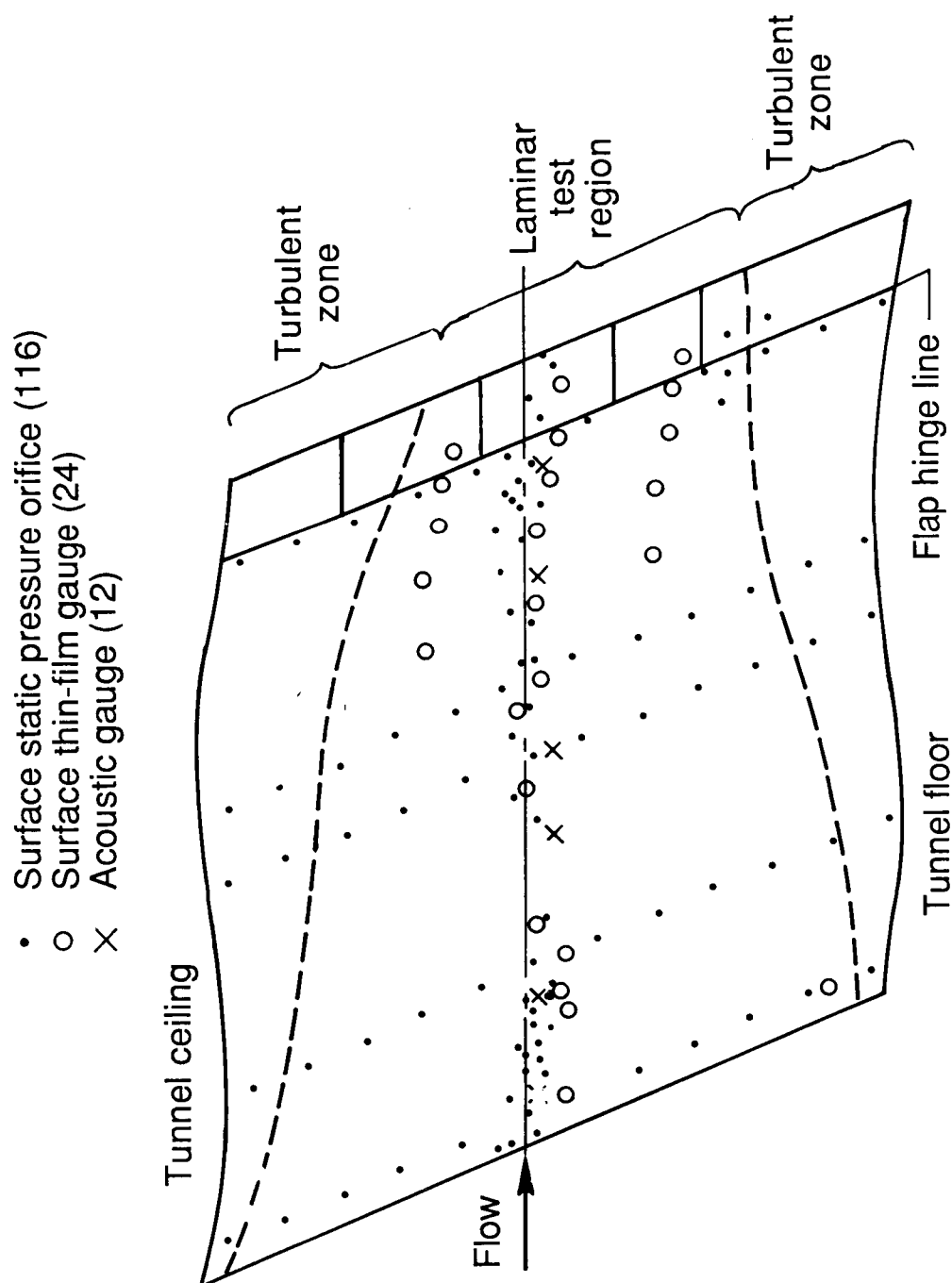


Figure 48. Theoretical distribution of pressure coefficients along middle of liner wall opposite airfoil upper surface at design conditions.



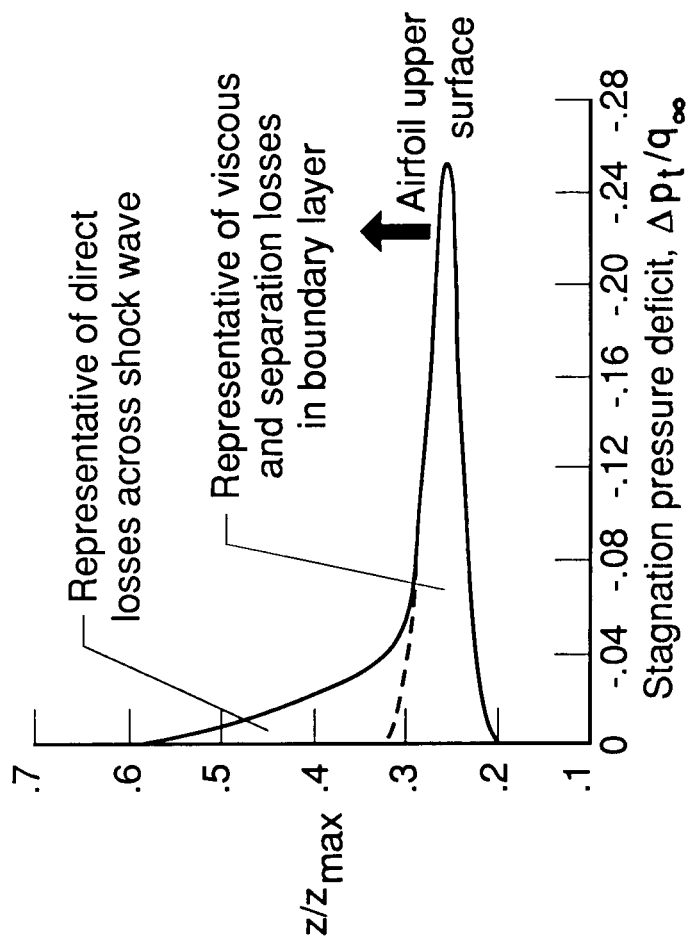
(a) Upper surface.

Figure 49. Model surface instrumentation.

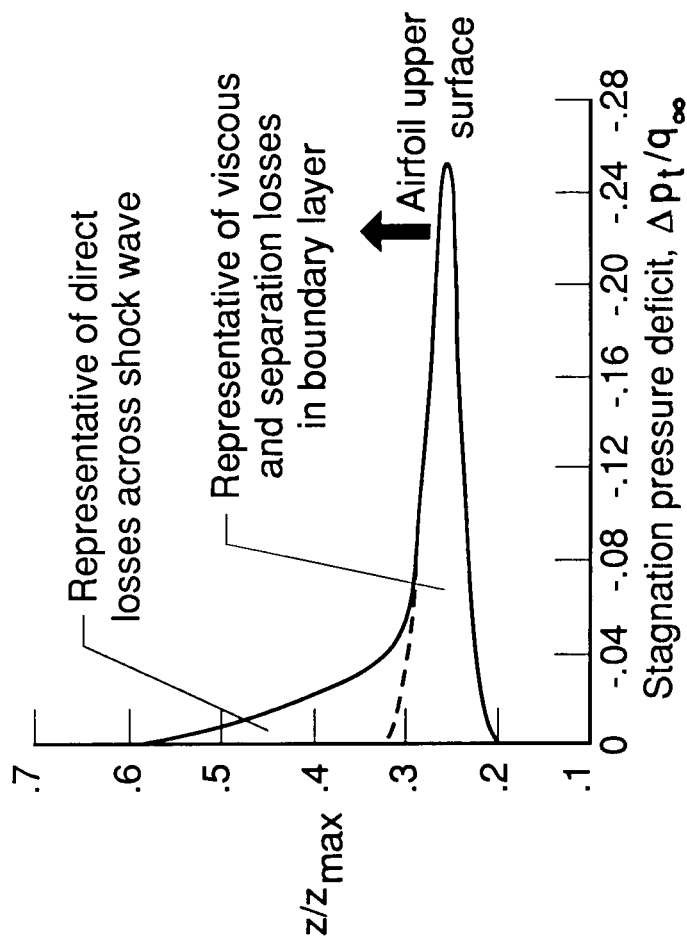


(b) Lower surface.

Figure 49. Concluded.

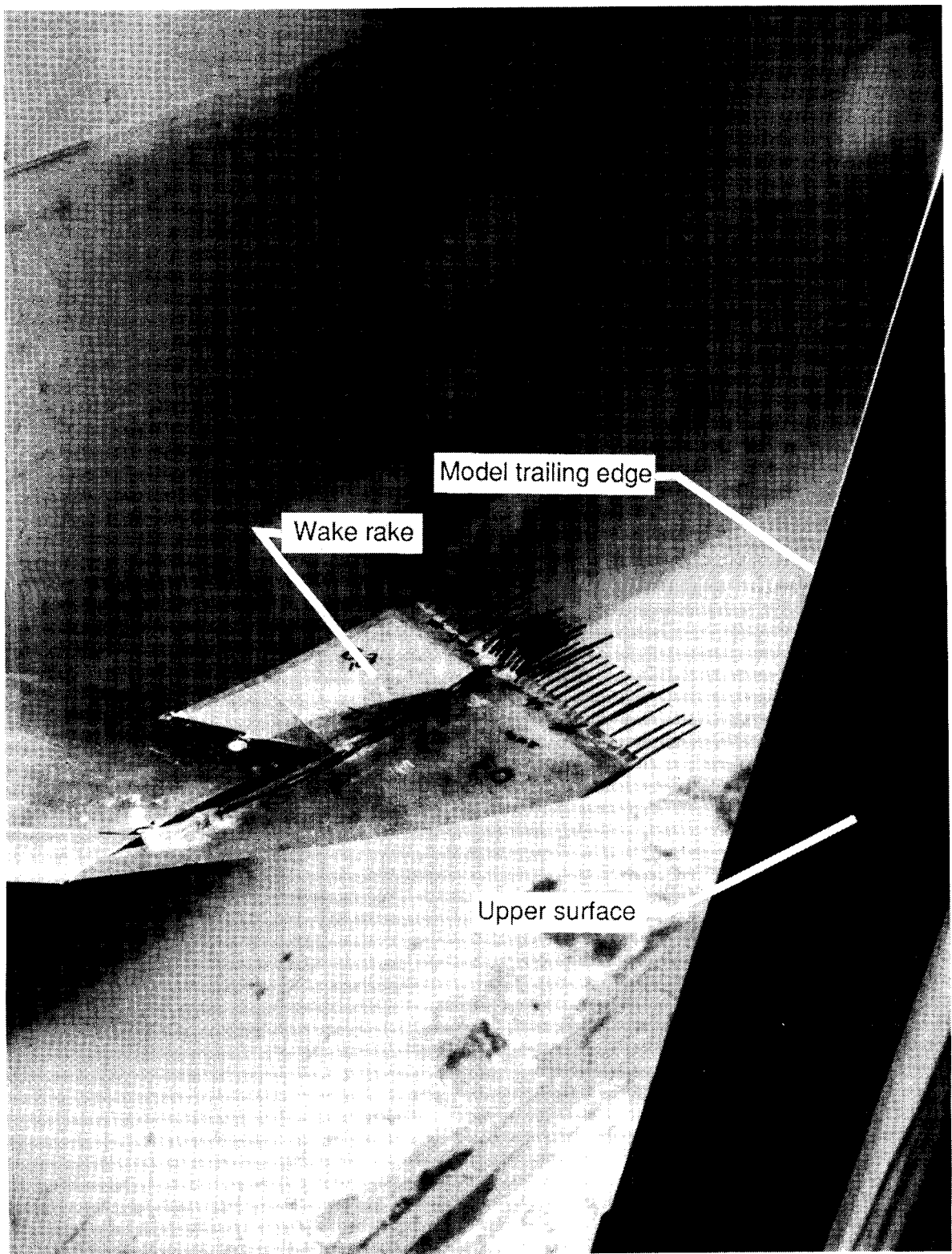


(a) Sketch of profile drag rake.



(b) Schematic of wake profile.

Figure 50. Sketch and photographs of profile drag rake and schematic of wake profile.



L-86-6134

(c) Photograph of profile drag rake behind trailing edge of model.

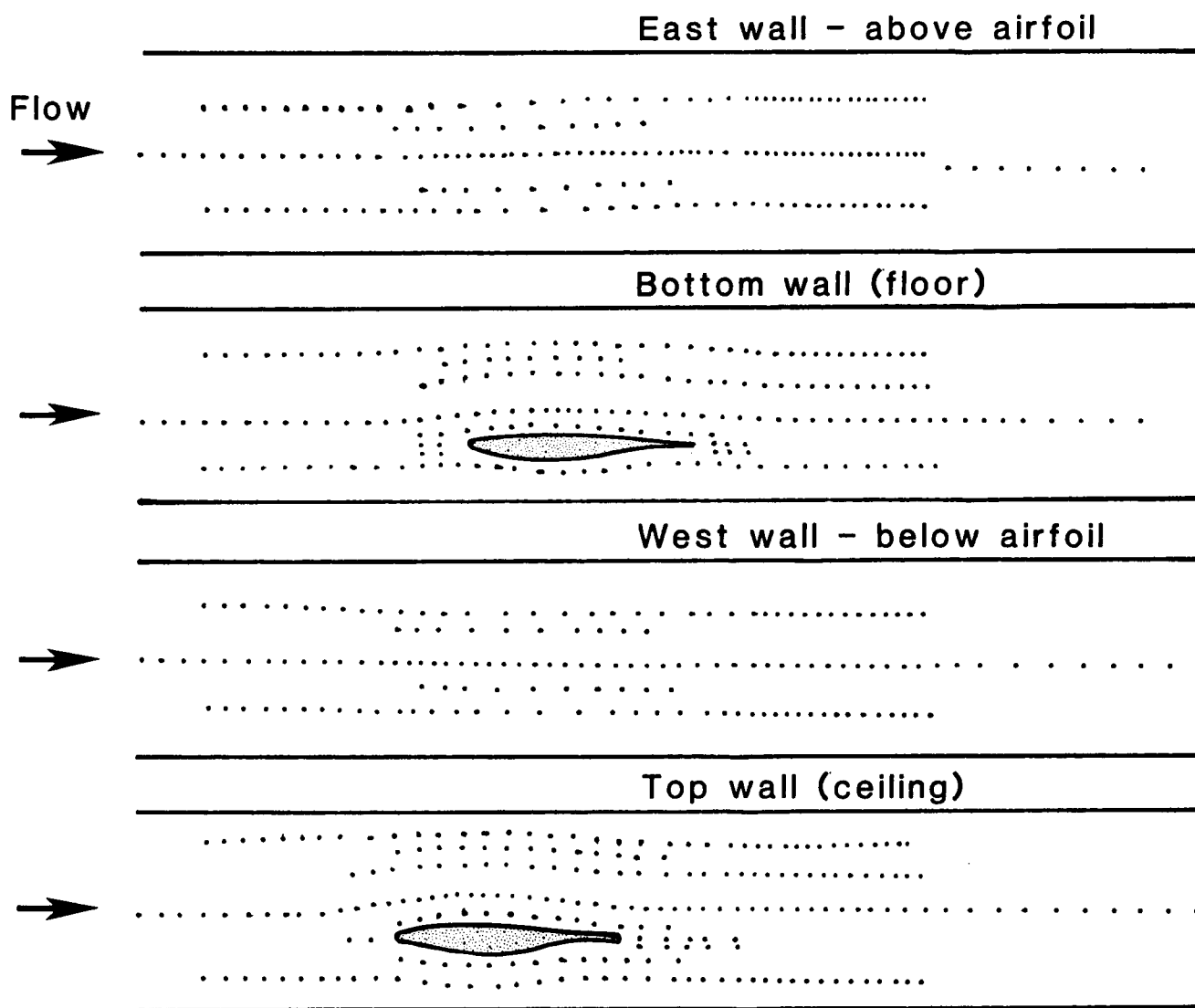
Figure 50. Continued.

L-82-9,339



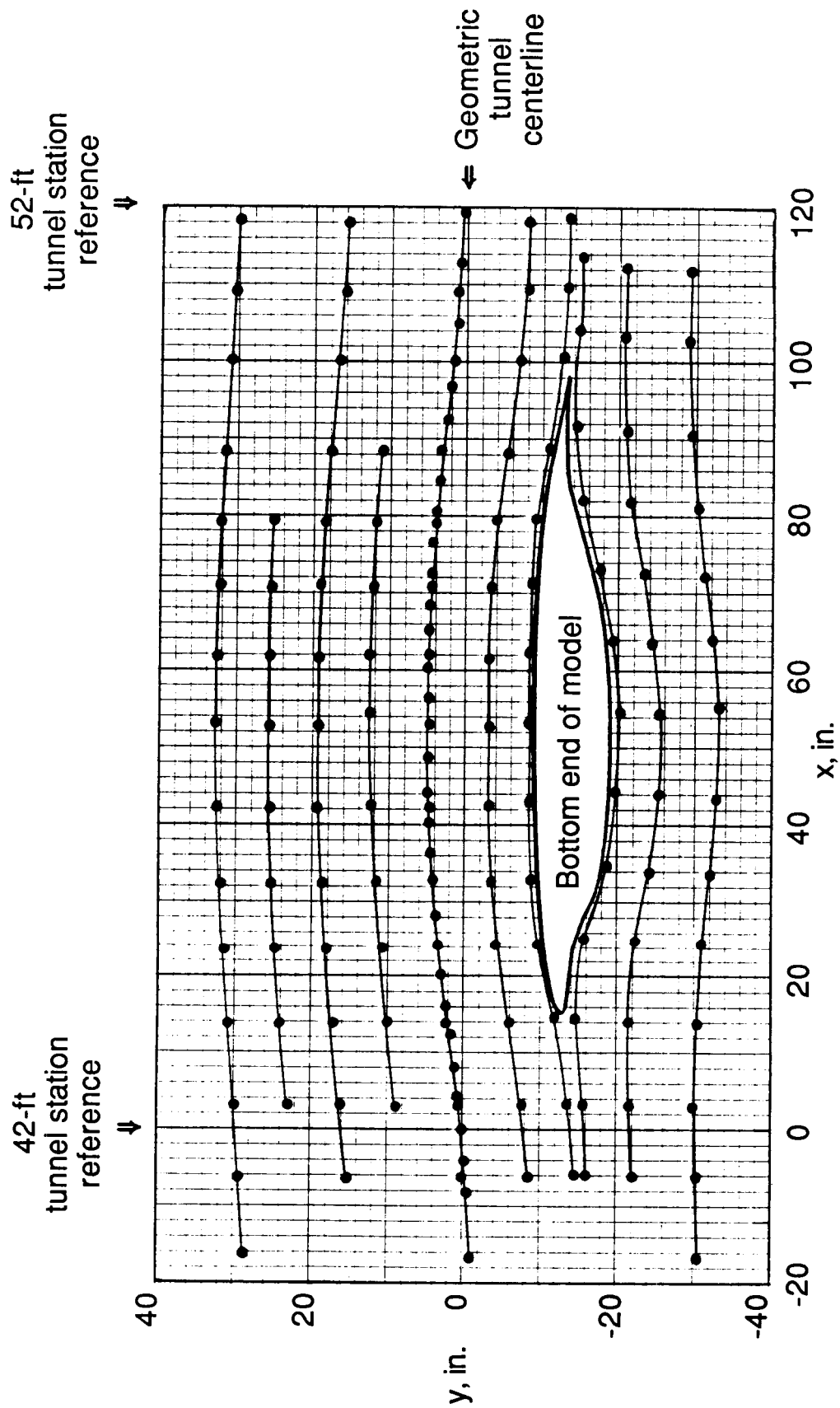
(d) Photograph of wake rake mounted in test section. Upstream view.

Figure 50. Concluded.



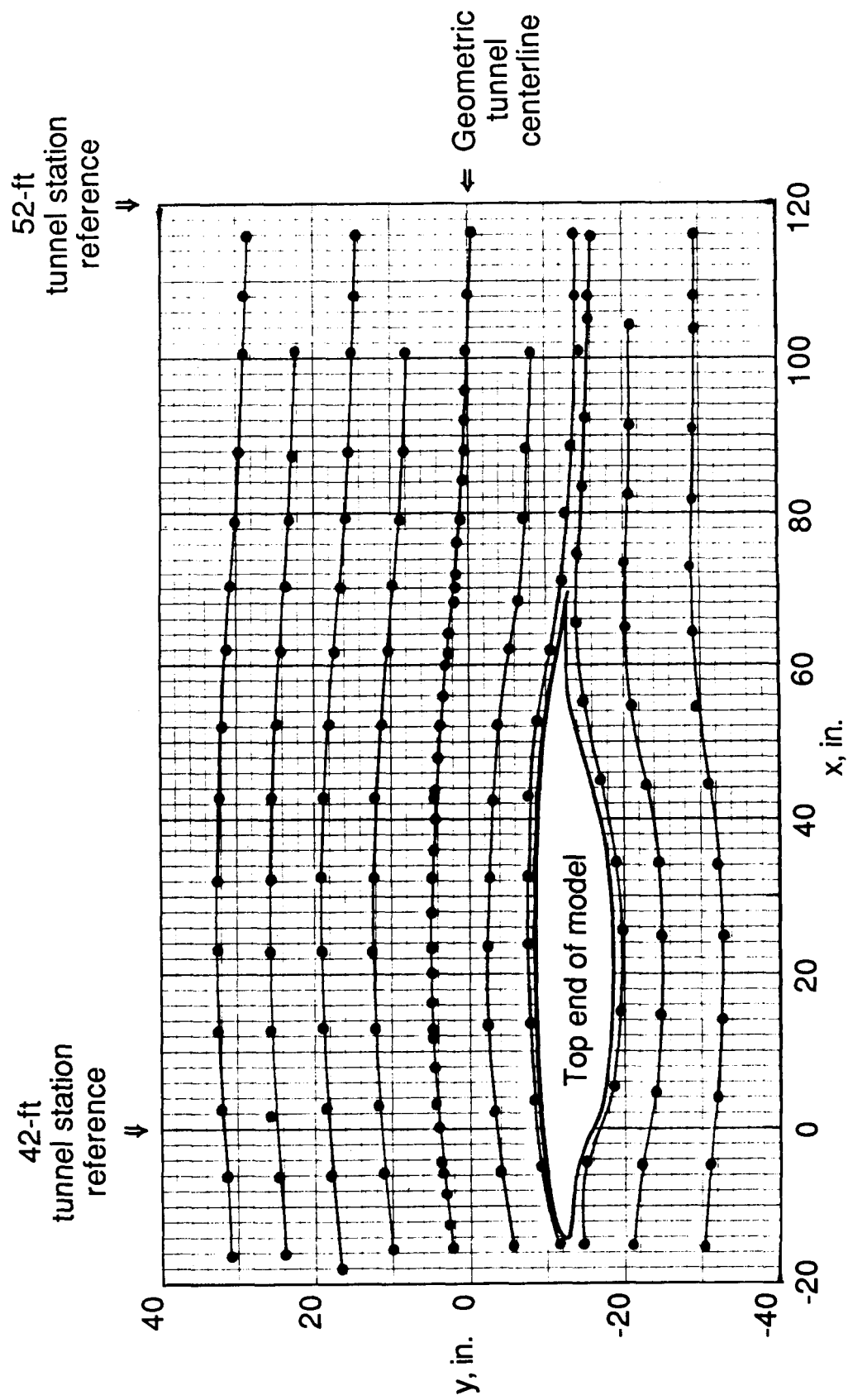
(a) Overall locations.

Figure 51. Pressure orifice locations over four walls of liner.



(b) Orifices around model on floor of test section.

Figure 51. Continued.



(c) Orifices around model on ceiling of test section.

Figure 51. Concluded.

Report Documentation Page

1. Report No. NASA TP-2809		2. Government Accession No.		3. Recipient's Catalog No.	
4. Title and Subtitle The NASA Langley Laminar-Flow-Control Experiment on a Swept, Supercritical Airfoil—Design Overview				5. Report Date May 1988	
				6. Performing Organization Code	
7. Author(s) Charles D. Harris, William D. Harvey, and Cuyler W. Brooks, Jr.				8. Performing Organization Report No. L-16324	
9. Performing Organization Name and Address NASA Langley Research Center Hampton, VA 23665-5225				10. Work Unit No. 505-60-31-03	
				11. Contract or Grant No.	
12. Sponsoring Agency Name and Address National Aeronautics and Space Administration Washington, DC 20546-0001				13. Type of Report and Period Covered Technical Paper	
				14. Sponsoring Agency Code	
15. Supplementary Notes					
16. Abstract A large-chord, swept, supercritical, laminar-flow-control (LFC) airfoil has been designed and constructed and is currently undergoing tests in the Langley 8-Foot Transonic Pressure Tunnel. The experiment was directed toward evaluating the compatibility of LFC and supercritical airfoils, validating prediction techniques, and generating a data base for future transport airfoil design as part of NASA's ongoing research program to reduce drag significantly and increase aircraft efficiency. Unique features of the airfoil included a high design Mach number with shock-free flow and boundary-layer control by suction. Special requirements for the experiment included modifications to the wind tunnel to achieve the necessary flow quality and contouring of the test section walls to simulate free airflow about a swept model at transonic speeds. The design of the airfoil with a slotted suction surface, the suction system, and modifications to the tunnel to meet test requirements are discussed.					
17. Key Words (Suggested by Authors(s)) Laminar-flow control Contoured wind tunnel Transonic aerodynamics Supercritical swept wing				18. Distribution Statement Unclassified—Unlimited Subject Category 02	
19. Security Classif.(of this report) Unclassified		20. Security Classif.(of this page) Unclassified		21. No. of Pages 125	
				22. Price A06	